DYNAMICS OF MOLECULAR ADSORBATES EXPOSED TO ULTRAFAST THERMAL GRADIENTS

BY

JEFFREY ALLEN CARTER

DISSERTATION

Submitted in partial fulfillment of the requirements
for the degree of Doctor of Philosophy in Chemical Physics
in the Graduate College of the
University of Illinois at Urbana-Champaign, 2011

Urbana, Illinois

Doctoral Committee:
Professor Dana Dlott, Chair
Professor Martin Gruebele
Professor David Cahill
Professor James Lisy

Abstract

Energy transfer concerned with how thermal energy is transported at molecular-length scales is a relatively new area and the physics governing this process are not yet well established. The experiments presented here represent initial steps toward developing a better understanding how thermal energy travels across solid-molecule interfaces as well as how thermal energy flows through molecules.

The experimental scheme here is as follows. A molecular monolayer is bound on one end to a gold film, acting as an ultrafast heat bath. Using a laser flash-heating technique, the heat bath can be jumped to several hundred degrees Celsius in a duration of a few picoseconds. As the energy flows from the thermal reservoir into the molecules composing the monolayer, a coherent non-linear vibrational spectroscopy probes specific localized vibrational modes within the monolayer to monitor the presence of thermal disorder on the picosecond time scale.

By measuring the transit time of energy flowing through alkane-based monolayers of increasing length, the flow of thermal energy was found to be ballistic – or constant velocity – in nature as it traveled through the molecules. This data also strongly suggest that energy is deposited directly into a delocalized region of the alkane chains $\sim$0.8-nm in length.

Benzylthiolate-based monolayers allowed the energy transfer dynamics for systems with sub-nanometer lengths. In addition to phonon heating, these monolayers experience electron-heating effects that excited high-energy vibrational mode through inelastic scattering events. For monolayers containing a phenyl group, the electron scattering range was found to be limited to $\leq$1 nm.

For Mom.

Acknowledgements

This thesis would not have been possible without both the initial chance and the scientific direction provided to me by my advisor Dana Dlott, and for that I thank you. To Zhaohui Wang and Alexi Lagutchev: I am grateful for years of lively scientific discussions that have provided much of my experimental background and have solidified my grasp of the related theory. Graduate school would not have been the same without both Rusty Conner and Jonathan Montoya; there are many good memories. To the other graduate students of the Dlott group: I have thoroughly enjoyed my time discussing various scientific ideas, trouble-shooting experimental problems and on those rare occasions just goofing off. And finally to Lindsay Sperling: graduate school and life in general is much better with you.

Contents

List of Figures

List of Tables

1

Introduction

1.1 Overview of Thermal Energy Transport

The scientific study of thermal energy and heat flow dates back to the 1700s and has been the focus of an immense amount of research.[1] By the mid-1800s, the laws of thermodynamics were solidified.[1] This includes the 2^{nd} law of thermodynamics, which states that an isolated system will tend toward equilibration. Thus, two bodies initially at different temperatures will thermalize over time.

Thermodynamics, however, provides no kinetic information about the characteristic time frame for heat flow through a material. Heat conduction experiments – an outgrowth of electrical conduction measurements – were used to study heat flow and thermalization processes beginning in the mid-1700s.[2] These results provided the empirical data for the development of the accepted law of thermal diffusion that describes heat flow through solids.[2]

Heat conduction through solids is described by a random walk of either lattice phonons or electrons.[3] Phonons being the dominate heat transporting medium in

dielectrics, while electrons are the primary carriers for conductors. The heat carrier, having a characteristic mean free path, travels through the material a given statistical length before undergoing a collision that randomizes the propagation direction. This process, repeated many times, results in the diffusive nature of heat transport through solid materials.

As the size of material components gets smaller, whether its the distribution of grain sizes for a polycrystalline material or the individual components of a composite material, the ratio of material at an interface relative that of bulk material increases. A consequence, there is a length scale where the rate of energy flow, given a thermal gradient, is no longer determined by the diffusive nature of the heat carriers. Instead, the energy transfer across interfacial boundaries becomes the rate limiting in the thermalization process.[4] This occurs, because at each interface, the phonons are either reflected or transmitted. The relative amount of transmitted energy depends on the incident collision angle, the acoustic impedance and the alignment of the phonon density of states.[4] Designer materials with unique thermal conduction properties can be made by taking advantage of these effects.[5,6]

Pushing further to even smaller length scales, at distances of $\sim$1 nm, one can begin to discuss how thermal energy travels through materials that are $\sim$1 molecule thick. At the molecular level, the continuum mechanics model that describes energy transport in solid breaks down and a more detailed description of energy transport is necessary. Thermal conductance at the molecular level is predicted to be quite different than the analogous process in bulk systems.[7,8]

Theoretical work trying to determine the most important factors in thermal conductance of molecular systems produced several interesting results – some

surprising, while others more or less expected.[7] Segal *et al.* treated a model system of a saturated alkane attached at either end to two different heat baths. The heat baths were modeled with a continuum of phonon states up to a cutoff frequency, corresponding to a realistic Debye temperature, and the fictitious molecule was modeled with a discrete set of vibrational levels. These studies found that the rate of energy transfer depended on the density and localization of molecular vibrational states, the anharmonic coupling strength between the phonon modes and the molecular vibrations, and also the Debye temperature of the heat baths.[7]

From a basic energy-transfer perspective, these results are reasonable intuitive. The higher the density of states, the more modes are available to exchange energy. Likewise, the stronger the coupling between the normal modes of the molecule and the phonon modes of the heat bath, the more efficient energy transfer occurs and the flow of thermal energy is faster.

Another result from these simulations was that a model system composed of coupled harmonic oscillators was sufficient to explain heat conduction through these molecules, a process dominated by ballistic energy transfer.[7] More completed models using Morse potentials to describe the molecular normal modes only deviated slightly at physically relevant conditions. This suggests a stark contrast in the manner of how heat is transported through molecules compared to larger, macroscopic system. These simulations provide an interesting set of questions about the nature of molecular thermal conductance.

At this point, one may wonder why the thermal transport properties of molecular-based systems are of interest. There is a strong fundamental interest in studying energy transfer, in general, at the molecular level. The quantum nature of molecular motion makes a molecule's behavior interesting. The heat transport through

molecules also represents a new class of experiments that probe the interworking of molecules. Traditional experiments designed to study molecular energy transfer do so by exciting a specific quantum state and monitor the energy decay into lower-energy vibrational states. Energy transfer with incoherent thermal excitations is qualitatively different; thermal fluctuations excite localized structural vibrations and the thermal energy subsequently travels through the molecule, driven by the presence of a thermal gradient. Few experiments have been designed to study the flow of thermal energy across molecular-scale systems.[8–11]

These types of studies are not simply academic problems. Successful integration of molecular components into electronic devices will have to address dissipation of thermal energy.[7,8] As an electronic current tunnels through a molecular wire, inelastic collisions will stochastically deposit large amounts of vibrational energy into the molecule.[12,13] The rate at which this heat can be removed from the device will dictate the steady-state temperature of the system. If the dissipation of energy from the molecular wire into the electrical contact is too slow, then the device will overheat and become thermodynamically unstable, ultimately leading to failure.

One should note that nanoscale heat transport is not exactly the same as bulk heat transport. At nanometer length scales, the transfer of thermal energy occurs on the picosecond time scale and on such short time scales not all molecular vibrational modes will be in thermal equilibrium. Over time the transfered energy will eventually be distributed across all accessible degrees of freedom. For example, at an initial time the heat bath and the molecular system are in thermal equilibrium. If at some later point, the temperature of the heat bath is increase rapidly, leaving the molecular system at the original temperature. The presence

of a thermal gradient leads to energy transfer from the heat bath to the molecular system and at some later time the system will again be in thermal equilibrium. Regardless of the how the energy is carried or the type of dynamics that occur, this process is inherently a heat transport event.

1.2 Previous Work Toward Molecular-Scale Thermal Conduction

Schwarzer *et al.*[9,10] measured energy flow across aliphatic chains bound between azulene and anthracene functional groups in molecules within supercritical xenon. The S_1 electronic state of azulene undergoes fast internal conversion following excitation, leaving a substantial amount of vibrational energy localized to the azulene group. Energy migrates from the azulene group through the aliphatic linker chain and into the anthracene group over several picoseconds. The transfer of this energy was monitored with a time-delayed probe laser tuned to either the red edge of the azulene $S_0 \rightarrow S_3$ transition – watching for a decrease in hot-band excitation as the energy leaves the azulene – or the red edge of the anthracene $S_0 \rightarrow S_1$ transition – waiting for the arrival of vibrational energy to normal modes localized on the anthracene function group, increasing the hot-band absorption.

These energy transfer studies observed two types of energy transfer across these molecules characterized by different time scales.[9,10] On the ∼100-fs time scale, 15%-20% of the initial vibrational energy departs from the azulene group and is explained by the vibrational dephasing of normal modes that span the entire molecular system. On the ∼1-ps time scale, the energy transfer occurs

through anharmonic coupling between normal modes. The characteristic time scale τ for thermalization between the azulene and anthracene heat baths levels off with the aliphatic chain length after $\sim$3 CH_2 units. Thus the rate of thermalization is determined by the coupling of the heat baths to the chain. The energy transfer across the chain is thought to occur scatter-free, corresponding to ballistic transport.

These experiments represent the earliest studies of how excess vibrational energy, localized to a particular spatial region, thermalizes with the remaining regions of the molecule. Perhaps referring to the azulene group as a heat bath is not entirely accurate; the vibrational populations at early times will cannot be represented well with a single local temperature. Regardless, these studies provide an interesting insight into spatially resolved energy transport, which is a key feature of any molecular conductance experiment.

Smits *et al.*[15] conduced experiments that monitored the flow of energy from membrane-bound water through model biological lipid membrane. In these experiments, an ultrafast infrared pulse pumped the OH stretching vibrations of the interfacial water, and through anharmonic couplings the vibrational energy was transfered to the hydrophilic lipid head group. The vibrational energy subsequently traveled through the saturated lipid tails. And once the energy traversed the length of the monolayer, thermally-induced disorder within the model membrane began to appear. The time dynamics of the membrane disorder was measured by vibrationally-resonant sum-frequency spectroscopy – a second-order nonlinear vibrational spectroscopy. For this system, a time delay was observed between the vibrational excitation of the interfacial water and the onset of thermal disorder of $\sim$0.95 ps.[15]

The interpretation of this number is not straight forward. The energy must flow from the initially excited interfacial water molecules into lipid modes that are anharmonically coupled to the water. Hydrogen bonding between the water molecules and the hydrophilic lipid head groups leads to moderately efficient energy transfer into other localized high-frequency modes.[16] Although it may also be possible that the dominate energy transfer pathway requires the excited OH stretch to decay into bulk water librations, which then couple to lower-energy structural modes. Once the energy is deposited into the lipid membrane, then it must migrate through the length of the molecule. Exactly what the measure delay time means depends on the exact nature and timescales of these intermolecular and intramolecular energy transfer steps.

Similar to the work of Schwarzer *et al.*,[9,10] the laser-excited interfacial water is not a well-defined by one temperature at early delay times and does not constitute what most would describe as a traditional heat bath. Nonetheless, this work is an important step in spatially resolved energy transport within molecular materials.

Wang *et al.*[17] conducted room-temperature thermal conductance measurements of alkanedithiol self-assemled monolayers (SAM) sandwiched between Au and GaAs layers, forming a Au-SAM-GaAs junction. Using the 3ω method,[18] the interfacial conductance of the entire junction, including both interfaces, was measured for several alkanedithiols with different lengths. The interfacial conductivity of these systems was measured to be $\sim$25 MW m^{-2} K^{-1} and nearly independent of chain length.

Interfacial conductance measurements on multi-layered materials, such as Au-SAM-GaAs junctions, are less than ideal to obtain detailed information about single interface properties. Accordingly, no new information about how thermal

energy is transported across individual solid-molecule interfaces can be extracted from these studies. Also, effects of surface roughness for these measurements are unknown. The root-mean-square surface roughness of freshly oxide-etched GaAs and flame-annealed Au are reported to be 0.6($\pm$0.1) and 1.5($\pm$0.3) nm, respectively;[17] the alkanedithiol molecules used for this study are a mere $\sim$1.4-nm thick. Even through the root-mean-square surface roughness is only one descriptor in surface metrology, the surface topography is probably such that poor thermal contact is made between the Au-SAM interface. As a result, the measured interfacial conductance values are likely lower than those of an ideal junction.

Ge *et al.*[18] took a different approach to measure the interfacial conductance of molecule-solid junctions. These experiments used monolayer-capped Au nanoparticles suspended in an aqueous solutions. In this scheme the nanoparticles, acting as a heat bath, were laser flash-heated, while the aqueous solution served as a heat sink and energy flowed out of the nanoparticles, through the molecules and then finally into the solution. The fluidic nature of the heat sink ensured that poor physical contact at the interfaces was minimized – an improvement over the studies of Wang *et al.*[17]

These experiments still measure an effective interfacial conductance over two separate interfaces. However, through cleaver modification of the monolayer, this problem was somewhat mitigated. Both hydrophobic and hydrophilic SAM-H_2O interfaces were studied, having thermal conductivities of 50($\pm$5) and 100($\pm$20) MW m^{-2} K^{-1}, respectively.[18] For the hydrophobic sample, both the Au-SAM and the SAM-H_2O interfaces have a significant thermal impedance and both interfaces will contribute to the measured conductance value. On the other hand,

the hydrophilic SAM–H_2O interface is strongly coupled through the presence of hydrogen bonding and most of the measured interfacial conductance would be expected to arise from the Au-SAM interface.

Remaining Questions About Molecular-Scale Thermal Conductance

Over the last decade several interesting experimental studies focused on molecular-scale thermal conductance have been conducted and provided insight. Studying a property such as thermal conductance at the molecular scales is inherently difficult. Molecules are small objects, measured on the nanometer scale. Trying to measure energy flow from spatially distinct regions of molecules requires nanometer or even sub-nanometer spatial resolution. Additionally, the intrinsic time scale for energy transfer across nanometer length scales is picoseconds, making both high-spatial and high-temporal resolution critical to these experiments.

The theoretical predictions of Segal *et al.*[8] have provided several areas for experimental work to test the current models. The nature of these experiments, however, has limited the progress in this field and many questions remain unanswered about the physics of molecular-scale thermal conductance. Of central interest is the nature of heat flow at the molecular level. Predictions suggest ballistically transport for linear chain molecules, apposed to the diffusive behavior of bulk systems.[8] Furthermore, the energy-level mismatch between the vibrational states of the molecules and the phonon continuum of the solid comprising the interface will dictate the magnitude of the interfacial conductivity. An single-interface measurement of this type is yet to be made. The heat transport rate is also predicted to depend on the vibrational localization or the extent of delocalization. The vibrational modes are reliant on the molecular structure and

the dependence of heat transport on molecular structure is for the most part unknown.

1.3 Experimental Approach Of This Work

This thesis describes new experimental work that attempts to address some of the unanswered questions about molecular-scale thermal conduction. The method presented here to study the propagation of thermal energy into and through molecules is in some ways similar to both the work done by Smits *et al.*[15] and Ge *et al.*[18] A SiO_2/Cr/Au substrate, serving as an ultrafast heat bath, is flash-heated to several hundred degrees Celsius in a few picoseconds using a femtosecond laser pulse. A self-assembled monolayer, attached to the heat bath at one end by a Au-S bond, heats as thermal energy surges into the molecules from the heat bath. The resulting dynamics are monitored with picosecond resolution using vibrational sum-frequency spectroscopy – a nonlinear second-order vibrational spectroscopy. This spectroscopic technique can achieve sub-molecular resolution and provides a means to monitor a spatially distinct region of the molecules. As the monolayer heats, the increased amount of thermal energy leads to an increase in monolayer disorder. The presences of disorder measured at spatially distinct regions provides information about how the energy transfer occurs throughout molecular-scale systems.

Laser heating of these Au substrates results in an excited phonon distribution that is well-described by a temperature.[19] Thus, the term *heat bath* applies here in the same sense as it would to a macroscopic system. As mentioned above, the spectroscopic technique employed has the ability to probe a distinct spatial region

of a molecule. This allows thermal energy to enter the molecules comprising the monolayer at one end and its arrival at some other part of the molecule to be monitored at a later time.

This experimental approach has two important advantages. First, the energy-transport measurements are across only one SAM-Au interface, simplifying some of the interpretation. Secondly, the incorporation of SAMs provides a convenient modular aspect to this approach. This allows many different types of monolayers to be utilized, providing a means for systematic studies.

Thesis Layout

A brief introduction to vibrationally-resonant sum-frequency spectroscopy is presented in Chapter 2, with the goal of providing a general resource for future graduate students. The pertinent topics of this technique are discussed with enough depth that one should feel at ease with the terminology and the basic ideas behind sum-frequency spectroscopy. Chapter 3 is a presentation and discussion of the experimental equipment and technical aspects of this research. The time-resolved thermoreflectivity measurements conducted with a white-light continuum to characterize the ultrafast heat baths is found in Chapter 4. The molecular conductance experiments using alkanethiolate monolayers are presented in Chapter 5. Addtional experimental interfacial energy transfer work on benyzlthiolate monolayers can be found in Chapter 6. Chapter 7 discusses two-dimensional sum-frequency spectroscopy and contains several simulations of the molecular conductance experiments that aid in both the general understanding and in the interpretation of the experimental results. Chapter 8 serves as the Appendix and contains various computer scripts necessary for data collection and analysis.

1.4 References

1. Hellemans, A.; Bunch, B., The Timetables of Science, Simon and Schuster Inc., New York, 1988.
2. Burr, A. C., Notes on the History of the Concept of Thermal Conductivity, Isis, 20, 1, 1933. And the references within.
3. Kittel, C., Introduction to Solid State Physics, John Wiley & Sons, Inc., New York, 1953.
4. Stoner, R. J.; Harris, H. J., Phys. Rev. B, 48, 22, 1993. And the references within.
5. Cahill, D. G.; Ford, W. K.; Goodson, K. E.; Mahan, G. D.; Majumdar, A.; Maris, H. J.; Merlin, R.; Phillpot, S. R., Appl. Phys. Rev. 93, 2, 2003.
6. Ge, Z.; Cahill, D. G.; Braun, P. V., J. Chem. Phys. B, 108, 2004.
7. Segal, D.; Nitzan, A.; Hanggi, P., J. Chem. Phys. 119, 13, 2003.
8. Galperin, M.; Nitzan, A.; Ratner, M. A., Phys. Rev. B, 75, 155312, 2007.
9. Schwarzer, D.; Hanisch, C.; Kutne, P.; Troe, J., J. Phys. Chem. A, 106, 8019, 2002.
10. Schwarzer, Kutne, P.; Schroder, C.; Troe, J., J. Chem. Phys. 121, 4, 2004.
11. Ruan, C.; Vigliotti, F.; Lobastov, V. A.; Chen, S.; Zewail, A. H., PNAS, 101, 5, 2004.
12. Seidel, M. T.; Chem, S.; Zewail, A. H., J. Phys. Chem. C, 111, 4920, 2007.
13. Ioffe, Z.; Shamai, T.; Ophir, A.; Noy, G.; Yutsis, I.; Kfir, K.; Cheshnovsky, O.; Selzer, Y., Nature Nanotechnology, 3, 727, 2008.
14. Shamai, T.; Ophir, A.; Selzer, Y., Appl. Phys. Lett. 91, 102108 2007.
15. Smits, M.; Ghosh, A.; Bredenbeck, J.; Yamamoto, S.; Muller, M.; Bonn, M.; New J. Phys., 9, 390. 2007.
16. Deak, J. C.; Pang, Y.; Sechler, T. D.; Wang, Z.; Dlott, D. D., Science, 306, 5695, 2004.

17. Wang, R.; Segalman, R. A.; Maujumdar, A., Appl. Phys. Lett. 89, 173113, 2006.

18. Cahill, D. G., Rev. Sci. Instrum. 61, 2, 1990.

19. Ge, Z.; Cahill, D. G.; Braun, P. V., Phys. Rev. Lett., 96, 186101. 2006.

20. Brorson, S. D.; Fukimoto, J. G.; Ippen, E. P.; Phys. Rev. Lett. 59, 17, 1987.

2

Vibrationally-Resonant Sum-Frequency Spectroscopy

Vibrationally-resonant sum-frequency spectroscopy (VSFS) is a coherent second-order vibrational spectroscopy that can provide interfacial selectivity.[1–3] Within an isotropic material, only surface or interfacial molecules generate sum-frequency signals, making VSFS an immensely useful spectroscopic probe. As a vibrational spectroscopy it provides information about molecular structure and organization. These characteristics allow the behavior of interfacial molecules to be observed without being overwhelm by bulk signal.

2.1 Linear and Nonlinear Polarization

Under normal conditions an electric field oscillating at ω incident on a material generates a material polarization P that also oscillates at ω.

$$P(\omega) = \chi(\omega)E(\omega) \tag{2.1}$$

The linear susceptibility χ, a material property, dictates the degree of the induced polarization. In a system with no resonances, this material polarization subsequently reradiates light at ω. Depending on the material this is observed as either reflection, refraction or scattering. If a material is exposed to light sources of different frequencies simultaneously, then the field can be considered as a linear superposition of monochromatic light. Each field then generates a material polarization at its unique frequency, which then radiates independently.

$$E = \sum E(\omega) \tag{2.2}$$

$$P = \sum P(\omega) = \sum \chi(\omega)E(\omega) \tag{2.3}$$

As the strength of the incident electric field increases, the material polarization is no longer adequately described by a simple linear superposition. The material polarization is instead, best described as a power series,[4,5]

$$P = \chi E + \chi^{(2)}E^2 + \chi^{(3)}E^3 + \cdots, \tag{2.4}$$

where the first term, χE, is the linear polarization and the remaining terms, $\chi^{(2)}E^2 + \chi^{(3)}E^3 + \cdots$, are nonlinear polarizations.

Considering the simplest case of an intense monochromatic light source of peak strength $2E_\omega$,

$$E = E_\omega(e^{i\omega t} + e^{-i\omega t}) \tag{2.5}$$

the second order term becomes:

$$\chi^{(2)}E^2 = \chi^{(2)}E_\omega(e^{i\omega t} + e^{-i\omega t})E_\omega(e^{i\omega t} + e^{-i\omega t}) = \chi^{(2)}_{2\omega}E^2_\omega((e^{i2\omega t} + e^{-i2\omega t}) + \chi^{(2)}_0 2E^2_\omega \tag{2.6}$$

Accordingly, the material polarization has two second-order nonlinear components. One that oscillates and radiates at twice the original frequency corresponding to second harmonic generation. The second component corresponds to a static field generated within the material.

With the application of two intense monochromatic electric fields, such that:

$$E = E_{\omega_1}(e^{i\omega_1 t} + e^{-i\omega_1 t}) + E_{\omega_2}(e^{i\omega_2 t} + e^{-i\omega_2 t}) \tag{2.7}$$

the second order term becomes:

$$\chi^{(2)}E^2 = \chi^{(2)}_{2\omega_1}E^2_{\omega_1}((e^{i2\omega_1 t}+e^{-i2\omega_1 t})+\chi^{(2)}_0 2E^2_{\omega_1}+\chi^{(2)}_{2\omega_2}E^2_{\omega_2}((e^{i2\omega_2 t}+e^{-i2\omega_2 t})+\chi^{(2)}_0 2E^2_{\omega_2}$$

$$+2\chi^{(2)}_{\omega_1+\omega_2}E_{\omega_1}E_{\omega_2}(e^{i(\omega_1+\omega_2)t} + e^{-i(\omega_1+\omega_2)t}) + 2\chi^{(2)}_{\omega_1-\omega_2}E_{\omega_1}E_{\omega_2}(e^{i(\omega_1-\omega_2)t} + e^{-i(\omega_1-\omega_2)t}). \tag{2.8}$$

Notice the presence of the last two terms corresponding to the generation of new frequencies of $\omega_1 + \omega_2$ and $\omega_1 - \omega_2$. These are the second-order terms responsible for sum-frequency generation and difference-frequency generation, respectively.

Weak electric fields applied to a bulk material will induce a linear polarization

throughout the material. As the electric field alternates sign, the in the linear polarization of the material follows.[4] This is seen in the equation below.

$$P^{(1)} = \chi^{(1)} E_{\omega} \tag{2.9}$$

$$-P^{(1)} = \chi^{(1)}(-E_{\omega}) \tag{2.10}$$

However, the same argument applied to the second-order polarization provides a different picture.

$$P^{(2)} = \chi^{(2)} E_{\omega_1} E_{\omega_1} \tag{2.11}$$

$$-P^{(2)} = \chi^{(2)}(-E_{\omega_1})(-E_{\omega_1}) = \chi^{(2)} E_{\omega_1} E_{\omega_1} \tag{2.12}$$

Thus suggests that $-P^{(2)} = P^{(2)}$, which can only be true if $P^{(2)} = 0$. This requires $\chi^{(2)} = 0$ for bulk systems. Interestingly, the inversion symmetry of an isotropic system is broken at the interface and second-order signal can be generated from interfacial molecules.

2.2 Second-Order Material Susceptibility

Both the material polarization and the applied electric fields are vector quantities, thus the second-order susceptibility must be a rank three tensor with 27 elements.[4]

$$P_i^{(2)} = \chi_{ijk}^{(2)} E_{j,\omega_2} E_{k,\omega_1} \tag{2.13}$$

In the above equation, the ijk indices represent general cartesian coordinates. Depending on the symmetry of the interface not all of the ijk combinations

are unique. Consider an azimuthally isotropic, or a uniaxial, surface where any rotation leads to an identical surface. A C_2 rotation transforms $X \rightarrow -X$ and $Y \rightarrow -Y$.[4,6,7] Then $C_2 \cdot \chi^{(2)}_{xzz} = \chi^{(2)}_{-xzz} = -\chi^{(2)}_{xzz}$, which only happens if $\chi^{(2)}_{xzz} = 0$. Likewise, additional C_2 operations yield:

$$\chi^{(2)}_{xzz} = \chi^{(2)}_{yzz} = \chi^{(2)}_{zxz} = \chi^{(2)}_{zyz} = \chi^{(2)}_{zzx} = \chi^{(2)}_{zzy} = \chi^{(2)}_{xxx} =$$
$$\chi^{(2)}_{yyy} = \chi^{(2)}_{yyx} = \chi^{(2)}_{yxy} = \chi^{(2)}_{xyy} = \chi^{(2)}_{xxy} = \chi^{(2)}_{xyx} = \chi^{(2)}_{xxy} = 0.$$

Furthermore, C_4 rotation transforms $X \rightarrow Y$ and $Y \rightarrow -X$. Then $C_4 \cdot \chi^{(2)}_{xyz} = \chi^{(2)}_{y-xz} = -\chi^{(2)}_{yxz}$. X and Y can be exchanged because of the azimuthally isotropic then $-\chi^{(2)}_{xyz}$ becomes $-\chi^{(2)}_{yxz}$, which must be equal to $\chi^{(2)}_{yxz}$. Again, the susceptibility element must be equal and opposite simultaneously, making it zero by symmetry. Additional C_4 operations yield:

$$\chi^{(2)}_{xyz} = \chi^{(2)}_{yxz} = \chi^{(2)}_{zxy} = \chi^{(2)}_{zyx} = \chi^{(2)}_{yzx} = \chi^{(2)}_{xzy} = 0.$$

For a uniaxial interface only 7 $\chi^{(2)}$ elements are nonzero, and only 4 of the terms are unique.[9]

$$\chi^{(2)}_{zzz},\ \chi^{(2)}_{xxz} = \chi^{(2)}_{yyz},\ \chi^{(2)}_{zyy} = \chi^{(2)}_{zxx},\ \chi^{(2)}_{xzx} = \chi^{(2)}_{yzy}.$$

One can also derive the symmetry-unique non-zero $\chi^{(2)}_{ijk}$ elements by taking a detailed look at how these surface elements are related to the molecular properties. Consider an ensemble of interfacial molecules each having a unique reference frame distinct from that of the surface reference frame. The molecular hyperpolarizability β – the efficiency of an individual molecule to generate a second-order

signal – is defined in the local reference frame. The material nonlinear susceptibility is simply the ensemble-averaged hyperpolarizability of the interfacial molecules.[9]

$$\chi^{(2)}_{ijk} = N \sum_{abc} \langle (i \cdot a)(j \cdot b)(k \cdot c) \rangle \beta_{abc} \tag{2.14}$$

In the above equations, N is the molecular number density, $\langle \cdots \rangle$ denotes the ensemble average over the molecular orientations, and $(i \cdot a)$ is a projection of the molecular coordinate frame on to the surface coordinate frame.

The evaluation of the orientational average under specific symmetry restraints yields the unique non-zero $\chi^{(2)}$ elements for a given surface. It can also be shown that for an isotropic system, one with flat orientational distribution, that no second-order signal will be generated in the bulk. This is completely general and can be extended to any even-order nonlinear process. Only nonlinear process of odd-orders will generate bulk signals.

2.3 Molecular Hyperpolarizability

The molecular hyperpolarizability β describes the frequency-dependent ability for a molecule to generate a second-order signal. Using perturbation theory the hyperpolarizability can be depicted as sum-over-states expression. The corresponding expression within the dipole approximation for a vibrationally-resonant system is shown below.[8,9]

$$\beta_{ijk}(\omega_{vis}, \omega_{ir}) = \frac{-1}{2\hbar^2} \sum_{n,m} \frac{\mu^i_{0m} \mu^j_{mn} \mu^k_{n0}}{(\omega_n - \omega_{ir} - i\gamma_n)} \left[\frac{1}{(\omega_m - \omega_{sum} - i\gamma_m)} + \frac{1}{(\omega_m + \omega_{vis} + i\gamma_m)} \right] \tag{2.15}$$

The summation is over all n vibrational states and all m electronic states, μ_{n0} represents the dipole transition moment, ω_n is the corresponding transition frequency, and γ_n is the damping coefficient which includes contributions from both dephasing and lifetime effects.

When the infrared frequency is on resonance with a molecular vibration the hyperpolarizability experiences a significant resonant enhancement. This type of enhancement encodes vibrational information directly into the sum-frequency spectrum, allowing resonant frequencies and widths to be measured. While the sum-frequency spectrum does provide vibrational information, the spectrum is not equivalent to a traditional infrared spectrum. The differences will be apparent after a slight massage of the sum-over-states equation. By recognizing that

$$\frac{-i}{\hbar}\sum_{m}\left[\frac{\mu^{i}_{0m}\mu^{j}_{mn}}{(\omega_m-\omega_{sum}-i\gamma_m)}+\frac{\mu^{i}_{0m}\mu^{j}_{mn}}{(\omega_m+\omega_{vis}+i\gamma_{nm})}\right] \tag{2.16}$$

is a anti-stokes Raman transition, one can see that the molecular hyperpolarizability is the product of n^{th} vibrational transition and the related anti-stokes Raman transition.[8,9]

$$\beta_{ijk}(\omega_{vis},\omega_{ir})=\frac{-i}{2\hbar}\sum_{n}\frac{\alpha^{ij}_{0n}\mu^{k}_{n0}}{(\omega_{n0}-\omega_{ir}-i\gamma_{n0})} \tag{2.17}$$

Thus for a vibrational mode to be sum-frequency active, then it must be both infrared and Raman active.

The sum-frequncy selection rule provides a means for determining which molecular hyperpolarizabilities will contribute to a particular sum-frequency signal. As with the material susceptibility, the hyperpolarizability is a rank-three

tensor with 27 elements and many elements are zero by symmetry. For any molecular transition to be symmetry allowed, the integrated transition moment must be nonzero. Or in other words, the sum-frequency transition moment Γ_{SF} must transform as the totally symmetric irreducible representation Γ_{TS} of the molecular symmetry group.[7,9]

$$\Gamma_{SF} = \Gamma_{AR} \otimes \Gamma_{IR} \in \Gamma_{TS} \tag{2.18}$$

If a vibrational mode has a transition moment μ_z that transforms as B_1, then only Raman tensors elements that satisfy the above symmetry constraint will yield a nonzero hyper polarizability, i.e. B_1. For the symmetric CH_3 stretch of CH_3F, which transforms as A_1 in the C_{3v} point group, only α_{zz}, α_{xx} and α_{yy} Raman transitions result in nonzero hyperpolarizabilities. For the symmetric CH_3 stretch only β_{zzz}, β_{xxz} and β_{yyz} are allowed by symmetry to contribute to the sum-frequency signal. This type of simple analysis holds for non-degenerate vibrational modes. However, to find the nonzero hyperpolarizabilities for degenerate vibrational modes, one must consider how the entire component, i.e. β_{xxx}, transforms under all symmetry operations of the molecular symmetry groups.

2.4 Experimental Sum-Frequency Observables

In experiments the infrared and visible fields are incident on the interface with a polarization of either S or P. Likewise, the generated sum-frequency is measured in terms of S and P polarized light, and the measured material susceptibility is

one of the following:[10]

$$\chi^{(2)}_{PPP}, \chi^{(2)}_{SPP}, \chi^{(2)}_{PSP}, \chi^{(2)}_{SSP}, \chi^{(2)}_{PPS}, \chi^{(2)}_{SPS}, \chi^{(2)}_{PSS}, \chi^{(2)}_{SSS}$$

The indices denote the sum-frequency, the visible and the infrared polarizations, respectively.

The 8 different measurable second-order susceptibilities can be written as linear combinations of the cartesian-based second-order susceptibilities. P polarized light incident on a surface projects onto the X and Z directions and S polarized light projects onto Y direction[11], such that:

$$E_P = L^X_P E_X + L^Y_P E_Y$$

and

$$E_S = L^Y_S E_Y \tag{2.19}$$

The Fresnel coefficients L relate the electric fields from S and P polarizations to the local-field cartesian components at the surface. Ideally, the Fresnel coefficients would simply account for the vector projections, however, reflection and refraction of the incident fields lead to more complicated expressions. Various models which account for thin-film effects exist,[12,13] but for the current discussion the Fresnel coefficients will remain completely general.

One can break down the polarization-dependent sum-frequency signal accordingly:

$$I_{SSP} = |\chi^{(2)}_{SSP} E_{S,vis} E_{P,ir}|^2 = |\chi^{(2)}_{SSP} L^Y_S E_{Y,vis} (L^X_P E_{X,ir} + L^Z_P E_{Z,ir})|^2$$

$$= |(L^Y_{S,sum}\chi^{(2)}_{YYX}L^Y_{S,vis}L^X_{P,ir}E_{Y,vis}E_{X,ir} + L^Y_{S,sum}\chi^{(2)}_{YYZ}L^Y_{S,vis}L^Z_{P,ir}E_{Y,vis}E_{Z,ir})|^2 \tag{2.20}$$

Taking this further, for a surface with uniaxial symmetry $\chi^{(2)}_{YYX} = 0$ and the resulting signal is simplified.

$$I_{SSP} = |L^Y_{S,sum}\chi^{(2)}_{YYZ}L^Y_{S,vis}L^Z_{P,ir}E_{Y,vis}E_{Z,ir})|^2 \tag{2.21}$$

2.5 A Time-Domain Picture

VRSF spectroscopy is usually described in the frequency-domain, however, a time-domain description can be more intuitive when discussing ultrafast experiments. In this picture, the VRSF signal can be described starting with a completely general formulation of the second-order polarization and the second-order response function,[14]

$$P^{(2)}(t) = \int_{-\infty}^{t} d\tau_2 \int_{-\infty}^{\tau_2} d\tau_3 R^{(2)}(t,t_2)E(\tau_2)E(\tau_3), \tag{2.22}$$

where $R^{(2)}(t,t_2)$ is the response function and t_2 is the time delay between the two electric fields,[14]

$$R^{(2)}(t,t_2) = \left\langle \left[\left(\frac{i}{\hbar}\right)^2 \langle \Psi^{(0)}|VG(t-\tau_2)VG(t-\tau_3)V|\Psi^{(0)}(-\infty)\rangle + C.C. \right] \right\rangle. \tag{2.23}$$

V and G are interaction and time-evolution operators, respectively, and are shown below:

$$V = -\mu \cdot \epsilon \tag{2.24}$$

$$G(t) = \Theta(t) e^{(-iHt/\hbar)} \tag{2.25}$$

The material polarization can be rewritten after explicitly separating the individual Cartesian components and considering the contributing interaction orderings. Below is the I^{th} component of the polarization originating from the m^{th} vibrational mode:

$$P^{(2)}_{I,m}(t) = \int_{-\infty}^{t} d\tau_2 \int_{-\infty}^{\tau_2} d\tau_3 R^{(2)}_{IJK,m}(t, t_2) E(\tau_2) E(\tau_3). \tag{2.26}$$

Furthermore,

$$R^{(2)}_{IJK,m}(\tau_2, \tau_3) = R^{(2),L}_{IJK,m}(\tau_2, \tau_3) + C.C. \tag{2.27}$$

and,

$$R^{(2),L}_{IJK,m}(\tau_2, \tau_3) = \sum_{ijk} \sum_{n} M^{ijk}_{IJK}(t, \tau_2, \tau_3)[\mu_{0n} \cdot \hat{i}][\mu_{nm} \cdot \hat{j}][\mu_{m0} \cdot \hat{k}] K(t, \tau_2, \tau_3) \tag{2.28}$$

$$M = \int d\Omega_t \int d\Omega_{\tau_2} \int d\Omega_{\tau_3} [\hat{i}_{\Omega_t} \cdot I] P'(\Omega_t) [\hat{j}_{\Omega_{\tau_2}} \cdot J] P'(\Omega_{\tau_2}) [\hat{k}_{\Omega_{\tau_3}} \cdot K] P(\Omega_{\tau_3}) \tag{2.29}$$

$$K = \left[(\rho_{00} - \rho_{mm})_{\tau_3} \Theta(\tau_3) e^{-(i\omega_{m0} + \gamma_{m0})(\tau_2 - \tau_3)} \Theta(\tau_2) e^{-(i\omega_{n0} + \gamma_{n0})(t - \tau_2)} \right] \tag{2.30}$$

The response function, as written, is separated into two main parts, $M^{ijk}_{IJK}(t, \tau_2, \tau_3)$ and $K(t, \tau_2, \tau_3)$.

$M^{ijk}_{IJK}(t, \tau_2, \tau_3)$ contains all of the orientational dynamics the system may

undergo.[11,15] Starting with an ensemble distribution $P(\Omega_{\tau_3})$ defined at time τ_3, M describes the projection of the k^{th} unit vector of the molecular frame onto the K^{th} unit vector of the laboratory frame. The molecular ensemble is then allowed to evolve and the molecular coordinates are projected onto the laboratory coordinates. The ensemble dynamics are expressed as a conditional probability $P^{'}(\Omega_{\tau_2})$ – or more formally as $P(\Omega_{\tau_2}, (\tau_2 - \tau_3)|\Omega_{\tau_3})$ – which describes the orientational ensemble at time τ_2 with the explicit knowledge of the ensemble at a previous time τ_3.[11] In other words, this term accounts for changes in the transition probabilities due to molecular motion that may change the angle between the transition dipole moment and the electric field vector between interaction times.

The dynamics of the molecular coherences are described within the $K(t, \tau_2, \tau_3)$.[15] This term models how interactions with the electric fields generates and manipulates the molecular coherences, how the coherences dephase over time and how initial vibrational populations affect the generation of second-order signals.

After integrating the second field interaction and a slight massage, the response function begins to take on a more familiar form, where the second-order signal can be seen as a vibrational coherence which is subsequently scattered from,

$$R^{(2),L}_{IJK,m}(t, \tau_3) = \sum_{ijk} \alpha_{ij}\mu_k M^{ijk}_{IJK}(t, \tau_3)\Theta(\tau_3)e^{-(i\omega_{m0}+\gamma_{m0})(t-\tau_3)}(\rho_{00} - \rho_{mm}) \quad (2.31)$$

and

$$P^{(2)}_{I,m}(t; t_{VIS} - t_{IR}) = E_J(t - t_{VIS}) \int_{-\infty}^{t} d\tau_3 R^{(2)}_{IJK,m}(t, \tau_3)E_K(\tau_3 - t_{IR}) \quad (2.32)$$

At this point t_{IR} and t_{VIS} are used to describe the arrival time for the IR and VIS laser pulse used in vibrationally-resonant sum-frequency spectroscopy.

This second-order surface polarization can be inserted into Maxwell's equations as a source term which radiates.[5,8] The radiated field is then detected either in the time domain or the frequency domain. For time-domain detection, the signal must be heterodyned against a phase-stablized oscillator.[16] Alternatively, the signal can be detected in the frequency domain by a Fourier transfer via a spectrograph.[22]

2.6 As a Tool to Study Molecular Dynamics

Sum-frequency spectroscopy when conducted with ultrafast laser pulses provides a powerful technique able to measure non-equilibrium dynamics on length scales and time scales relevant to molecules. Resulting from the second-order nature of sum-frequency spectroscopy, signal is only generated in anisotropic environments such as surfaces and interfaces. Thus, in general, SFG reports spectral information about molecules within a-few-nanometer length scale. Additionally, the application of ultrafast laser pulses provides dynamical information with a time resolution approximately equal to the vibrational dephasing time T_2. While many studies utilize sum-frequency as an characterization tool for static and slowly evolving systems, few experiments incorporate this vibrational spectroscopy as a probe in pump-probe experiments.[17,18] This section aims to discuss the merit of sum-frequency as a probe and to illustrate what types of information can be obtained in this style of pump-probe scheme.

In a general pump-probe experiment, a pump creates a non-equilibrium situa-

tion that evolves until a new equilibrium state is achieved. The resulting dynamics are then probed at various time-delays after the system is pumped and the molecular-scale dynamics are subsequently inferred. The precision in which the molecular-scale dynamics can be determined depends greatly on the information density of the probing technique.

Vibrational-based spectroscopies are quite useful; the vibrational frequencies report information about the molecular structures and any changes in the local environment that may have occurred.[19–21] SFG shares this ability to follow changes in the molecular structure. As seen from §2.2.3, SFG is resonantly enhanced and as the local environment changes, the vibrational frequency ω_{0m} shifts in response.

Sensitivity to Vibrational Populations

Sum-frequency spectroscopies are also sensitive to vibrational populations. This sensitivity, however, is different from traditional linear vibrational techniques. Due to the coherent nature of this emitted signal, the SFG intensity is more sensitive to vibrational populations, following the relation of:

$$I_{SFG} \sim (\rho_{00} - \rho_{mm})^2. \tag{2.33}$$

For example, in a simple vibrational manifold consisting of only a two-levels, a small change in vibrational population δ – assuming initially $\rho_{00} = 1$ and $\rho_{mm} = 0$ – results in a corresponding intensity change,

$$I_{SFG} \sim (1 - 2\delta)^2. \tag{2.34}$$

Substituting explicit numbers, a 5% population change will result in apprximately 20% loss in signal strength. Thus, SFG is quite sensitive to changes in population. It should be noted that the vibrational manifolds for most molecules are not completely described by an idealized two-level system and that this calculation is a slight over estimate.

Further analysis also predicts that hot-band SFG signals from $2 \leftarrow 1$ transitions should be observable under certain circumstances. For small populations, $\delta \lesssim 5\%$, the red-shifted $2 \leftarrow 1$ peak will be only a few percent of the fundamental $1 \leftarrow 0$ peak. As δ increases to larger percentages, the $2 \leftarrow 1$ transition will be comparable in strength to the $2 \leftarrow 1$ transition. For this discussion, the molecular hyperpolarizabilities are estimated from the harmonic limit, where $\beta_{21} = 4\beta_{10}$. One can see that due to the coherent nature of the sum-frequency emission, SFG can serve as a non-invasive experimental tool for following vibrational populations or measuring vibrational lifetimes of molecules at surfaces.

Sensitivity to Molecular Order and Orientation

Sum-frequency signals, as second-order phenomena, are generated from only molecules in anisotropic media. This is a consequence of the even-order nonlinearity and can be traced back to the fact that the second-order material susceptibility is the ensemble average of the molecular hyperpolarizabilities presented in §2.2.2. The ensemble average $\langle (i \cdot a)(j \cdot b)(k \cdot c) \rangle$ can be written as a product of trigonometric functions using the set of Euler angles that connect the molecular coordinate frame abc to the laboratory coordinate frame ijk. In an isotropic system, the distribution of Euler angles that describe the molecular ensemble is flat, meaning there is an equal probability for all possible orientations. Preforming the required

integration shows that the ensemble average is exactly equal to zero by symmetry for a flat angular distribution. Therefore, SFG provides a method to determine, at least qualitatively and possible qualitatively, the amount of disorder present in a molecular system.

In pump-probe scheme, in which the pump resulted in a thermal gradient, incorporating SFG as a probe would allow the observation of the thermalization process. Assuming the interface or surface had an appreciable amount of initial order, then as energy flowed into the system, the amount of thermally-induced disorder would increase, resulting from increased random motion, and the SFG signal would decrease accordingly.

For those interested in calculating the sum-frequency signals for a system undergoing dynamics, further discussion of the orientational dynamics is necessary. Initially introduced in §2.2.5, M_{IJK}^{ijk} contains all the information and conditional probabilities about the orientational dynamics for an equilibrium measurement. In the event that the system is experiencing non-equilibrium dynamics, this term must be modified. An additional time dependence needs to be included to describe the system evolution after the pump pulse, but before the probe measurement. This is formally done by including another conditional probability term in Eq. 2.29. The evolution of the orientational dynamics can calculated either analytically or numerically depending on the type of system. An excellent starting point for understanding orientational dynamics is provided by Berne and Pecora.[11]

2.7 References

1. Shen, Y. R., Nature 337, 519, (1989).
2. Eisenthal, K. B., Chem. Rev., 1343, (1996).
3. Videl, F.; Tadjeddine, A. Rep. Prog. Phys., 68, 1095, (2005).
4. Boyd, R. W. Nonlinear Optics, 2^{nd} Ed. Academic Press, 2003.
5. Griffiths, D. J. Introduction to Electrodynamics, 3^{rd} Ed. Prentice hall, Upper Saddle River, New Jersey, 1999.
6. Harris, D. C.; Bertolucci, M. D. Symmetry and Spectroscopy: An Introduction to Vibrational and Electronic Spectroscopy. Oxford University Press, Inc. New York, 1978.
7. Bunker, P. R; Jensen, P. Molecular Symmetry and Spectroscopy, 2^{nd} Ed. NRC Research Press, Ottawa, 1998.
8. Shen, Y. R., The Principles of Nonlinear Optics, Wiley-Interscience, New York, 1984.
9. Moad, A. J.; Simpson, G. J. J. Phys. Chem. B. 108, 3548, 2004.
10. Begue, N. J.; Moad, A. J; Simpson, G. J., J. Phys. Chem. C, 113, 23, 2009.
11. Bern B. J.; Pecora, R., Dynamic Light Scattering: with Applications to Chemistry, Biology, and Physics. General Publishing Company, Ltd., Toronto, Ontario, 2000.
12. Hecht, E., Optics, 4^{th} Ed. Addison Wesley, San Fransisco, California, 2002.
13. Bloembergen, N.; Pershan, P. S. Phys. Rev. 128, 606, 1962
14. Mukamel, S. Principles of Nonlinear Optical Spectroscopy. Oxford University Press, Oxford, New York, 1995.
15. Ge, N.-H.; Zanni, M. T.; Hochstrasser, R. M. J. Phys. Chem. A., 106, 962, 2002.
16. Stiopkin, I. V.; Jayathilake, H. D.; Dordenyuk, A. N.; Benderski, A. V., J. Am. Chem. Soc., 130, 2271, 2008.

17. Smits, M.; Ghosh, A.; Bredendeck, J.; Yamamoto, S.; Muller, M.; Bonn, M.. New J. Phys., 9, 390, 2007.

18. Shang, X.; Nguyen, K. Rao, Y.; Eisenthal, K. B., J. Phys. Chem. C, 112, 51, 2008.

19. Shelby, R. M.; Harris, C. B.; Cornelius, P. A., J. Chem. Phys. 70, 1, 1979.

20. Zheng, J.; Kwak, K.; Fayer, M. D., Acc. Chem. Res., 40, 1, 2006.

21. Tanimura, Y.; Mukamel, S., J. Chem. Phys. 99, 12, 1993.

22. Rickter, L. J.; Petralli-Mallow, T. P.; Stephenson, J. P., Opt. Lett. 23, 1594, 1998.

3

Experimental

3.1 Laser System

This section describes the laser system components and any details pertinent to the success of the pump-probe experiments discussed within this thesis. The nature of the experiments – both ultrafast and nonlinear– required a laser system that could generate large-amplitude, short-duration pulses. This is most easily accomplished using an amplified Ti:Sapphire laser system.

Ti:Sapphire Oscillator

The fs-laser pulses for the entire system begin in the oscillator, a Model TS Ti:Sapphire kit laser (Kapteyn-Murnane Laboratories L.L.C.). The Ti:Sapphire oscillator rod is pumped by a continuous-wave visible laser Millennia Vs (Spectra-Physics) outputting 5 Watts centered at 532 nm. Passively mode-locked, the oscillator generates ∼100 fs pulses at ∼80 MHz. While this laser can produce ultrafast pulses with a total output of 500 mW, the energy per pulse or pulse

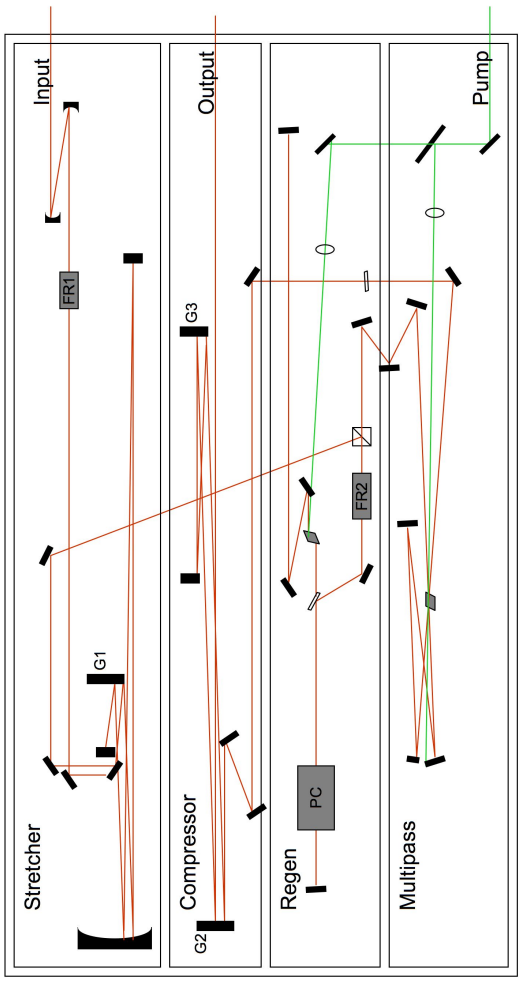

Figure 3.1: Schematic of the Titan-I amplification system - The main sections of the CPA amplification system are shown – stretcher, regenerative amplifier, multipass amplifier, compressor. The oscillator pulses enter the Titan-I at the *Input* point. The amplified pulses exit at the *Output* point. The 800-nm and 532-nm beam paths are shown in red and green, respectively. Faraday isolators are shown as FR, diffraction gratings as G, and the Pockels cell as PC.

energy is considerable low at ~ 5 nJ.

Chirped Pulse Amplification

The oscillator pulses are directed into the amplification system (Titan-I, Quantronix). The overall gain of this amplifier is 10^6. It is, therefore, necessary to stretch the pulses in time before amplification, limiting peak pulse power to avoid damaging the laser gain medium. This process is termed chirped pulse amplification (CPA). Shown in Fig. 3.1, the Titan-I consists of a stretcher, two amplification stages and a compressor. Each amplification stage has a Ti:Sapphire rod as the gain medium and is pumped by a common Q-switched, frequency-doubled Nd:YLF laser (Darwin, Quantronix) outputting 16 W or 160 mJ/pulse at 1 kHz.

The oscillator pulses are temporally stretched by a single-grating stretcher in a folded configuration. Making use of the large pulse bandwidth, the various frequency components are dispersed, sent slightly different path lengths, and then recombined spatially; the result is a pulse with positive chirp, that is the lower frequencies arrive first, followed by the higher frequencies. These pulses now have a long enough duration, $\sim$100 ps, such that when amplified, the peak power of each pulse is lower than the damage threshold of the gain medium. The stretched pulses are directed into the first of two amplification stages.

A consequence of the CPA technique is that the leading edge of the pulses experiences in most gain. This causes a change in frequency spectrum of the output pulses. To counter this effect, a pulse-shaping mask is used as a frequency filter in the stretcher, generally positioned in front of the folding mirror near the Fourier plain. The final alignment of this mask, done after the Titan-I system is aligned, is such that the amplified output spectrum is as Gaussian as possible,

while simultaneously minimizing the time-bandwidth product.

A Pockels cell, acting as an optical shutter, operates at 1 kHz and permits 1 out of every 8×10^4 of the stretched pulses into the first amplification stage – the regenerative amplifier. This type of amplifier is an optical resonator capable of lasing on its own. The stretched pulses in directed along the cavity path and acts as a "seed" to stimulate coherent photon emission. After ∼20 round trips in the cavity, the population inversion within the gain material is sufficiently depleted so that the pulse energy begins to decrease due to cavity losses. At this point, the Pockels cell then switches out the amplified pulse from the regenerative amplifier cavity. The total amplification of this stage is 10^5, generating pulse energies of $\sim300\mu$J. An advantage of using a regenerative amplifier is that it has stable cavity modes and thus highly-amplified pulses tend to maintain a near-TEM_{00} mode structure.

Considering the high repetition rate of the oscillator, the timing of the Pockels cell is quite important. The pulses from the oscillator are space ∼12.5 ns apart, meaning that the Pockels cell needs to switch from a completely off – $\lambda/4$-plate operation – to completely on – $\lambda/2$-plate operation – or vis-versa in < 12.5 ns. Either a timing error or an inadequate voltage will result in less-than desired switching of this electro-optical component. This can lead to the amplification of extraneous pulses or possibly to an incomplete switching-out of the main pulse. Undesired amplification of additional pulses, especially pre-pulses arriving before the main pulse, causes problems with efficiency and stability in nonlinear optical processes further along in the setup. Generally, the intensity ratio of the main pulse to other pulses or the contrast ratio, should be maintained at an minimum of 500:1 measured after the regenerative amplifier.

The final amplification occurs in the multipass stage, where the pulse traverses a gain medium twice, each time with a slightly different direction. This stage boosts the pulse energy from ∼300 μJ to ∼5 mJ. The pulses are then sent into the compressor, which utilizing a pair of matched gratings, removes the frequency chirp from the amplified pulses, resulting in ∼120-fs pulses.

For most of the discussed experiments, the output of the Titan-I was split prior to the compressor by a 50:50 beam splitter. The transmitted component traveled into the Titan-I compressor and was subsequently used for the probe pulses. The reflected component was output as is, and was sent to an auxiliary compressor (Clark-MXR, Inc.), which could be adjusted independently to generate a pumping pulse of varying duration (∼150 fs $\leq \tau_{Pump} \leq$ ∼10 ps).

Optical Parametric Amplifier

A portion of the compressed Titan-I output was used to pump an optical parametric amplifier (TOPAS, Light Conversion) – a non-linear optical device capable of generating tunable output. Within the TOPAS, a second-order stimulated down-conversion process takes a pump photon and generates two new lower-energy photons, the signal and idler photons. This process conserves energy, such that $\omega_{pump} = \omega_{signal} + \omega_{idler}$. And following convention, $\omega_{signal} > \omega_{idler}$. The tunability of the signal ranges such that $1150\mu m \leq \lambda_{signal} \leq 1600\mu m$. The signal and idler subsequently undergo mixing in a difference-frequency-generation module (Light Conversion) to generate tunable mid-infrared radiation, $\omega_{DFG} = \omega_{signal} - \omega_{idler}$

Detailed information about the TOPAS can be found in the manual. Therefore, the following description is brief, including only the basic operation. Inside the TOPAS, two beam splitters portion the pump beam into three separate paths

– A,B and C – with a relative intensity ratio of ∼90:9:1. The C beam is passed through a nonlinear BBO crystal three different times. For each pass this beam is focused tightly using various curved mirrors to increase the peak intensity. These first three passes generate a visible amount of broadband superfluorescence, which is frequency filtered by reflection from a diffraction grating and spatial filter. This filtered superfluorescence serves as a seed to stimulate subsequent downconversion processes. Both the seed and the B beam are focused into the nonlinear crystal together in a collinear geometry, overlapped spatially and temporally. The result is an amplification of the seed energy. The final amplification occurs in the fifth pass, when the forth-pass output is again overlapped spatially and temporally in a collinear geometry with the A beam. By changing the angle of the diffraction grating, i.e. changing the seed frequency, and by changing the non-linear crystal angle to optimize the phase-matching angle, the signal and idler of the TOPAS are tunable in frequency. The signal and idler are then recombined spatially and temporally in a non-collinear geometry in a $AgGaS_2$ crystal to generate the mid-IR source. Again, the crystal angle must be tuned for optimal phase matching.

Fortunately, the TOPAS has a computer interface and once a calibration file – consisting of a grating angle, crystal angles and a temporal delay positions specific for each mid-IR wavelength – has been created, then changing the output of the TOPAS consists of simply changing a number in the computer. The day-to-day TOPAS maintenance is minimal. The pump pointing needs to be re-optimized daily by adjusting two steering mirrors, driven by fine-positioning actuators (PICOMOTOR, Newport). During this process, one should ensure that the first three passes through the crystal must pass in the same vertical plane. Also, the vertical position of the third pass should be such that it strikes the rotation axis

of the diffraction grating. Normal output pulse energy of the difference-frequency at $\sim$ 3 μm ranges between 20-25 μJ, depending on the initial alignment during the calibration process.

3.2 Sample Preparation

Substrate Fabrication

The samples were fabricated on borosilicate glass substrates (Chemglass) with dimensions of 50 x 50 x 1.6 mm^3. The glasses slides were cleaned in 3:1 mixture of concentrated sulfuric acid (H_2SO_4, Fisher Scientific) and 30% hydrogenperoxide solution (H_2O_2, Mallinckrodt Chemicals) for several hours to remove any organic residue. The substrates were rinsed with copious amounts of deionized water followed by electronics-grade isopropanol ($(CH_3)_2CHOH$, Fisher Scientific) and then dried with either nitrogen (N_2, S. J. Smith Welding Supply) or argon (Ar, S. J. Smith Welding Supply).

Both chromium and gold were deposited onto the glass substrates using an electron-beam deposition system (Temescale) in the Materials Research Laboratory located on the University of Illinois campus. The film thicknesses and deposition rates were measured *in situ* with a quartz-crystal deposition monitor (Dektak). Deposition rates were kept at 0.1 $Å s^{-1}$ and 1.5 $Å s^{-1}$ for chromium and gold, respectively.

Self-Assembled Monolayers

Self-assembled monolayers (SAMs) have become ubiquitous in chemical-related research fields. These one-molecule-thick films, hence monolayer, undergo sponta-

neous self-assembly forming a densely packed surface.[1,2] The exothermic nature of the chemisorption process between the molecules and the metal-based substrate drives the monolayer formation with minimum effort. The most common type of SAM consists of an organosulfur compounds, such as thiols, disulfides, and sulfides, deposited on prepared gold films. An enormous amount of literature on SAMs and related topics exists, however, the reviews of Love, *et al.* and Schreiber and the references within are particularly good and continue to serve as useful sources for information.[3,4]

Monolayers serve as ideal models to systematically study the structural effects of molecules on material or interfacial properties. Due to the relative ease of synthesizing thiol-based compounds, there are hundreds of possible thiolate monolayers, in essence creating a structural library of well-characterized building blocks. For these reasons, the experiments discuss in this thesis employee SAMs as model system to study how energy transfer occurs through interfaces at the nanoscale. The table below presents the molecules used for monolayer formation, along with its abbreviation and source.

Several of the molecules were synthesize in lab by Hiroki Fujiwara following standard procedures in the chemical literature. 1-Tetracosanethiol (C24) was synthesized from tetradecanoic acid. 4-Phenylbenzylthiol (BPhT) was synthesized starting with 4-phenylbenzyl alcohol (Chem-Impex, International, Inc.) following the procedures in ref 5 and ref 6. Phenylpropylthiol (B3T), phenylbutylthiol (B4T), and phenylpentylthiol (B5T) were synthesized from the corresponding bromides (TCI America, Co., Ltd.) using the procedure of ref 6.

All thiols studied were used without further purification. Most of the thiols were dissolved in deoxygenated ethanol at a concentration of $\sim$1 mM. Due to

Molecule	Abbreviation	Source
1-hexanethiol	C6	Sigma-Aldrich Chemical Co.
1-octanethiol	C8	Sigma-Aldrich Chemical Co.
1-decanethiol	C10	Sigma-Aldrich Chemical Co.
1-dodecanethiol	C12	Sigma-Aldrich Chemical Co.
1-tetradecanethiol	C14	Sigma-Aldrich Chemical Co.
1-hexadecanethiol	C16	Sigma-Aldrich Chemical Co.
1-octadecanethiol	C18	Sigma-Aldrich Chemical Co.
1-eicosanethiol	C20	Sigma-Aldrich Chemical Co.
1-tetracosanethiol	C24	Synthesized*
benzenethiol	BT	Sigma-Aldrich Chemical Co.
benylthiol	B1T	Sigma-Aldrich Chemical Co.
2-phenylethanethiol	B2T	Sigma-Aldrich Chemical Co.
3-phenylpropylthiol	B3T	Synthesized*
4-phenylbenylthiol	B4T	Synthesized*
5-phenylpentylthiol	B5T	Synthesized*
2-methylphenylthiol	2MBT	Sigma-Aldrich Chemical Co.
cyclohexanethiol	CHT	Sigma-Aldrich Chemical Co.
4-nitrobenzenethiol	NBT	Sigma-Aldrich Chemical Co.
4-phenylbenzenethiol	BPhT	Synthesized*
4-biphenylbenzenethiol	TPhT	Frinton Laboratories

Table 3.1: Molecules for Self-Assembly - The above molecules are used in the formation of self-assembled monolayers for energy transfer studies. *See this section for the starting reagents for the thiols listed as synthesized.

poor solubility in ethanol, BPhT was dissolved in an ethanol-benzene mixture and TPhT was dissolved in cyclohexanol to improve solubility. The substrates were soaked in the thiol solution for twenty four hours to allow complete self-assembly of thiolate monolayers. The SAM-coated substrates were washed extensively with ethanol and then were stored in ethanol until needed for the laser measurements.

The quality of the monolayer, broadly defined using the packing density and the monolayer order as metrics, was determined qualitatively by contact-angle measurements and the sum-frequency spectrum. On a well-packed hydrophobic monolayer, a drop of water will exhibit a substantially larger contact angle than a water droplet on a poorly-formed monolayer.[2] Additionally, the strength and the presence of vibrational resonances in the sum-frequency signal is a good indication of a well-ordered monolayer. For example, the observation of methylene peaks, is clear evidence that the monolayer order is less-than ideal;[7,8] this occurred infrequently and these samples would then be discarded.

3.3 Sample Motion

For all experiments, the samples were attached to a motorized mount to avoid optical damage associated with the beams dwelling on the same spot for an extended time period. Without continuos motion, both the monolayer and substrate experienced degradation. The motion rate was chosen so that the sample surface moved approximately one pump-beam diameter ($\sim$500 μm) between 1 kHz laser shots, or a linear speed of $\sim$50 cm/s. Even with this precaution, after enough time elapsed the samples would evidence damage.

The molecular conductance experiments on the alkanethiolate monolayers

used a relatively simple, home-built mount capable of only rotational motion which was then coupled with a manually-operated translation stage. While in principle this stage work, only the outer portion of the sample had the required linear speed, leaving the inner-most portion of the sample unused. The other experiments utilized two computer-controlled translation stages (Compumotor, Parker Hannifin Corp.) driven by servo motors and controllers (Gemini Servo, Parker Hannifin Corp.); one stage for horizontal motion and the other for vertical motion. A computer script, written by Alexi Lagutchev, drove each stage in a sinusoidal motion with slightly different frequencies, resulting in sample motion that traces out a Lissajous curve. See the Appendix for a copy of this script. The exact curve is sensitive to the ratio of frequencies and as the ratio approaches unity the figure traces out more and more of the sample area.

3.4 Thermoreflectance Experiments

Experimental Layout

The dual-beam white-light spectrometer layout for the thermoreflectance experiments is shown in Fig. 3.2 and is based on the amplified Ti:Sapphire laser system discuss in §3.1. A fs white-light continuum is generated and then split into dual beams. The signal beam was reflected from a flash-heated region of the Au sample and the reference beam was reflected from a nearby region not flash-heated. The two probe beams were sent to a common 0.5-m imaging spectrograph (Chromex, Inc.) equipped with a CCD array detector (Andor Technology).

The 800-nm pump pulses are compressed in the auxiliary compressor and travel down an optical delay line (Gaertner Scientific Corp.) adapted with a

computer-controlled translation stage (Accudex, Aerotech, Inc.) before arriving at the sample. The pump-probe delay can be adjusted between -10 ps to 200 ps via computer with step-size as small as several femtoseconds. Additionally, the pump pulses travel through a computer-controlled mechanical shutter (Uniblitz, Vincent Associates) capable of sub-milisecond switching.

The flash-heating pulses are incident on the back surface of the substrates – opposite that of the Au – at $\sim$45° with respect to the surface normal. The probing pulses, in a chevron arrangement, are focused onto the front side of the substrates with a single 15-cm focal-length lens, also making an angle of $\sim$45°. This geometry minimizes differences in the transit time of the pump and the probe pulses as they traverse the sample and increases the intrinsic time resolution of the measuring apparatus.

Generation of White-Light Continuum

The remainder of the Titan-I output was used to generate the white-light probe beams. Shown in Fig. 3.3, a fs 800-nm pulse passed through a variable attenuator composed of a $\lambda/2$-wave plate and an ultrafast thin-film polarizer. The attenuated pulse is then focused by a lens ($f = 15$ mm) into a 1-mm-thick sapphire window. A 5x microscopic objective collected and collimated the divergent white-light continuum.

This configuration provided a means for easy alignment and pulse power adjustment. As the power level was increased to the WL-generation threshold, a faint beam of single-filament WL was observable. A slight increase in power produced a brighter beam with additional concentric rings of various colors, caused by stimulated Raman scattering. Further increases in power resulted in a dynamic

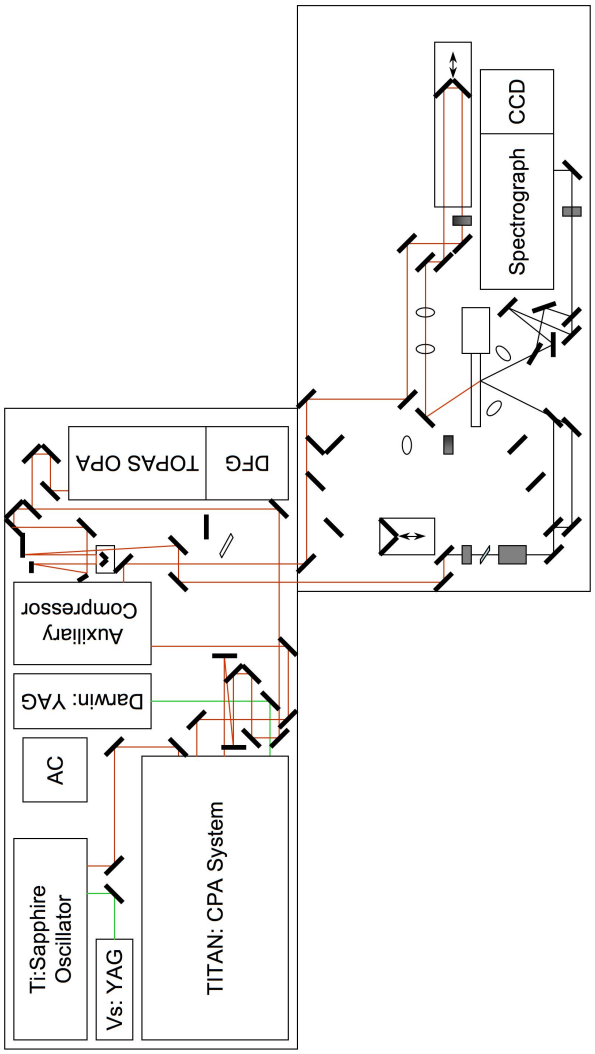

Figure 3.2: Optical layout for thermoreflectance experiments - This layout shows the entire laser setup spread across two different laser tables. Two 800-nm laser paths are shown in red; one is the fast-heating pulse, which travels through the axillary compressor and down an optical delay before impinging on the sample. The other 800-nm laser path travels to the white-light-generation apparatus. The white-light paths for the signal and the reference beams are shown in black. The other optical components shown are used in the molecular conductance experiments.

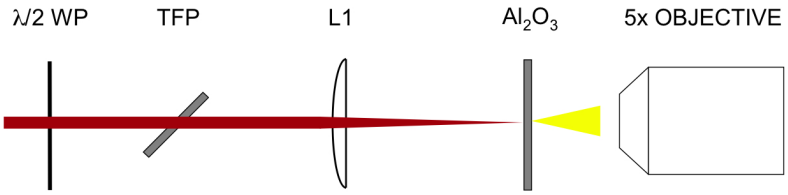

Figure 3.3: Generation of white-light continuum - The optical components are as follows: $\lambda/2$ WP is a rotatable half-wave plate, TFP is a ultrafast, thin-film polarizer, L1 is a X-cm-focal-length lens, Al_2O_3 is a sapphire window, and the 5× OBJECTIVE is a 5× microscope objective.

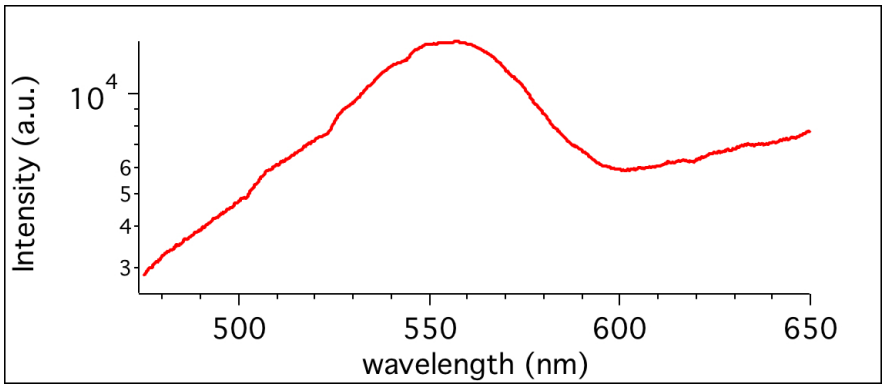

Figure 3.4: Spectrum of white-light continuum - Shown here is a typical white-light continuum spectrum obtained from the white-light-generation apparatus shown in Figure 3.3. The spectrum extends further into the red region of the spectrum, but the spectral range shown here is the maximum allowed with the diffraction gratings in use. Note the intense spectral feature around 550 nm, this is most likely extra intensity caused by other non-linear processes such as simulated Raman scattering.

show of brilliant colors, caused by the interference of multifilament WL generation. All experiments were conducted in the more-stable single-filament regime, using powers just below the multi-filamentation threshold. A typical spectrum of the WL continuum after one reflection from a gold mirror is shown in Fig. 3.4. Aside from minor laser-based fluctuations, the spectral shape was stable for the duration of all experiments, up to 24 hours – nothing longer was attempted. Optical damage of the sapphire window was rare, generally only occurring in the multifilament regime during the initial alignment. In this case, the window was simple rotated to a fresh spot.

By using refractive optics for collecting and focusing the white-light continuum, the probe beam had a noticeable amount of positive chirp. In retrospect, the degree of chirp could have been minimized by using reflective optics, such as off-axis parabolic mirrors. To independently quantify the amount of chirp present within the pulse, one would generally measure this by Kerr-gating the white-light continuum with another femtosecond pulse. However, this measurement requires polarizers with high extinction ratios, 10^6, that were unavailable.

Pulse Timings

For any pump-probe experiment, finding the exact path length of the pump and probe pulses such that both pulses are incident on the sample simultaneously is important. This point marks the zero-delay time for the data series. Nonlinear interactions between the pump and the probe pulses in various material are often used to extract this value. For a fs white-light continuum and a fs 800-nm pulse, Kerr gating could have been employed to find the simultaneity point, however, this was unnecessary. Instead the lens and microscopic objective were removed

from the white-light generation setup, described in Figure 3.3, allowing the fs 800-nm pulse to be focused down at the sample plane. Here both the 800-nm pump pulse, the 800-nm probe pulse – used to generate the white-light continuum – and a mid-IR pulse were spatially overlapped in an approximately 300-μm-thick $LiNbO_3$ powder sample suspended in a transparent polymer. The optical delays of both 800-nm pulses were independently adjusted to arrive simultaneously with the mid-IR pulse. This process was monitored either by eye or with the aid of the spectrograph and CCD. At the simultaneity point, the $LiNbO_3$ would generate the sum frequency, observable at $\sim$ 650 nm. The two 800-nm pulses, having been synchronized with a common third pulse, were then overlapped themselves. The optics that had been previously removed were then re-inserted to generate the white-light continuum. This, of course, changes the pulse timings due to difference between the refractive indices of air and glass. Thus, the optical delay of the pump pulse must be increased by $\sim$ 24 ps to compensate the extra delay from the additional optics in the probe path. The pulse timings can be further fine tuned after the first data run.

Data Collection Parameters

Both the signal and the reference spectra were collected with two 15-cm lenses and recorded simultaneously on a common CCD array detector. To do this, the spectra had to be well separated on the CCD and strongly attenuated to limit any bleeding of one signal into the other during CCD readout. The separation on the CDD was kept to a minimum of 50 pixels and the signal-reference contamination was checked prior to any data collection.

Typical experimental parameters are as follows: acquisition time $t = 1$ s,

spectrograph slit $l = 250$ μm and the spot sizes (FWHM) ~ 300 μm $\times$ 450 μm and ~ 100 μm $\times$ 150 μm for the pump and probe beams, respectively. The probe beam size was measured using a variety of filters to insure that all components of the white-light bandwidth were well focused. For each pump-probe delay, signal and reference spectra were collected multiple times with and without the pump. To expedite the data collection process, a short script was used to collect and save the spectra, to move the delay line and to open and close the pump shutter. This script is included in the Appendix.

It should be noted that the slit width is not, in practice, the limiting factor in spectral resolution for this experiment. The signal beam is focused to $\sim$100 μm at the slit, and thus, the resolution is $\sim$5 pixels on the CCD – the pixel width is 25 μm. Depending on the diffraction grating used, this translates into different spectral resolutions. For calibration purposes, the slit is narrowed and the signal beam is centered on it. Due to slight imperfections in the planarity of the sample motion relative to the collection optics, the signal beam walks slightly, $<$25 μm, at the spectrograph slit. The slit is widen to limit additional intensity fluctuations, with the downside of smearing the spectral resolution by an additional pixel.

3.5 Molecular Conductance Experiments

Experimental Layout

The ultrafast flash-thermal molecular conductance apparatus is illustrated in Fig. 3.5. Similar to the thermoreflectance setup, the thermal conductance apparatus is based on the amplified Ti:Sapphire laser system discuss in §3.1. There are, however, several differences between these two setups.

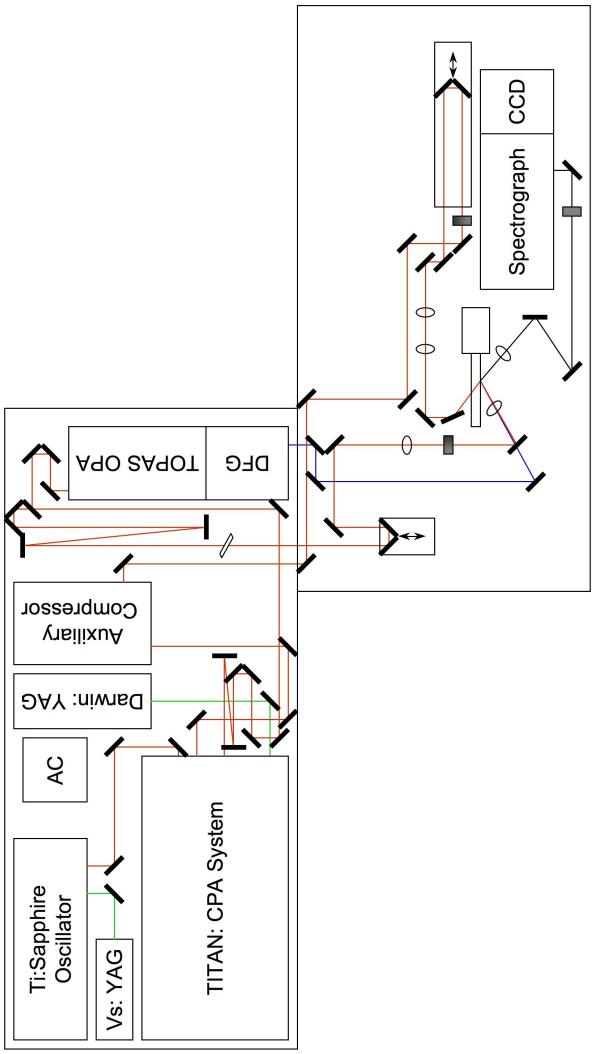

Figure 3.5: Optical layout for sum-frequency experiments - Similar to the layout shown in Figure 3.2, the optical layout for the molecular conductance experiments spans two different optical tables. The output of the TITAN-I CPA amplifier is split into two beams, one to serve as the pump, the other to generate the probe beams. The pump is independently compressed in the auxiliary compressor and then sent down an optical delay line before arriving at the sample. The other beam, used to generate the probe beams, is split. One component pumping an optical parametric amplifier to generate a tunable mid-infrared source. The other component travels through an etalon and emerges as a narrow-band source. Both probe beams are then focused onto the sample. The sum-frequency signal is then collected, then dispersed by a spectrograph and detected on a CCD.

The molecular conductance experiments employ vibrationally-resonant sum-frequency spectroscopy (VSFS) or sometimes simply referred to as sum-frequency generation (SFG). The compressed portion of the Titan-I output is split into two beams with a 60:40 ratio. The larger component pumps the OPA to generate tunable mid-IR pulses. The smaller portion is directed through an etalon used as a pulse shaper to create narrow-band 800-nm light. These two pulses are spatial and temporally overlapped at the sample plain and act as a probe pair. The flash-heating pulses are created as discussed in §3.4 and are incident on the back surface of the substrates – opposite that of the Au – at $\sim$60° with respect to the surface normal. The probing pulses are incident on the front side of the substrates at $\sim$60°. The generated sum-frequency emission was collected and dispersed by a spectrograph before being imaged on a CCD array.

Generation of Narrow-Band Visible Pulses

To observe an intrinsic rather than instrument-limited vibrational line width $\Delta\nu$, the non-resonant visible pulse must have an appreciably smaller bandwidth than that of the vibrational transition. Alternatively, in the time-domian, the narrow-band visible duration should be significantly longer in duration than the vibrational coherence. The narrow-band visible pulses were created by passing 800 nm pulses of 120 fs duration through a Fabry-Perot etalon with a free-spectral range of 500 cm^{-1} and a spectral bandpass of 6.7 cm^{-1} FWHM. The resulting laser pulses had energies of 20 μJ and were time-asymmetric; the leading edge of the pulse had a 120-fs rise, while the trailing edge decayed with the characteristic exponential of $\sim$0.8 ps as dictated by the etalon.

Pulse Timings

There are three different laser pulses for these experiments – one pumping pulse and two probe pulses – and thus two different pulse timings to adjust. The coarse timings are conducted similar to those discussed in §3.4. These delays are further fine tuned by replacing the $LiNbO_3$ alignment sample with a $Au/Cr/SiO_2$ substrate and optimizing the non-resonant second-order signal that is generated at the Au surface.

Polarization Considerations

The molecular conductance experiments employ molecular monolayers chemisorbed to mirror-like Au substrates. And thus, the SFG intensity for all polarization combinations, except *ppp*, are prohibitively weak.[8] The reason for this has to do with the Fresnel coefficients for electrical conductors, gold included. Good conductors also make good mirrors, and tend to reflect a large fraction of the incident light. For an electric field with a polarization parallel to the surface, the reflected light also experiences a phase shift of nearly π. Following classical electromagnetic theory, the electric field E experienced by the monolayer is a superposition of both the incident and reflected field $E = E_i + E_r$ or $E = (1 - r)E_i$ and is approximately zero for a polarization parallel to the surface.[9] The perpendicular polarization components of electric fields do not suffer this phase shift. According, the IR and visible pulses are horizontally polarized with respect to the optical table and are *p*-polarized with respect to the sample.

Phase-Matching Angle

The nonlinear mixing of the two probe photons in the molecular monolayers generates a new photon at the sum-frequency. This process must conserve both the energy and momentum of the initial photons.[10] The conservation of energy is easily observed, $\hbar\omega_{SFG} = \hbar\omega_{IR} + \hbar\omega_{VIS}$ with the aid of a calibrated spectrograph. The conservation of momentum, on the other hand, is observed by the directed emission in the phase-matching direction. This direction can be calculated using the k-vectors of the two probe beams, $k_{SFG} = k_{IR} + k_{VIS}$. In general, two sum-frequency signals will propagate away from the sample – one as a reflection direction, the other in the transmitted direction. The intensity ratio of the reflected and transmitted signals is dictated by the Fresnel coefficients for that particular interface.

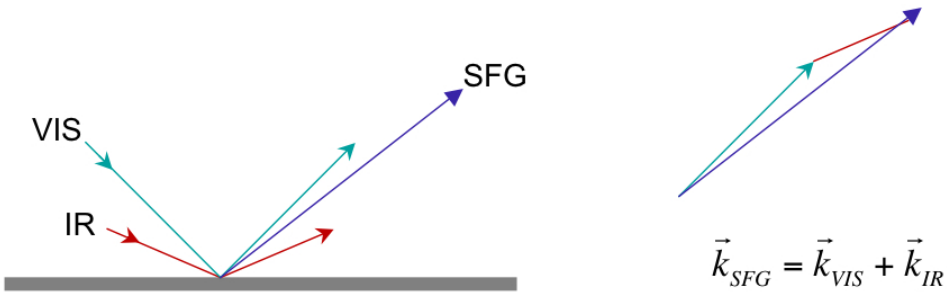

Figure 3.6: Phase-matching schematic - The schematic on the left provides a generalize picture of the sum-frequency signal, labeled SFG, being emitted at the phase-matched angle in a reflected geometry. The vector addition on the right shows how this phase-matched angle is determined.

One could, in theory, calculate exactly the direction of signal propagation and preform the initial alignment of the collection optics accordingly. Fortunately, this was unnecessary. Using a 1-mm-thick polycrystalline ZnS window,

the sum-frequency signal was visible by eye and the collection optics could easily be aligned.

Data Collection Parameters

SFG measurements were made using a femtosecond IR pulse and a picosecond 800 nm visible pulse. The IR pulses had a pulse energy of 15-25 μJ, depending on the center frequency, a duration of 200 fs and a spectral width (FWHM) of $\sim$150 cm^{-1}. This beam was focused to a $1/e^2$ beam diameter of 200 μm at the sample plain. The visible pulses had a pulse energy of 2.5 μJ and a spectral shape as discusses in §3.5.2. The visible beam was also focused to a spot-size of 200 μm. The IR and visible beams were incident on the sample at a 60° angle, so on the sample surface the SFG footprint was an approximately elliptical region 400 x 200 μm^2.

For the first several molecular-conductance experiments, the heating laser pulses were obtained by stretching an 800 nm pulse of 120 fs with a pair of high-index SF10 flint glass equilateral prisms spaced about 1 m apart, to a duration of $\sim$500 fs. After the pulse stretcher, the beam shape was elliptical with an eccentricity that approximately matched the SFG beam footprint. The heating pulses were sent down an optical delay line and were then weakly focused on the back side of the sample at normal incidence. The heating pulse energy was 120 μJ and the beam diameter was about twice as large as the probe beams, ensuring near-uniform heating over the region probed by SFG. Soon after completing the experiments discussed in Chapter 5, the auxiliary compressor was installed and the subsequent heat pulses were compressed independently. This arrangement limited unnecessary power losses suffered through the prism-pair stretcher.

The pump-pulse energy needed to produce damaged spots on the Au surface that had once clearly been melted was about 100 μJ for an elliptical spot with axes ($1/e^2$) 700×350 μm^2 (h×v). The flash-heating data presented in Chapter 5 were acquired using 80 μJ pulses. Based on an Au melting temperature of 1064 C, we estimated a temperature jump $\Delta T \approx 800$ K with 80 μJ pulses. However, after many thousands of pulses, the thin metal substrates developed faint damage tracks due to some unknown multiple-pulse interaction with the Au-Cr layers. The experiments discussed in Chapter 6 were taken with a pump-pulse power equivalent to 60 μJ, which allowed for longer signal-averaging times. See Chapter 4 for additional discussion of the temperature jumps experienced by the monolayers.

An inert-atmosphere purge was used to extend SAM lifetime, presumably by eliminating ozone. The SFG spectra were acquired with a 0.5 m spectrograph (Chromex) and thermoelectrically-cooled CCD detector (Andor). The normal CCD temperature was -65° C. The acquisition time for each spectrum depended on the intensity of SFG signal, which varied between monolayers, but typically was in the 4 to 10 s range.

3.6 References

1. Dubois, L. H.; Nuzzo, R. G., Annu. Rev. Phys. Chem. 43, 437, 1992.
2. Bain, C. D.; Troughton, E. B.; Tao, Y.-T.; Evall, J.; Whitesides, G. M.; Nuzzo, R. G., J. Am. Chem. Soc., 111, 1, 1989.
3. Love, J. C.; Estroff, L. A.; Kriebel, J. K.; Nuzzo, R. G.; Whitesides, G. M., Chem. Rev., 105, 1103, 2005.
4. Schreiber, R., Prog. Surf. Sci., 65, 151, 2000.
5. Tongkate, P.; Pluempanupat, W.; Chavasiri, W. Tetrahedron Lett., 49, 1146, 2007.
6. Han, C.-C.; Balakumar, R. Tetrahedron Lett., 47, 8255, 2006.
7. Hirose, C.; Haydock, S.; Bain, C. D.; Vibr. Spectrsc., 24, 109, 2000.
8. Patterson, J. E.; Dlott, D. D. J. Phys. Chem. B. 109, 5045, 2005.
9. Hecht, E., Optics, 4^{th} Ed. Addison Wesley, San Fransisco, California, 2002.
10. Shen, Y. R., The Principles of Nonlinear Optics, Wiley-Interscience, New York, 1984.

4

Thermoreflectance of Ultrafast Heat Baths[1]

4.1 Introduction

An interesting situation arrises when metals are heated with laser pulses of sub-picosecond duration. The laser-heating duration and the electron-phonon thermalization occur on similar time scales.[1,2] The electric field of the laser pulse couples to the metal electrons within the skin depth, which heats the metal electrons to an elevated temperature. While on the sub-picosecond time scale, the lattice temperature or phonon temperature remains essentially unchanged.[2] Electron-photon coupling on the picosecond time scale leads to localized thermalization. This phenomenon is usually discussed within the context of the two-temperature model.[1–3]

To characterize the electron-phonon thermalization time for the specific sub-

[1]Parts of the research presented here have been previously published as: Carter, J. A.; Wang, Z.; Fujiwara, H.; Dlott, D. D., J. Phys. Chem. A, 113, 2009

strates used throughout this thesis, time-resolved thermoreflectance (TRTR) technique was used to monitor this process. As the electron and phonon temperatures change in time, the surface reflectance or absorption changes in time. Thus, TRTR measurements provide the thermalization time scales for the metal substrates employed as ultrafast heat baths.

Two-Temperature Model

As mentioned above, femtosecond laser heating of Au is best described by the two-temperature model.[1,3] For small ΔT of a few Kelvin, the laser pulse excites a small fraction of the conduction electrons, which thermalize in a few femtoseconds through electron-electron interactions.[4,5] These hot electrons have a mean free path, such that they extend further into the material than just skin depth of the photons. For a laser pulse of ∼100-fs duration, the local electrons are well described by a Fermi distribution of an elevated temperature T_e throughout the pulse duration.

For temperature jumps of several hundreds of Kelvin, it is necessary to excite a much large fraction of the conduction electrons, including some of the *d*-band electrons.[6,7] Interactions between the conduction electrons and between the electrons and the *d*-band holes retard the electron-phonon equilibrium.[6,7] According to the model of Jiang and Tsai[3], for a final temperature near 1000 K, the electron temperature should initially reach a supprisingly-high peak temperature of $\sim 2 \times 10^4 K$.

The below coupled first-order differential equations describe the two-temperature model in general.[1] Exactly how the parameters of the two equations are expressed determines the ranges of temperature excursions where this model maintains va-

lidity.

$$C_e(T_e)\frac{\partial T_e}{\partial t} = \nabla[k_e(T_e)\nabla T_e] - G[T_e - T_p] + S(z,t) \tag{4.1}$$

$$C_p(T_p)\frac{\partial T_p}{\partial t} = G[T_e - T_p] \tag{4.2}$$

The expressions obtained by Jiang and Tsai[3] allow this model to extend reasonable well to temperatures near the melting point of a metal. C_e and C_p represent the electron and phonon heat capacities, $k_e(T_e)$ describes the temperature-dependent electron diffusion, G is the electron-phonon coupling term and $S(z,t)$ is the depth-dependent laser heating source term. As constructed, this is a one dimensional model, where both the electron and phonon temperatures are depth dependent, $T_e(z)$ and $T_p(z)$. For heating pulses focused to spot sizes of 100s of microns, this model is valid for thin films on the order of 100s of nanometers.

Temperature-Dependent Reflectivity within the Drude Model

The intraband electronic transitions of metals is described with the Drude model,[8] which accounts for the conduction-electron contributions to the complex dielectric constant. Free-electron models, without electron scattering, lead to perfect reflection of metals for frequencies below the plasma frequency – a non-physical result. The Drude model assumes an electron-collision frequency ω_τ, which makes the dielectric function,

$$\epsilon = 1 - \frac{\omega_p^2}{\omega(\omega + i\omega_\tau)}. \tag{4.3}$$

In the above expression, ω_p is the plasma frequency of the metal and ω is the electric field frequency. This introduction of electron collisions results in absorptive behavior. The dielectric function can be further used to calculate the complex

refractive index,[9]

$$\tilde{n} = \sqrt{\epsilon} = n + ik, \tag{4.4}$$

where n is the traditional material refractive index and k is the absorptive component of the index. The imaginary component k is dependent on the collision frequency. From a physical perspective, an applied electric field will drive the Drude or conduction electrons in an oscillatory manner and un-distrubed electrons will re-radiate at the driving frequency. Electrons that undergo collisions, one the other hand, suffer energy loss and cannot re-radiate and a component of the field is observed to have been absorbed by the metal surface.

The collision frequency ω_τ is temperature dependent.[10,11] Thus, the electron-phonon thermalization process can be monitored by following the time resolved reflectance in a pump-probe scheme. In general, the electron collision frequency can be expanded in terms of both the electron and the phonon temperatures. For the temperatures relevant here, the expansion can be simplified to only include two temperature-dependent terms.[10]

$$\omega_\tau \approx A_{ee} T_e^2 + B_{ep} T_p \tag{4.5}$$

A_{ee} and B_{ep} are the electron-electron and electron-phonon scattering coefficients, respectively. These values can be determined for different conductors from experimental thermal and electrical resistivities.[11,12]

4.2 Results

This section describes thermoreflectance results of flash-heated substrates. For these measurements two femtosecond white-light continuum (WL) pulses were incident on the gold surface. One of these WL pulses was overlapped with the flash-heating pulse and served as the signal, reporting temperature-dependent reflectivity changes. The other WL pulse, acting as a reference, was reflected off of a portion of the unheated sample and monitored inherent changes in the WL source.

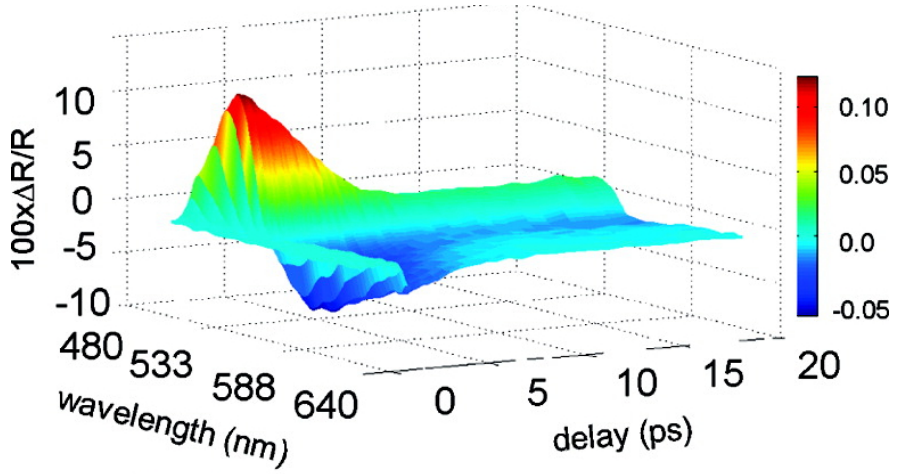

Figure 4.1: Transient thermoreflectance - Time-dependence of Au reflectivity encompassing both the interband-transition and the intraband-transition regions after flash-heating to ∼600 °C for a 0.8-nm Cr / 50-nm Au substrate. The Au phonons have obtained thermal equilibrium in ∼4 ps.

Figure 4.1 is a 2D thermoreflectance plot characteristic of large temperature jumps of Au substrates. As the 100-fs flash-heating pulse excites the surface electrons, the reflectance changes quite abruptly by as much as 8%. Following the two-temperature model, electron-phonon scattering begins to thermalize the electron and lattice temperatures. This thermalization process is observed in the

first few picoseconds as the surface reflectance approaches its long-time values.

The spectral region of the probed reflectivity encompasses both the 510-nm interband transition and other regions where the Drude or conduction electrons dominate the reflectance.[13] The complex shape of the TRTR data near the interband transition indicates that during the flash-heating process the *d*-band electrons are indeed being excited to conduction band. The increase in surface reflectivity can be explained as the following: as more *d*-band electrons are thermally excited to the conduction band, fewer electrons are present to undergo light induced transitions, which in turn boosts the surface reflectivity. Away from the interband transition, the reflectance decreases with temperature, as discussed in §4.1. The in-between region is affected by both the interband and intraband transitions.

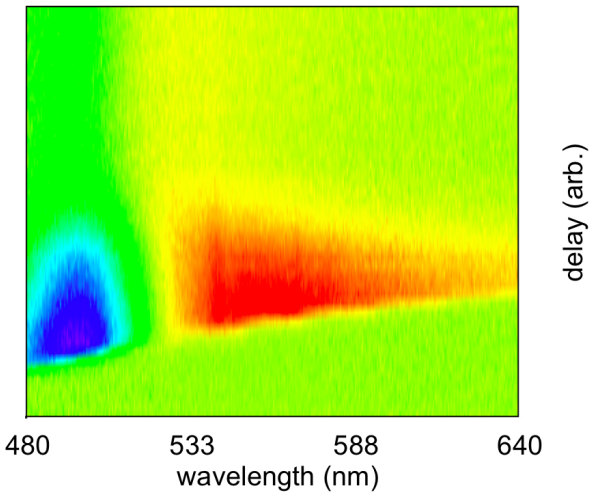

Figure 4.2: Alternate view of transient thermoreflectance - The TRTR data shown here is identical to that of Figure 4.1. The only difference is that the delay axis has a non-linear scale and the actual delays have not been plotted. The positive chirp of the femtosecond white-light continuum is apparent.

There are two interesting features of the data in Figure 4.2; the apparent delay in reflectance dynamics across the various wavelengths, and the spectral changes around the interband transition. The first of these features is a result of chirp present in the white-light continuum pulses. The other feature is indicative of either different thermalization dynamics of the *d*-band and Drude electrons, or different reflectivity temperature dependences in the interband and intraband spectral regions.

Temperature-Dependent Thermalization

These measurements were conducted with 0.8-nm Cr 50-nm Au substrates, where the 0.8-nm Cr layer is a minimal-thickness adhesion layer, in an attempt to study primarily the Au dynamics. The molecular conductance experiments discussed in Chapter 5 and Chapter 6 used 0.8-nm Cr / 50-nm Au substrates.

To study how the pump fluence affected the electron-phonon thermalization rates, 1D frequency slices of the 2D data series as fitted as a function of pump-probe delay for various fluences. The transient reflection dynamics near the interband transition decayed in a non-exponential manner. The dynamics in the Drude region, on the other hand, did fit well to an exponential. While the transient time profiles are slightly different in shape, the thermalization time reported by both spectral regions are approximately equal. Accordingly, the reported thermalization times have been measured using the intraband transition near 600 nm.

The equilibrium constants – the characteristic exponential time constant – for the thermalization process are obtained from a least-squares fitting the TRTR. The errors shown in Figure 4.3 are plus or minus one standard deviation. From

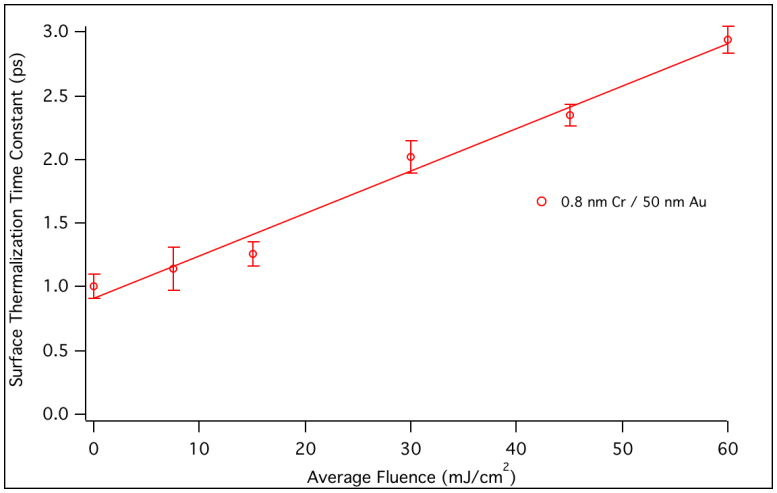

Figure 4.3: Electron-phonon thermalization time - As the pump fluence increases, the characteristic time constant, measured at 600 nm, for electron-phonon thermalization increase for a 0.8-nm Cr / 50-nm Au substrate. The data is plotted verses the average pump fluence, the WL probe beam is focused to a much smaller probes an area that has experiences a local fluence of about twice the average value.

the data, the thermalization time of the Au substrate appears to increases linearly with pump fluence. The low-fluence datum was obtained from the TRTR apparatus described briefly in §5.2. All other data was obtained with the dual-beam femtosecond white-light spectrometer described in §3.4. The abscissa is labeled as average fluence, however, the probe beam is more-tightly focused than the pump; the local area probed experienced a fluence closer to the peak fluence $f_p \approx 2\langle f \rangle$, assuming a near-Gaussian spatial pulse profile.

Varying the Substrate Composition

To better understand how the Cr thickness affected the substrate thermalization and final temperatures, additional experiments were conducted with increasing thicknesses of Cr, while keeping a constant 50-nm-layer of Au. As the Cr layer thickness increased, more laser energy was absorbed by the Cr layer, resulting in

less laser energy available to directly heat the gold. One the short time scales, < 20 ps, for an equivalent fluence, the change in surface reflectance for thicker Cr layers was characterized by a shorter thermalization times. However, as observed at longer delays in Figure 4.4, the temperature of the metal surface continued to increase for substrates with thicker Cr layers.

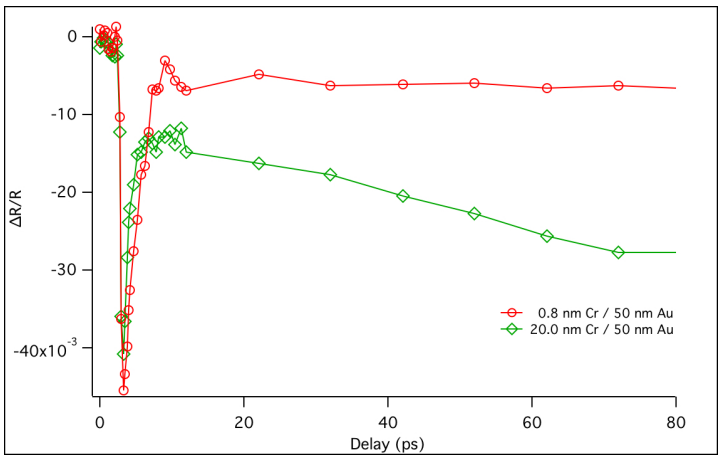

Figure 4.4: Substrate Comparison - The TRTR data for both the 0.8 nm Cr / 50 nm Au and the 20 nm Cr / 50 nm Au substrates are shown for an average pump fluence of 30 mJ/cm^2. The frequency slices are taken at 600 nm to avoid complication by the interband transition dynamics. Differences in the transient surface reflectance are clearly evident. There appears to be a delay after time zero before the surface reflectance changes, this is an artifact due to the chirp in the white-light continuum and should be ignored.

Figure 4.5 compares the relative reflectance change, measured at delay of 20 ps, for several different substrates made with various thicknesses of Cr. For each fluence, the substrates with thicker Cr layers had a larger change in reflectivity at the gold-air interface. This is suggests that for a constant fluence, larger temperature jumps occur for the substrates with thicker Cr layers on the less-than-20-ps time scale. Notice that data for the 20-nm and 10-nm thickness Cr substrates at higher fluences in absent in Figure 4.5. At those fluences, the

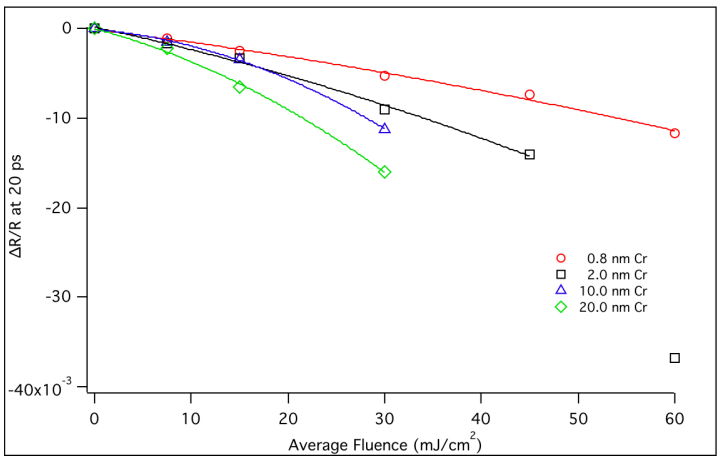

Figure 4.5: Substrate responses at 20 ps - Plotted here are the thermoreflectance measurements for different substrates with varying thicknesses of Cr for several pump fluences. All measurements were taken from time slices at 600 nm and at a pump-probe delay of 20 ps. The quadratic curves through each data set are to guide the eye.

substrate becomes visibly damaged after several hundred laser shots.

Figure 4.6 shows the longer-time reflectance changes of these substrates measured at 150 ps. Both data sets in Figure 4.5 and 4.6 are plotted on the same scale for easy comparison. The substrate with the thinest Cr layer reached a constant temperature within 2-6 ps, depending on the pump fluence, and the reflectance change is constant between delays of 5 and 150 ps. The surface reflectance for all other substrates continues to change out to 150 ps after the heating event. For example, the 20-nm Cr / 50-nm Au sample exhibits a reflectance loss of ∼2% at a 20-ps delay and a further loss to ∼3% by a 150-ps delay.

4.3 Discussion

As seen from the TRTR data shown in Figure 4.1, both the interband and the intraband regions are sensitive to changes in the electronic temperature. For small

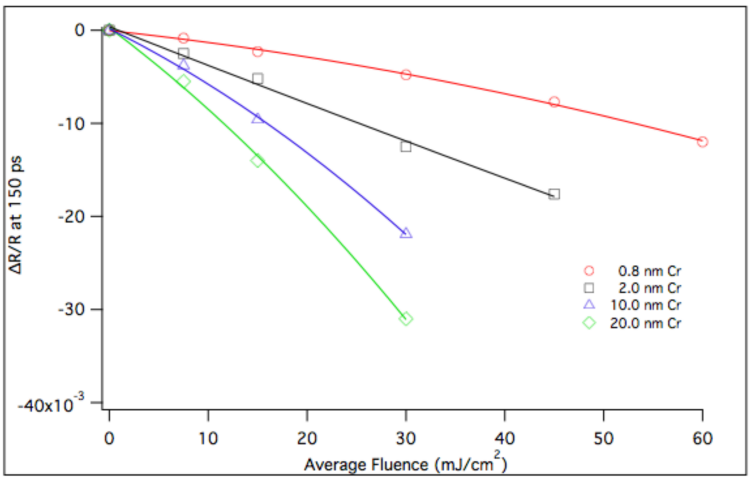

Figure 4.6: Substrate responses at 150 ps - The data plotted here is identical to that of Figure 4.5, except the relative reflectance changes are measured at a pump-probe delay of 150 ps. The quadratic curves through each data set are to guide the eye.

temperature jumps, only Drude electrons are promoted into higher-energy states. As mentioned before, the electron collision frequency is temperature dependent and the reflectance is subsequently altered. At the temperature jumps discussed here, the *d*-band electrons are also thermally excited to the conduction band. As a result, there are both fewer electrons are present in the *d*-band to undergo the interband transition, and fewer available or unoccupied final states that can accept a transitioning electron. The result is a decrease in absorption, which necessarily leads to an increase in reflectivity observed at early times. The long-time relative increase in reflectivity is caused by changes in the electron-band energies due to lattice expansion.

The Au thickness for all samples studied discussed here was 50 nm – several times the skin depth for this material.[14] Due to the thickness of the Au, the equilibration dynamics of the Cr sub-layer are not expected to influence the observed thermoreflectance data. The dynamics reported are affected by the temperature

dynamics of the Au surface.

Electron-Phonon Thermalization at High Temperatures

For the 0.8-nm Cr / 50-nm Au substrates, the Cr acts essentially as an adhesion layer, binding the Au to the SiO_2. The Cr layer does not absorb a significant amount of laser energy, and can be neglected for this discussion. The observed surface reflection dynamics are then a result of the electron-phonon thermalization process within the Au film.

The time required for surface thermalization τ scales linearly with pump fluence, as seen in Figure 4.3. The electron-phonon coupling factor G is predicted to increase with increasing electron temperature[15], which suggest that the thermalization process would become more rapid at higher fluences. This is, however, not the case; the data clearly show that the thermalization time τ increases. After inspection of Equation 4.1, the thermalization time is affected by both the electron-phonon coupling strength G and the electronic heat capacity C_e. In the limited of $T_e >> T_p$,

$$\tau = C_e(T)/G(T). \tag{4.6}$$

At ambient temperatures C_e is linear with T, but as the T becomes large, the d-band electrons begin to contribute to the electronic heat capacity.[15] The outcome is that both C_e and G have dependences on T, such that the thermalization time of the reflectance is observed to increase linearly with pump fluence.

Effects of Cr Thickness

By increasing the Cr thickness, more energy is absorbed in the Cr layer and the amount of laser energy available to directly heat the Au layer is reduced. For the substrates with 20-nm-thick Cr only about one third of the laser energy arrives at the Au layer compared to the substrates with only 0.8 nm of Cr. As a result, the electron temperature within the Au layer is substantially less than that of the substrates with thinner Cr layers. And accordingly, the substrates with lower Au-electron temperatures undergo faster thermalization within the Au layer. This effect is evident in the early time dynamics of the TRTR traces plotted in Figure 4.4; the initial fast drop in surface reflectance recovers faster in the 20-nm Cr / 50-nm Au sample when compared to the 0.8-nm Cr / 50-nm Au sample.

Similar to the dynamic processes that occur in Au, femtosecond laser heating of Cr leads to a non-equilibrium scenario of hot electrons and cold phonons. The electron-phonon coupling in Cr is quite strong and thermalization occurs on the sub-picosecond time scale; this strong coupling is characteristic of transition metals with an unfilled *d*-shell.[15] While the electrons and phonons in Cr are completely thermalized in <1 ps, the gold electrons and phonons are thermalizing over several picoseconds. As a result, the Au phonons in the thicker-Cr substrates are pumped both by the Au electrons and by the Cr phonons. The rate of phonon-phonon pumping is much slower than the electron-phonon pumping and is dictated by the interfacial conductance of the two materials.[16] The effects of phonon-phonon heating are observed in Figure 4.4 and by comparing Figures 4.5 and 4.6. The surface reflectance continues to decrease in the Drude region even out to ∼150 ps as the surface temperature continues to increase.

Temperature Estimate of 0.8-nm Cr / 50-nm Au Substrates

Experimental laser-based melting studies of 200-nm-thick Au layers found a melting fluence of 450 mJ cm^{-2}.[17] Assuming that most of the absorbed energy is deposited into the Au layer within in a distance of several skin depths – which is reasonable – then both the 200-nm-thick and the 50-nm-thick Au samples would absorb similar amounts of laser energy. The thermal mass of a 50-nm-thick Au layer is one fourth of that of the 200-nm-thick Au layer. Thus, one may expected that the melting fluence for the 0.8-nm Cr / 50-nm Au substrates should be ∼112 mJ cm^{-2}. The local peak fluence for the highest pump power in Figure 4.3 is ∼120 mJ cm^{-2}. At higher fluences, the data was not reproducible which suggest that local melting had occurred.

Looking at the model of Jiang and Tsai,[3] which agrees well with high-fluence melting experiments, the electron-phonon thermalization constant for a temperature jump of ∼500 K is approximately 5 ps. At early delays when the electron temperature is large, $A_{ee}T_e^2$ dominates the temperature-dependent reflectance. Accordingly, the thermoreflectance trace should have a time constant of ∼2.7 ps in the Drude region. The observed value is slightly less, measured at 2±.1 ps. This suggests that either the electron-phonon parameter within the model is not exactly correct, or that the temperature jumps are slightly less than expected. The agreement with previous experimental melting studies leads one to believe that the experimental work is correct.

4.4 Summary

The surface thermalization times for Cr-Au composite substrates were measured at various pump fluences. Both interband and intraband dynamics were visible. For the 0.8-nm Cr / 50-nm Au substrates, where the Au surface reflectivity is dictated by the electron-phonon dynamics in the Au layer, the thermalization time constant τ was found to increase linearly with applied pump laser fluence. For substrates with thicker Cr layers, the surface reflectivity at early time delays was dominated by direct laser pumping and the electron-phonon thermalization within the Au layer. At longer time delays, the surface reflectance continued to change, resulting from the flow of thermal energy from the Cr layer into the Au layer through phonon-phonon coupling.

The 0.8-nm Cr / 50-nm Au substrates reach thermal equilibrium, defined by $\sim 2\tau$, within 2 to 6 ps depending on the pumping fluence. While the other substrates, having larger Cr thicknesses, took $\sim$ 100 ps before the substrates was in thermal equilibrium. To study how molecular adsorbates behave under large thermal gradients, the substrate or heat bath should have the fastest thermalization time possible. Thus for the molecular conductance measurements discuss in the following chapters are conducted with the 0.8-nm Cr / 50-nm Au substrates. The laser powers used for those studies correspond to spot-averaged fluences ranging between 30-45 mJ cm^{-2}.

4.5 References

1. Anisimov, S. I.; Kapeliovich, B. L.; Perel'man, T. L., Sov. Phsy. JETP, 39, 375, 1974.
2. Fatti, N. D.; Voisin, C.; Achermann, M.; Tzortzakis, S.; Christofilos, D., Phys. Rev. B, 61, 16956, 2000.
3. Jiang, L.; Tsai, H.-L., J. Heat Transfer, 127, 10, 2005.
4. Sun, C.-K.; Vallee, F.; Acioli, L.; Ippen, E. P.; Fukimoto, J. G., Phys. Rev. B, 48, 16, 1993.
5. Brorson, S. D.; Fujimoto, J. G.; Ippen, E. P., Phys. Rev. Lett., 59, 1962, 1987.
6. Hu, M.; Petrova, H.; Hartland, G. V. Chem. Phys. Lett. 391, 220, 2004.
7. Chan, W.-L.; Averback, R. S.; Cahill, D. G.; Ashkenazy, Y. Phys. Rev. Lett., 102, 095701, 2009.
8. Ashcroft, N. W.; Mermin, N. D., Solid State Physics. Holt, Rinehart, and Winston, New York, 1976.
9. Griffiths, D. J. Introduction to Electrodynamics, 3^{rd} Ed. Prentice hall, Upper Saddle River, New Jersey, 1999.
10. Smith, A. N.; Norris, P. M., Appl. Phys. Lett., 78, 9, 2001.
11. Kittel, C., Introduction to Solid State Physics, 7^{th} Ed. Wiley, New York, 1996.
12. MacDonald, A. H., Phys. Rev. Lett., 44, 489, 1980.
13. Scouler, W. J.; Lin, W. Z.; Fujimoto, J. G., Phys. Rev. Lett. 18, 445, 1967.
14. Palik, E. D., Handbook of Optical Constants. Academic Press, Boston 1985.
15. Lin, Z.; Zhigilei J. V.; Celli, V., Phys. Rev. B. 77, 075133, 2008.
16. Kading, O. W.; Skurk, H.; Goodson, K. E., Appl. Phys. Lett., 65, 1629, 1994.
17. Stuart, B. C.; Feit, M. D.; Herman, S.; Rubenchik, A. M.; Shore, B. W.; Perry, M. D., J. Opt. Soc. Am. B, 13, 459, 1996.

5

Energy Transfer Across Gold-Alkanethiolate Monolayer Interfaces[1]

5.1 Introduction

Heat transfer is an important design component, extending across nearly all scientific and engineering fields. In most applications, heat is transfer or conducted through macroscopic objects. At the level of individual molecules, however, the familiar concepts of heat diffusion by phonons in bulk materials no longer apply. At the molecular level, discrete molecular vibrations transfer thermal energy. An emerging area where vibrational energy transfer becomes crucial is the field of molecular electronics, where long-chain molecules attached to tiny electrodes are

[1]The research presented here has been previously published as: Wang, Z.; Carter, J. A.; Lagutchev, A.; Koh, Y. K.; Seong, N.-H.; Cahill, D. G.; Dlott. D. D. Science, 317, 787, 2007.

used to transport and switch electrons. When an electron is transported through a molecule, inelastic collisions may occur between the electron and the molecular wire. This results in a transfer of energy from the electron into the molecular vibrations.[1] In studies such as this one where molecular energy levels are not individually resolved, it is conventional to call such processes "heat dissipation" or "nanoscale thermal transport" [2], even through an equilibrium Boltzmann distribution is not necessarily achieved. Nitzan and co-workers[3] have estimated that 10-50% of the electron energies could be converted to heat. Accordingly, a power of 10^{11} eV/s may be dissipated on a molecular electronic bridge carrying 10 nA under a bias of 1 eV. Using classical and quantum mechanical methods, they and others[1] have calculated steady-state temperatures resulting from such dissipation. But steady-state calculations do not entirely capture the essence of this phenomenon. The energy lost when electrons are transported through a molecular wire in a fraction of a picosecond appears as staccato bursts, up to 1 eV per burst. On a ten-carbon alkane molecule, for instance, 1eV is enough energy to produce a transient temperature jump $\Delta T \approx 225K$. At the temperatures associated with these ultrafast energy bursts, Nitzan and co-workers[3] suggest that, instead of the usual phonon mechanisms prevalent in ordinary thermal conduction processes[1], much of the heat is carried by high energy molecular vibrations such as carbon-carbon bending and stretching and carbon-hydrogen bending, which are delocalized over a few carbon segments.[3]

To study molecular energy transport in the regime of short distances, short time intervals and large temperature bursts, we have used an ultrafast flash thermal conductance apparatus to study densely packed self-assembled monolayers of long-chain hydrocarbon molecules anchored to metal substrates. Laser flash-

heating jumped the temperature of the metal substrate several hundreds of degrees in $\sim$ 1 ps. Heat flowed from the metal layer into the base of the molecular chains and then through the chains. Vibrationally-resonant sum-frequency spectroscopy was used that selectively probed the thermally-induced disorder of the methyl groups at the ends of the chains.

The concept of the thermal conductance apparatus is illustrated if Fig. 5.1. A femtosecond laser pulse flash-heated an $\sim$300-μm-diameter region of an Au layer crafted for a fast time response of $\sim$1 ps. The SAMs are formed from n-alkanethiol molecules HS-$(CH_2)_n$-CH_3 with an even number of carbon atoms from C6 to C24. A nonlinear coherent spectroscopic method,[4] termed broadband multiplex vibrational sum-frequency generation spectroscopy (SFG) probed an enseble of $\sim 10^{11}$ alkane chains at the cneter of the heated region. We determined an overall rate for heat transport from Au into the alkane chains, and a time for heat to propagate from the base to the ends of the chains, as a function of the length h of the alkane molecules.

An 800-nm, 500-fs-duration laser pulse from an amplified titanium-doped-saphhire laser[5] incident on the Au/glass interface (the back side) of the 50-nm-thick Au layer generated hot electrons within a skin depth of $\sim$15 nm.[6] Because the hot electrons have a large diffusion coefficient, the electron temperatures at the front and the back of the Au layer equalized even before the electron-phonon coupling brought the hot electrons into equilibrium with the lattice (6). Within $\sim$1 ps, the Au layer was in thermal equilibrium and uniformly heated throughout.[6] To improve the adhesion of Au to glass it was necessary to add a Cr layer beneath the Au. Unfortunately, heat transfer from a Cr layer to Au is relatively slow; to minimize this effect, we made the Cr layer just 0.7 - 0.8 nm thick.

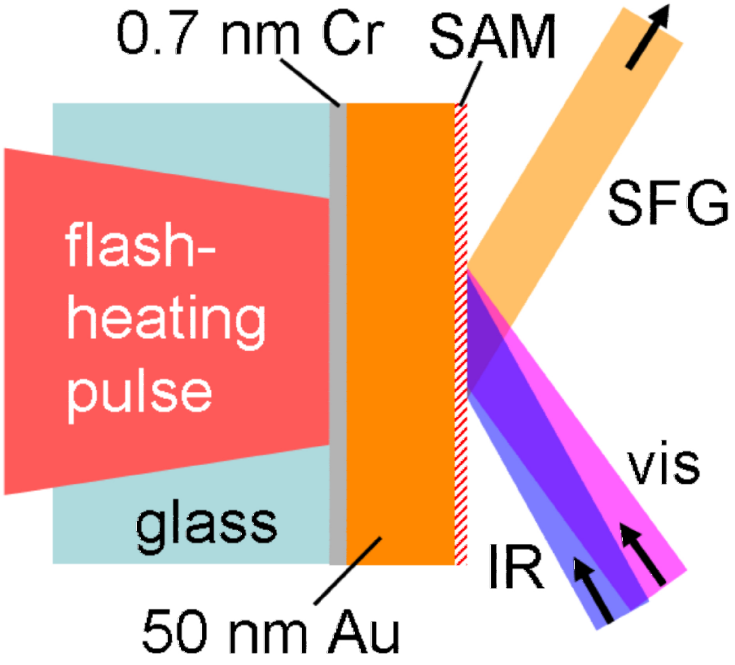

Figure 5.1: Concept of the ultrafast flash thermal conductance measurements - IR and visible pulses combine to generate SFG in an ~200-μm-diameter region containing $\sim 10^{11}$ alkane chains. SFG is sensitive to thermal disordering of the alkane terminal methyl groups of SAMs, which occurs when heat propagates from the Au surface to the ends of the alkane chains.

In the SFG technique we used, a femtosecond infrared (IR) pulse at 3.3 μm with a bandwidth of 150 cm^{-1} is incident on the SAM, coherently exciting all the alknae CH-stretch transitions in the 2850 to 3000 cm^{-1} range, along with electrons in the Au skin layer, producing an oscillating polarization in both the Au and the SAM layers. At the same time, a picosecond-duration 800-nm pulse ("visible") with a bandwidth of 7 cm^{-1} is incident on the sample. The visible pulse interacts with this oscillating polarization through coherent Raman scattering to create a coherent output pulse at the IR+Visible frequency. This combined IR-Raman interaction is forbidden within the dipole approximation for centrosymmetric media because the second-order susceptibility $\chi^{(2)}$ vanishes in such media. Because the methylene -CH_2- groups of the alkane SAM form a nearly centrosymmetric solid, the SFG signal that we observed originated predominatly from the Au surface and the terminal methyl -CH_3 groups. the well-known SFG spectrum obtain in *ppp* polarization,[4] from a SAM with n=17 (e.i., an 18-carbon or C18 SAM), is shown in Fig. 5.5. Molecular vibrational transitions appear as dips against a broad non-resonant background from Au. These methyl transitions have a spectral width $\Delta\nu$ = 15 cm^{-1}, corresponding to a coherence decay time constant T_2 = 0.7 ps, which indicates that SFG signals are emitted during an ∼1 ps time window. Thus the time resolution of these SFG measurements is ∼1 ps.

5.2 Results

Flash-Heating of Au-Cr Layers

This section described initial results characterizing the flash-heating response of the ultrafast heat bath using temperature excursions of a few degrees per laser

pulse. Latter experiments that better characterized the ultrafast heat baths were conducted with larger temperature jumps and discussed in-depth in Chapter 4.

The time scale for femtosecond laser heating of the glass-Cr-Au samples was characterized by time-domain thermoreflectance (TDTR). The output of a femtosecond Ti:sapphire laser oscillator operating at a repetition rate of 80 MHz was split into 10 mW pump and probe beams. The pump beam was incident on the metal layers from the glass side as in the SFG measurements. The pump beam was modulated at 9.8 MHz and focused with a 20 mm focal length objective lens to a 1/e2 spot diameter of 6 μm. The probe beam was directed down a variable optical delay and then focused onto the metal layer to 6 μm diameter with a separate 20 mm focal length objective. The probe beam was recollimated and directed into a Si photodiode detector. The signal, representing small changes in the Au surface reflectance induced by pump-pulse heating, was acquired using an rf lock-in amplifier at the 9.8 MHz modulation frequency. An imaging optical system and CCD camera facilitated the alignment of the pump and probe beams; final alignment was performed by maximizing the thermoreflectance signal.

These TDTR measurements characterized heating and cooling rates for small temperature excursions. The laser power incident at the sample was $\sim$10 mW for both the pump and probe beams. The steady-state temperature rise resulting from the average laser power and radial heat flow in the glass substrate was 10 K; the temperature jump of the Au film created by each optical pulse of the pump beam was $<$1 K. In order to craft a metal layer with the highest flash-heating rate, several samples were measured with varying Cr thickness, Cr deposition conditions, Au thickness, and the presence or absence of the SAM. The time scale of heating the Au film was independent of Au thickness at the 50 nm value used

here, but the time scale of heating increased approximately linearly with the Cr thickness, reaching 30 ps when the Cr layer was 5 nm thick. This led us to choose a Cr layer of minimal thickness, 0.8 nm. The SAM did not noticeably influence the TDTR results since the heat capacity of the SAM is much smaller than the Au film, and the SAM is too thin to significantly alter the time-dependent optical reflectivity of the Au surface. The thermal conductance of metal-metal interfaces increases linearly with increasing temperature,[3] so the rate of heat flow from Cr to Au which limits the rate of flash heating in the SFG experiments is expected to be even faster than what was observed.

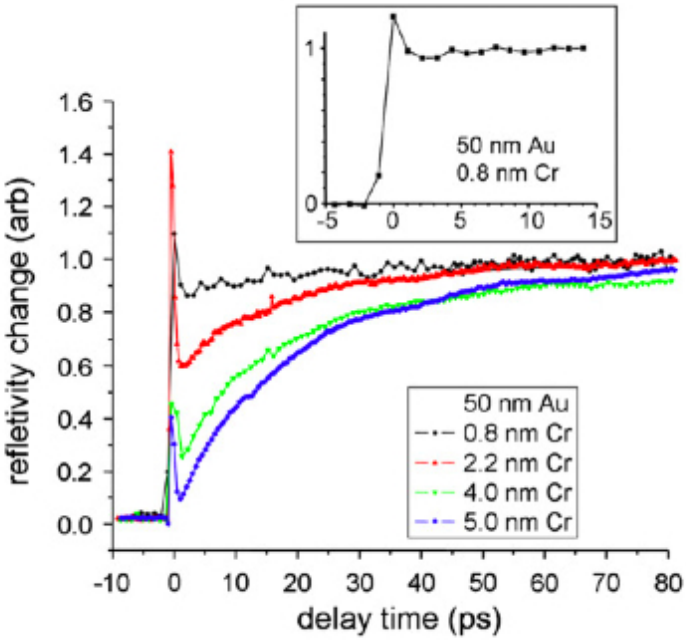

Figure 5.2: Thermoreflectivity - Thermoreflectance measurements of flash-heating of Cr-Au thick films on glass with 50-nm-think Au, as a function of Cr layer thickness. Heating cause the normalized reflectivity change to increase toward unity. The sharper feature near $t = 0$ is due to hot electrons. The fastest response was obtained with the 0.8-nm-thick Cr layer, as shown in the inset. The Au-surface temperature jumps to 90% of its peak within 1 ps, with the remainder of the rise occurring in <5 ps.

Using the 0.8-nm-thick Cr layer, the Au surface reached a temperature of 80% of the final temperature within 1 ps. There is also a slower (1.5 ps time constant) rise to the final temperature believed to be due to the Cr Layer. The same transient response was observed with either front-side or back-side flash-heating and with or without a SAM. The Au layer remained at an approximately constant high temperature for several nanoseconds, subsequently cooling by heat diffusion into the glass. In the SFG experiments, the intensity of the heating pulse was varied to locate the threshold for melting the Au, and then the pulse was attenuated by 20%. Because the melting temperature of Au $T_m = 1064°C$, this procedure resulted in flash-heating of the Au layer to $\sim 800°C$.

Molecular Dynamics Simulations

In order to better understand how ultrafast heating affects SFG signals, variable-temperature molecular-dynamics simulations were preformed on a C16 SAM on Au using the *Cerius*^{2} software package. These simulations are similar to those of Hautman and Klein,[7–9] but with time and temperature parameters relevant to these experiments.[10,11] The monolayer model had 27 C16 molecules on a $\sqrt{3} \times \sqrt{3}$ $R30°$ lattice atop a 50-nm-thick Au(111) substrate. The surface cell was a rhombus measuring 2.996×2.996 nm^2 with an angle of 199.94°. Periodic boundary conditions were used. The potentials were calculated using the *COMPASS* force field. Bonding interactions were restricted to harmonic terms, as in Ref 3. The nonbonding interactions were truncated at 20 Åand smoothed with a spline function. When the SAM was equilibrated at 300 K, the well-known[4] all-*trans* structure with a chain tilt of ∼35° and a zenith angle of ∼25° was obtained. The zenith is the angle between the surface normal and the final C-C bond, in this

case the C_{15}-C_{16} bond.

Ideally these simulations would be used to calculate the ensemble-averaged hyperpolarizabilities to generate the second-order material susceptibility $\chi^{(2)}$ These calculations are quite difficult, so a simpler approach was was taken. In the dipole approximation, the molecular hyperpolarizability is proportional to the IR transition dipole moment multiplied by the Raman polarizability. Instead of a preforming the ensemble average on the hyperpolarizability, which is a rank-three tensor, the IR transition moment was ensemble averaged. This simplification, while less rigorous, does provide the correct time-scale for the monolayer response to the ultrafast heat bath.

Considering the specific case of the $\nu_s CH_3$ transition, having an transition dipole moment of magnitude μ_{01} parallel to the terminal C_{15}-C_{16} bond, the square of the normalized ensemble-averaged μ_{01} is

$$\langle \mu_{01} \rangle^2 / |\mu_{01}|^2 = \left[\left(\frac{1}{n} \sum_{i=1}^{n} \vec{\mu}_{01} \right) \right]^2 / |\mu_{01}|^2. \tag{5.1}$$

This average is straightforward to calculate from a molecular dynamics simulation, by simply calculating the ensemble-averaged length of a unit vector parallel to the C_{15}-C_{16} bond.

Two difference types of simulations were conducted. The first determined an equilibrium temperature-dependence of the ensemble average, and the second characterized the evolution of the monolayer disorder after an instantaneous temperature jump. Starting with an energy-minimized structure at 0 K, the temperature was increase in increments of roughly constant $\beta = 1/k_B T$. For the thermalization at each temperature, the molecular dynamics trajectories were run

for up to 20 ps. The time needed to for the SAM to equilibrate varied between simulations and was judged by monitoring the amount of energy partitioned into torsional motions; the torsional component was the slowest to equilibrate of the various energy contributions. The ensemble average was then determined at ten different times – selected from using a random-number generator – during the last 5-10 ps when the SAM appeared to be in equilibrium. This process was used to generate the temperature-dependence of the monolayer disorder.

For the temperature-jump dynamics, the monolayer started with the ambient-temperature structure – a defect-free all-*trans* structure. The temperature of the SAM was then instantaneously jumped to $\sim$ 800 °C. The system was allowed to time-evolve and the ensemble average was computed at several subsequent times.

As the temperature was increased in the simulation, the methyl groups became orientationally disorder, decreasing the magnitude of $\langle\mu_{01}\rangle^2$. The disorder seems to saturate at a temperature of $\sim$ 600 K. Figure 5.4B shows how the thermal disordering progresses after a simulated fast temperature increase to 1100 K. On the <1-ps time scale, the labile terminal methyl groups undergo orientational fluctuations. On the $\sim$2-ps time scale, multiple gauche defects are created below the surface.[10,11]

Monolayer Response

Three intense vibrational transitions were observed, originating from the symmetric $\nu_s CH_3$ and the antisymmetric $\nu_a CH_3$ methyl stretching vibrations and from the δCH_3 bending overtone transition, which draws intensity from a 2:1 Fermi resonance with the CH stretches.[4,12] All methylene transitions are weak, which is indicative of a high degree of order.[4] Figure 5.6A shows the spectrum of a C18

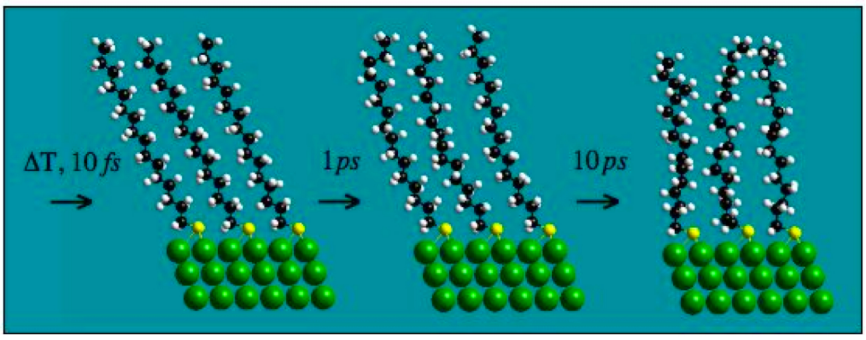

Figure 5.3: Evolution of monolayer disorder - Representative snap shots of the non-equilibrium molecular dynamics at various delays after the monolayer temperature was instantaneously jumped to 800 °C. The increase in monolayer disorder is evident as the monolayer explores further in the newly accessible regions of phase space.

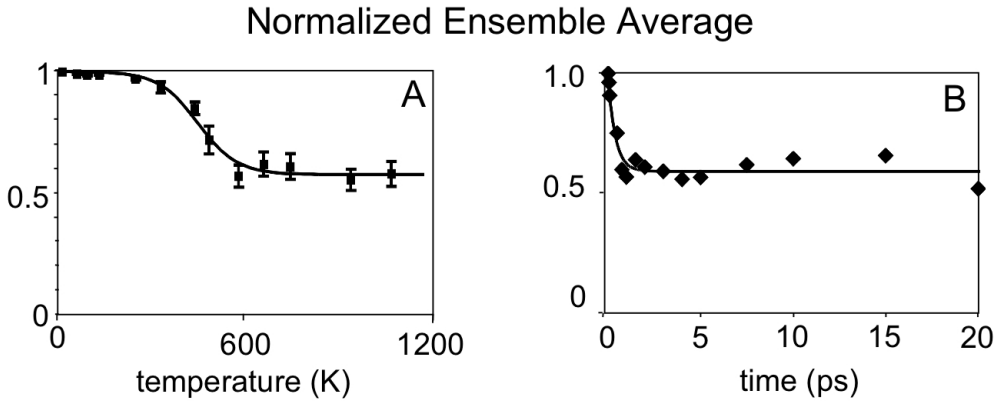

Figure 5.4: Results from molecular simulations - The magnitude and time scale of the sum-frequency intensity loss for the $\nu_s CH_3$ transition approximately follows the square of the normalized ensemble-average IR dipolar moment. (A) The magnitude is strongly temperature dependent between 300 K and 600 K. (B) With an instantaneous temperature jump to 1100 K, the mehtyl head groups become orientationally disordered in ∼1 ps.

SAM ∼400 ps after flash-heating, where the SAM is in equilibrium with Au at ∼800°C. All three methyl transitions appear to have lost intensity as a result of thermal disordering of the methyl groups. The $2\delta CH_3$ band evidences a red shift and broadens. It is notable that the methylene transitions remain weak at high temperature and that the transient intensity loss of the methyl transitions are reversible once the SAM returns to ambient temperature.

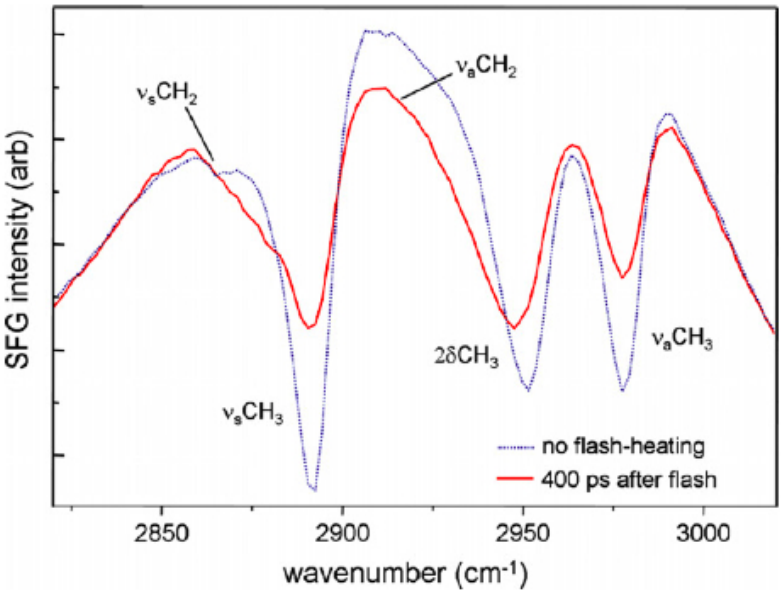

Figure 5.5: C18 SAM - SFG spectrum of a C18 SAM on Au, 400 ps after flash-heating to 1100K(solid), when Au and SAM are in thermal equilibrium, compared to a reference spectrum without flash-heating (dotted). Flash-heating causes SFG intensity loss in the CH_3 and $2\delta CH_3$ transitions. A thermal redshift of the $2\delta CH_3$ transition is also observed. No significant enhancement of the CH_2 transitions is observed.

Figure 5.6 shows a time series of SFG spectra after flash-heating of the Au to ∼800°C for C8 and C18 chains. SFG intensity loss is clearly faster with the shorter chains. The intensity-loss time dependence appears to be similar for all three methyl vibrational transitions, so the remaining discussion will consider

only $\nu_s CH_3$. To quantify the intensity loss, we define a normalized vibrational response function (VRF),[5,10]

$$VRF(t) = [I(T_{cold}) - I(t)]\ [I(T_{cold}) - I(t_{hot})], \tag{5.2}$$

where $I(T_{cold})$ is the $\nu_s CH_3$ vibrational intensity at ambient temperature and $I(T_{hot})$ is the intensity after a few hundred picoseonds when the Au and SAM are in thermal equilibrium.

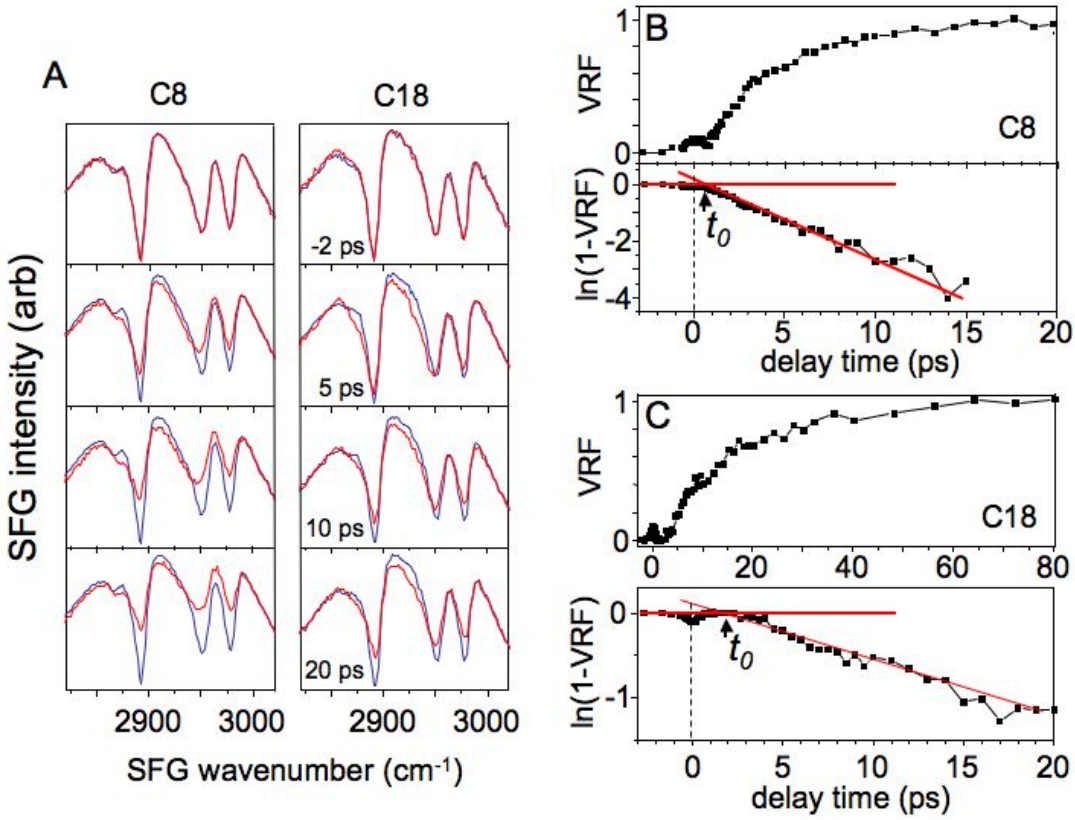

Figure 5.6: Representative time-dependent SFG spectra - (A) SFG spectra of C8 and C18 SAMs without heating pusles (blue) and with flash-heating pulses (red). The vibrational resonances of the methyl groups appear as narrow dips on a positive non-resonant background. (B) VRF for C8 monolayer. (C) VRF for a C18 monolayer.

The *VRFs* for C8 and C18 chains are shown in Fig. 5.6, B and C, where $t = 0$ denotes the arrival of the flash-heating pulses. Near $t = 0$, there is an artifact caused by pump-induced changes of the Fresnel coefficients of the metal surface, leading to a temporary loss of SFG intensity. This artifact is a fiducial time marker that locates $t = 0$. More precisely, the artifact occurs when the pump pulse and the visible pulse arrive at the sample simultaneously. For all alkane chains, the *VRFs* increased exponentially toward unity with a time constant τ. The increase of the *VRF*, however, did not start at $t = 0$. There was a time delay t_0 before this buildup. As a result of the delayed buildup, we fit the data to the function:

$$VRF(t) = \begin{cases} 0 & ;\ t < t_0 \\ 1 - e^{-(t-t_0)/\tau} & ;\ t \geq t_0 \end{cases} \tag{5.3}$$

To extract the parameters t_0 and τ from the data, we plotted $ln(1 - VRF)$ versus t as in Fig. 4.2, B and C, and used linear least-squares fitting in the $t > t_0$ region. The slope gave τ, and the abscissa intercept gave t_0. In Fig. 5.7, A and B, we plot t_0 and τ versus chain length. The chain length h, based on conventional molecular bonding parameters,[13] obeys the relation $h(nm) = 0.127n + 0.4$. Both t_0 and τ increased linearly with chain length.

5.3 Discussion

Monolayer Stability

The observation that the heating effects are reversible once the SAMs return to ambient temperatures is significant. This indicates that the chains remained bonded to the Au surfaces and do not irreversibly generate disulfide dimers.

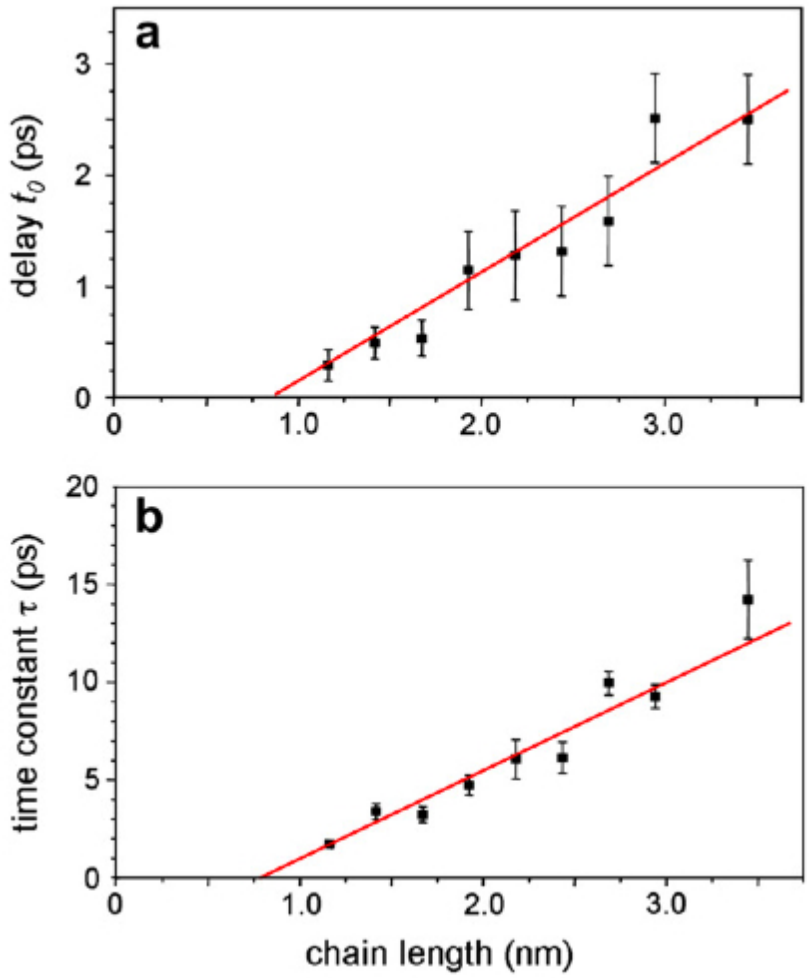

Figure 5.7: Chain-Length Dependent - (A) Dependence on chain length of the delay time t_0 between the flash-heating pulse and the arrival of the initial burst of heat at the methyl heat groups. (B) Dependence of chain length of the time constant τ for thermal equilibration between flash-heated Au and alkane chains.

The unexpected stability of these SAMs at temperatures far above the usual 175-225°C desorption range[14,15] must be attributed to the brief duration of the temperature jump. Thermal stability in the presence of ultrafast temperature jumps can be addressed in the language of transition-state theory, where $k(T) = (kT/h)e^{\Delta S^{\dagger}/RT}e^{-\Delta H^{\dagger}/RT}$. The normal desorption process of the disulfide dimer formation is a bimolecular reaction. An alternative, not usually seen at hight surface coverage, is the unimolecular dissociation and evaporation of single chains. With a sudden jump to a high temperature, where $\Delta H^{\dagger}/RT \ll 1$, the rate becomes limited solely by the pre-exponential factor. The bimolecular reaction channel has a lower barrier and a smaller pre-exponential factor, perhaps 10^6 s^{-1}, because the entropy change for forming the dimer is large and negative. Thus, there is not enough time at hight temperature for dimerization and then subsequent evaporation to occur. The unimolecular channel has a higher barrier and a much larger pre-exponential perhaps $> 10^{11}$ s^{-1}. The lack of observation of monolayer loss indicates that the unimolecular barrier is too high to be competitive even at these elevated temperatures.

Molecular Thermometers

The molecular dynamics simulations suggestive of a gradual transition between an ordered crystalline state and a fluid-like state as the monolayer temperature is increases. Hauptman and Klein refer to the elevated-temperaure state was the "rotator" phase.[9] Above ∼600 K, the monolayer disorder saturates, becoming insensitive to further temperature increases. Thus, based on the sum-frequency signals of the alkanethiolate monolayers, these systems can be employeed as molecular thermometers in the temperature range of 300-600 K. These thermometers are

approximately 1.5-Åthick, the width of a single CH_3 group. The time response of these molecular thermometers is ∼1 ps as observed from the simulations. In other words, any observed monolayer response slower than 1 ps is indicative of actual energy flow into the monolayer.

Ballastic Thermal Transport

The delay time t_0 emerges from the ability of SFG to selectively probe alkanes at the terminal methyl groups. The heat burst from the Au substrate travels along the chains, but only after the leading edge of this heat burst reaches the terminal methyl groups does the SFG optical thermometer begin to register an effect. Thus, t_0 is interpreted as the time for heat to travel from the Au surface to the ends of the alkane chains. The linear dependence of t_0 on chain length indicates that the leading edge of the heat burst propagates ballistically along the chains, and the slope of the data in Fig. 5.7A gives a velocity of 0.95 (±0.1) nm/ps = 0.95 km/s.

The quantum mechanical models of Nizan and co-workers[1,3] show that 700 °C heat transport along alkane chains attached to a pair of metal electrodes involves molecular vibrations ranging up to 1500 cm^{-1}. The ballistic velocity of 1 km.s for heat transport along alkane chains should be understood as resulting not from acoustic phonons, which in polyethylene – a similar material – at ∼2.3 km s^{-1}, but instead from a mix of intramolecular vibrations dephasing at a slower rate.

Non-Zero Intercept and Physical Meaning

In Fig. 5.7, both t_0 and τ go to zero at a finite chain length of ∼0.8 nm. This indicates that the hot Au layer does not transfer its heat into an individual atom

at the base of the SAM, but instead Au transfers energy into a region at the base of the SAM 0.8 in length, which is about four carbon segments. This result is in good agreement with the predictions of Segal *et al.*,[3] which find that the heat-carrying vibrations of short-chain alkanes are delocalized over four to five carbon segments.

While this explanation fits quite nicely the theoretical predictions,[3] there is the possibility of an alternative explanation. In later experiments – discussed in Chapter 6 – with benzylthiolate monolayers, an abrupt loss of sum-frequency signals in ∼1 ps was observed, followed by a subsequent partial recover of signal over several tens of picoseconds. After various experiments we believe that it is possible for non-equilbrium electrons – hot electrons that have yet to thermalize with the phonons – to directly heat the adsorbed molecules through inelastic scattering. If this effect was appreciable for alkanethiolate monolayers, then the non-zero intercept would need to be re-interpted as the effective scattering distance. The effective scattering distance is defined here as the distance into the monolayer that hot electrons can scatter from and deposit substantial amount of vibrational energy into the molecules.

Estimation of Interfacial Conductance

The linear dependence of τ on chain length h is indicative of a heat transfer process dominated by interfacial conductance.[2,16] In this limit, heat transfer from Au to the alkane chains is the rate-limited step, controlled by the strength of the coupling between the Au phonons and the alkane vibrations. The interface

thermal conductance G can be defined as,

$$G = q/\Delta T, \tag{5.4}$$

where q is the heat flux normal to the interface and ΔT is the interfacial temperature drop. If we use a time-averaged heat flux of $\rho C_p h \Delta T/\tau$ – the total amount of thermal energy needed to raise the monolayer temperature to that of the heat bath spread over the observed thermalization time. In the previous equation, ρ is the monolayer density, C_p is the specific heat of the monolayer and h is the monolayer length. Substituting $\rho \mathrm{C_p h} \Delta T/\tau$ for q in the above equation, we arrive at an expression for the interfacial conductance in terms of experimental parameters,

$$G = \rho C_p h/\tau, \tag{5.5}$$

The interfacial conductance G is an interfacial property and is affected by both of the adjoined materials. According to Nitzan[3] the molecular vibrations responsible for heat transfer are delocalized to only a few carbon segments. Thus the coupling between the bath modes and the monolayer vibrations is likely independent of chain-length for alkanethiolates greater than 4 or 5 carbons. Hence, we take the interfacial conductance to be constant for all monolayers in this chapter. Obviously, the interfacial conductance is in general molecule dependent, and if the molecular structure is significantly altered in some way, then we would expect G to change accordingly.

At first glance, the interfacial conductance appears to be dependent on chain length. The is, however, not the case. Longer chains need more total energy to reach the same temperature, so longer chains heat up more slowly. Thus the

quotient h/τ is independent of chain length. Alternatively, we can rewrite the above equation,

$$\tau = \rho C_p / Gh, \tag{5.6}$$

and compare $\rho C_p/G$ to the slope of the data in Fig 5.7 B, allowing the interfacial conductance G to be determined.

Estimating the value of the interfacial thermal conductance G from the time constant τ requires a knowledge of the alkane SAM specific heat C_p in the temperature range 25-300 °C. Since these specific heats are not known, these values will be estimated. Looking toward other hydrocarbons for reasonable estimates, such as liquid alkanes or polyethylenes, is natural starting point. These materials vary in density, and the best estimates are likely obtained by trying to match the density of the SAM layers. Using the C18 chains as an example, the area per chain is 21.7 Å^2, the perpendicular height of the SAM is 23.6 Å, and the molar mass of C18 is 285.56 g/mol (13). The mass per unit area is $m_A = 2.2 \times 10^{-6}$ kg m^{-2} and the density is $\rho = 930$ kg m^{-3}.

Beattie *et al.*[17] have suggested liquid hexadecane as a model for SAMs, but the density of hexadecane ($\rho = 770$ Kg m^{-3}) is quite low. Some lower-density polyethylenes and crystalline paraffin wax, with a density[18] $\rho = 930$ kg m^{-3}, seem to be a better match to the SAMs. Above 110 °C, the specific heats (J Kg^{-1} K^{-1}) of low-density polyethylenes and paraffin are similar and can be represented by the relation,[18]

$$C_p(T) = [2550 + 3.37(T - 110°C)]. \tag{5.7}$$

This relation, however, was verified to be accurate only to temperatures up

to ∼150 °C.[18] In what follows, the linear dependence of C_p on T is assumed to be extendable to the needed hight temperatures of these experiments. There is an experimental precedent for this extrapolation; optical thermometry studies of nanosecond flash-heated polymers found that on time scales too fast for significant thermal decomposition to occur, the data were consistent with a linear extrapolation of the specific heat to 550 °C. Accordingly, a temperature-averaged specific heat $\bar{C}_p$ can be defined as,

$$\bar{C}_p = \frac{\int_{T_i}^{T_f} C_p(T)}{T_f = T_i}. \tag{5.8}$$

Using tabulated specific-heat data in the 25-110 °C range[8]) and the linear extrapolation at higher temperatures, $\bar{C}_p = 3000$ J kg^{-1} K^{-1} in the 25-300 °C range. Regardless of the material chosen – whether other low-density polyethylenes or paraffin – $\bar{C}_p$ did not vary by more than ∼10%. Thus, the errors of the $\bar{C}_p$ estimation and the errors in other parameters such as ΔT or G that depend of $\bar{C}_p$ are less influenced by the bulk material used to model the alkane SAMs, and more strongly dependent on the high-temperature C_p extrapolation.

The time constant τ is observed to increase linearly SAM height h, concluding that G is independent of alkane chain length. The best linear fit to the data in Figure 5.7B gives a slope τ/h of 4.5 ps nm^{-1}. Due to the saturation of the monolayer disorder at temperatures about 300 °C, τ represents the time constant describing the heat-up to ∼300 °C. The time constant associated with heating to 800 °C, when the monolayer is in thermal equilibrium with the Au substrate, would be several times longer. Using a linear approximation, $\tau \times (800-25)/(300-25) \approx 2.8\tau$, yielding a corrected slope in Figure 5.7B of 12.6 ps nm^{-1}. Adopting

values of $\bar{C}_p$ = 3000 J kg^{-1} K^{-1} and ρ = 930 kg m^{-3}, the estimation of the interfacial conductance G is 200($\pm$30) MW m^{-2} K^{-1}. The error associated with G is estimated from the standard deviation of the least-squares fitting in Figure 5.7B. This takes no account of the error introduced from the estimation of C_p or the monolayer-saturation correction. A realistic estimation of the error in this calculation should be much higher.

For comparsion, the values calculated by Nitzan[1,3] for molecular thermal conductances at 700 °C where found to be approximately chain-length independent for $n \leq 7$ and slightly less than 100 pW K^{-1}. Using the above value of G and an area per alkane chain of 2.2 10^{-19} m^2,[11] a single-molecule thermal conductance of 50 pW K^{-1} = 0.3 eV ns^{-1} K^{-1} is obtained. Thus, this measurements are in good agreement with quantum mechanical calculations that precede this work.

5.4 Summary

The sum-frequency signal is dependent on monolayer disorder and therefore provides a novel probe technique to monitor the energy flow into and through materials with molecular dimensions. This probe technique can be seen to confer two important advantages. In the past, thermal conductance measurements of SAMs were based on measuring heat flow across two interfaces;[19–21] the ability to probe the SAM itself eliminates one interface. Even though the flow of energy into the SAM is determined largely by interface effects, the ability to selectively probe the atomic groups that terminate the chains, rather than the thermal expansion of the entire chain,[22] allows us to investigate energy transport through the chain molecules themselves.

For the alkanethiolate monolayers studied here, the time delay t_0 representing the time necessary for the thermal energy to arrive at the CH_3 group was found to follow a linear relationship with monolayer chain length h. This suggests that the thermal energy travels ballistically through these one-molecule-thick films, apposed to a diffusive behavior where scattering events would lead to a non-linear relationship between t_0 and h. The inverse slope obtained from the linear yielded a heat flow velocity of 1 nm ps^{-1}. Additionally, the time-resolved sum-frequency signals decayed with a characteristic exponential time constant, which also exhibited a linear relationship with monolayer chain length. The τ parameter is related to the thermalization dynamics of the initially room-temperature monolayer with the laser flash-heated metallic substrate. The linear behavior is indicative of an process limited by a constant interfacial conductance, and from that an estimation of the monolayer-susbtrate interfacial conductance of $\sim$220 MW m^{-2} K^{-1} was made. Interestingly both plots of t_0 and τ versus h had a non-zero intercept that extrapolated to 0.8 nm. This length corresponds to a molecular section of S-$(CH_2)_4$, which is interpreted as a delocalized region of the molecular to which energy is directly deposited.

5.5 References

1. M. Galperin, M. A. Ratner, A. Nitzan, J. Phys.: Condens. Matter 19, 103201 (2007).
2. D. G. Cahill et al., J. Appl. Phys. 93, 793 (2003).
3. D. Segal, A. Nitzan, P. Hnggi, J. Chem. Phys. 119, 6840 (2003).
4. L. J. Richter, T. P. Petralli-Mallow, J. P. Stephenson, Opt. Lett. 23, 1594 (1998).
5. A. S. Lagutchev, J. E. Patterson, W. Huang, D. D. Dlott, J. Phys. Chem. B 109, 5033 (2005).
6. S. D. Brorson, J. G. Fujimoto, E. P. Ippen, Phys. Rev. Lett. 59, 1962 (1987).
7. J. Hautman, J.P. Bareman, W. Mar, M.L. Klein, J. Chem. Soc., Faraday Trans. 87 (1991) 2031.
8. J. Hautman, M.L. Klein, J. Chem. Phys. 91 (1989) 4994.
9. J. Hautman, M.L. Klein, J. Chem. Phys. 93 (1990) 7483.
10. J.E. Patterson, A.S. Lagutchev, W. Huang, D.D. Dlott, Phys. Rev. Lett. 94 015501(2005).
11. J.E. Patterson, D.D. Dlott, J. Phys. Chem. B 109 5045 (2005).
12. C. D. Bain, P. B. Davies, T. H. Ong, R. N. Ward, Langmuir 7, 1563 (1991).
13. C. D. Bain et al., J. Am. Chem. Soc. 111, 321 (1989).
14. N. Nishida, M. Hara, H. Sasabe, K. Wolfgang, Jpn. J. Appl. Phys.: I35 (1996) 5866.
15. H. Kondoh, C. Kodama, H. Sumida, H. Nozoye, J. Chem. Phys. 111,(1999) 1175.
16. H. K. Lyeo, D. G. Cahilll, Phys. Rev. B. 73, 144301 (2006).
17. D.A. Beattie, S. Haydock, C.D. Bain, Vibr. Spectrosc. 24 109 (2000).

18. M. Dole, W. P. Hettinger Jr., N. R. Larson, J. A. Wethington Jr., J. Chem. Phys. 20, 781 (1952).

19. Z. B. Ge, D. G. Cahill, P. V. Braun, J. Phys. Chem. B. 108, 18870 (2004).

20. Z. B. Ge, D. G. Chaill, P. V. Braun, Phys. Rev. Lett. 89, 173113 (2006).

21. R. Y. Wang, R. A. Segalman, A. Majumdar, Appl. Phys. Lett. 89, 173113 (2006).

22. S. Chen, M. T. Seidel, A. H. Zewail, Angew, Chem. Int. Ed. 45, 5154 (2006).

6

Energy Transfer Across Gold-Benyzlthiolate Monolayer Interfaces[1]

6.1 Introduction

This chapter describes measurements of energy transfer from polycrystalline Au(111) surfaces flash-heated by femtosecond laser pulses to estimated temperatures of 600 C, to self-assembled monolayers (SAMs) of aryl- and alkyl-thiol adsorbates. In the previous chapter, this technique to study heat flow along even-numbered alkanethiolate SAMs from C6 to C24, ranging in length from 1.2 to 3.5 nm. The vibrational sum-frequency spectroscopy of CH-stretch transitions of the alkane

[1]The research presented here has been previously published as: Wang, Z.; Cahill, D. G.; Carter, J. A.; Koh, Y. K.; Lagutchev, A.; Seong, N.-H.; Dlott, D. D., Chem. Phys., 350, 2008. Carter, J. A.; Wang, Z.; Dlott, D. D., J. Phys. Chem. A, 112, 2008. Carter, J. A.; Wang, Z.; Fujiwara, H.; Dlott, D. D., J. Phys. Chem. A, 113, 2009.

terminal methyl groups could be used as a molecular thermometer to measure heat flow from the Au surface, along the alkane chains, to the terminal methyl groups. The thermometer had a thickness comparable to the 1.5 diameter of the terminal methyl groups and a response time of <1 ps.

Alkanes shorter than C6 were unfortunately not stable enough for those measurements, which involved many thousands of high-intensity laser pulses. Thus, energy transfer from the metal surface to moieties that were separated from the surface by fewer than six carbon atoms were unable to be probed. There was, however, a very interesting observation about the short-chain-length behavior. The time response of the SFG thermometer from all alkane chains in the C6-C24 range had the same characteristic shape, characterized by two parameters t_0 and τ. See §5.2.2 for an in-depth discussion. The t_0 parameter was the delay time before the thermometer first began to respond, and τ was the time constant characterizing the exponential rise to the final temperature. Both t_0 and τ were observed to increase linearly with chain length. t_0 was interpreted as the time for the initial heat burst to propagate along the alkane chains, from the Au surface to the terminal methyl groups. The linear length dependence indicated that the heat burst propagated ballistically, and the results yielded a velocity of 1 km/s. The linear length dependence of τ indicated that the rate of chain heating was directly proportional to the chain heat capacity, which increases linearly with chain length. This type of dependence occurs when heat flow is dominated by a thermal barrier at the Au-SAM interface.[1,4] In such cases, heat flow across the interface is the same for all chains, but longer chains need more heat to attain the final temperature.

When plotted as a function of chain length, both t_0 and τ display non-zero

intercepts of 0.8 nm, which corresponds to a chain with 4-5 carbon atoms. Of course this intercept is an extrapolated quantity, but if taken literally, this suggests that chains 4-5 carbon atoms or less in length are heated instantaneously by the Au surface. This result is consistent with theory from Nitzans group,[5–7] who found that the heat-carrying vibrations of short-chain alkanes are delocalized over 4-5 carbon segments. It was concluded that phonons of the Au surface couple to and transmit energy to a *base region* of the alkane chains 4-5 carbon atoms in length.[1,2]

This interesting observation is the motivation for the present study, which examines a variety of molecules that probe energy transfer processes at close distances from a flash-heated Au surface. This chapter presents flash-heating data on SAMs comprised of the molecules shown in Figure 6.1. There are three classes of SAMs, short alkanes, methyl-, nitro-, and phenyl-substituted benzenes, and benzene-linker molecules of the form (C_6H_5)-$(CH_2)_n$-SH (n = 0-5) denoted BT, B1T, B2T, and so forth.

6.2 Results

SFG Spectra

Due to the high symmetries or atomic arrangements of the molecular adsorbates, in most cases, the SFG spectra arise from a single CH_3, CH, or NO_2 group.[3] These groups are highlighted in Figure 6.1. Representative SFG spectra using the non-resonant suppression technique[8] are shown in Figure 6.2 and Figure 6.3, after flash-heating to ∼600 °C. In Figure 6.2, the C6 spectra, originating from the terminal methyl groups, consist of three peaks, representing the symmetric

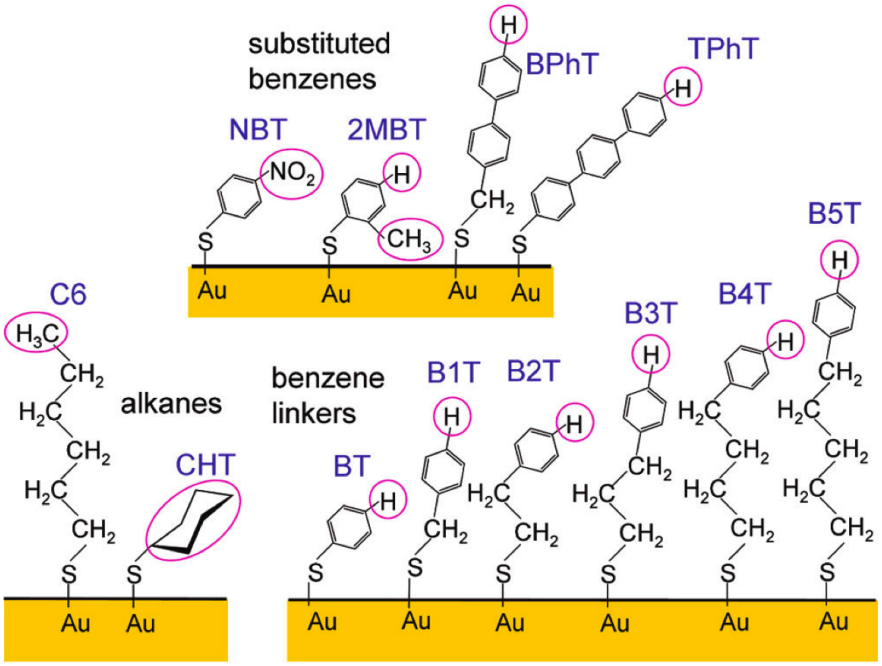

Figure 6.1: Molecular structures - Structures and acronyms of individual molecules comprising the thiolate SAMs used in this study. The atomic moieties most-likely responsible for the sum-frequency signals are indicated by circles.

and antisymmetric methyl CH stretches and the Fermi resonance.[9] Upon flash-heating, all peaks appear to lose intensity, but only the Fermi resonance exhibits a noticeable, yet still small, frequency redshift.[2] The methylene transitions were not observed.

The CH-stretches transitions of the BT, B1T, B2T, B3T, B4T and B5T SAMs result from the CH groups para to the thiolate linkage. In the local-mode picture, the SFG hyperpolarizabilities of the CH groups at the 2 and 5 positions tend to cancel each other, as do the CH groups at the 3 and 6 positions. Furthermore, a CH_3 substituent at the para positions eliminates the aromatic CH-stretch signal.[3] After flash-heating, the BT, B1T and B2T CH-stretch transitions lose intensity and evidence a slight redshift.

In the case of 2MBT, both methyl and phenyl CH-stretch transitions are simultaneously observable.[10] The methyl signal is easily assigned to the methyl-group substituent. The phenyl CH-stretch signal, however, is a bit more difficult to assign definitively, due to the lowered symmetry of the orthro-substituted phenyl ring. Again, resorting to a local-mode picture, the sum-frequency signal likely originates from a combination of CH-stretches from the CH groups at the 4- and 5-positions. Shown in Figure 6.3, both methyl and phenyl transitions lose intensity upon flash-heating, but the methyl transitions do not redshift.

NBT, also shown in Figure 6.3, is the only SAM studied where a transition other than a CH stretch was probed. Both symmetric and asymmetric NO_2 stretching transitions were independently observed, although only the spectra for the symmetric NO_2 stretch are shown. Both transitions lose intensity and redshift upon flash-heating.

In cyclohexanethiol (CHT), two intense CH-stretch transitions are detectable.

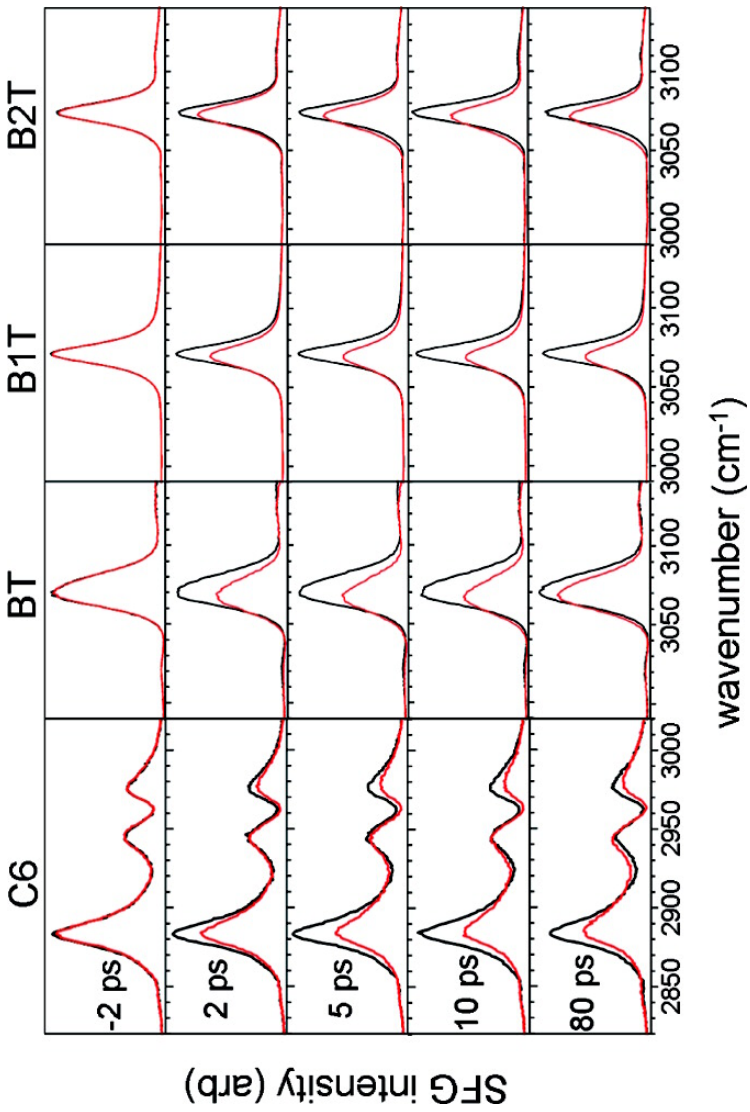

Figure 6.2: SFG spectra - SFG spectra, at the indicated times after flash-heating to ∼600 °C, for the terminal methyl CH stretch of the C6 alkanethiol on Au and the 4-position phenyl CH stretch of three benzenethiol SAMs on Au. The solid black curves are spectra taken with the SFG probe pulses preceding the flash-heating pulses.

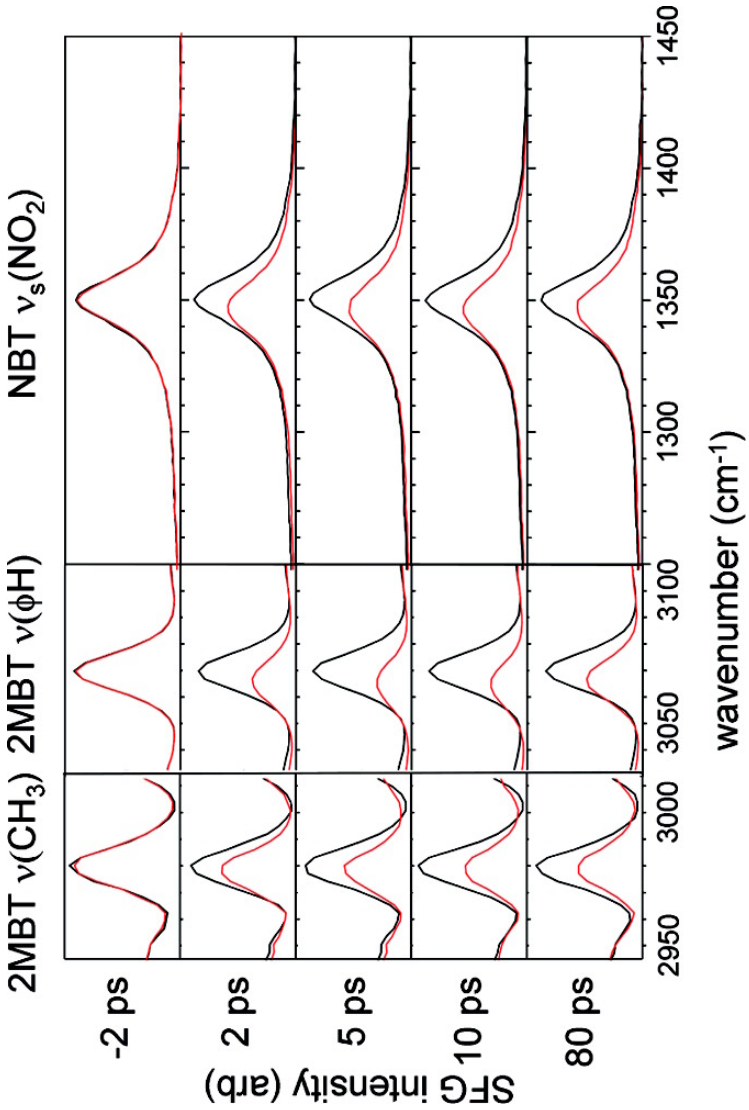

Figure 6.3: SFG spectra - SFG spectra, at the indicated times after flash-heating to ∼600 °C, for the methyl and phenyl CH stretch transitions of 2-methylbenzenethiolate SAM (2MBT) on AU and the symmetric nitro stretch of 4-nitrobensenethiolate (NBT) SAM on Au. The solid black curves are spectra taken with the SFG probe pulses receding the flash-heating pulses.

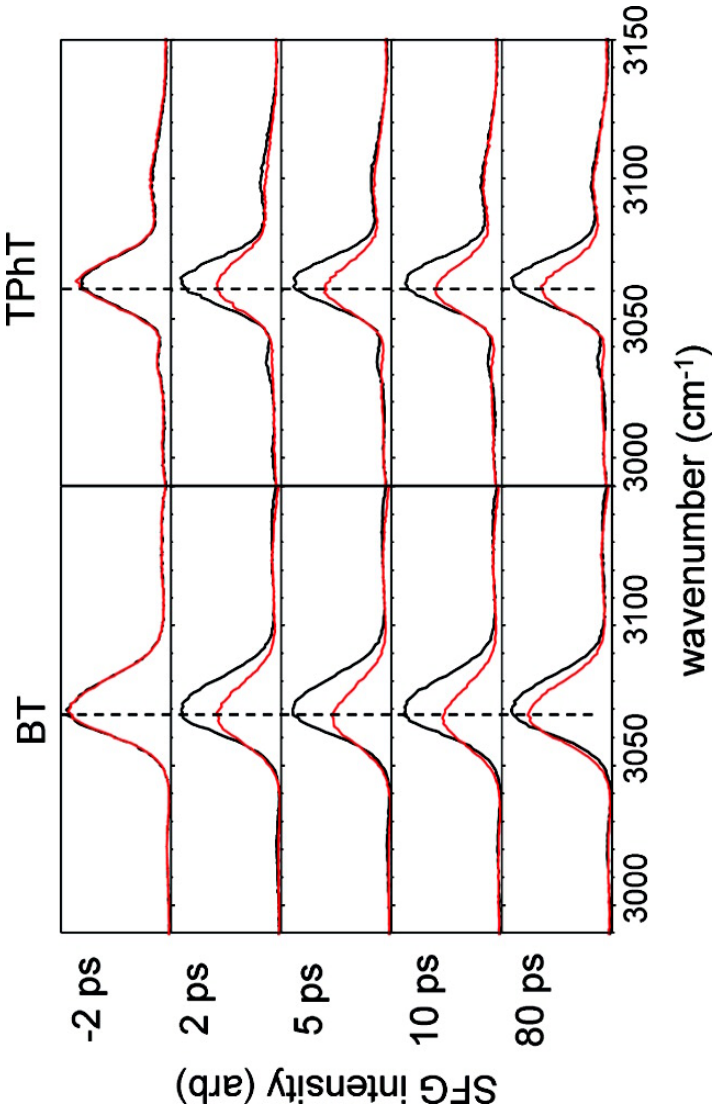

Figure 6.4: SFG spectra - SFG spectra from flash-heated benzenethiol (BT) and terphenylthiol (TPhT) at indicated times after flash-heating. THe solid black curves are spectra taken with the SFG probe pulses preceding the flash-heating pulses. Both SAMs evidence a thermal redshift. The BT SAM shows a redshift overshoot in the 2-10 ps time range, but the TPhT SAM shows no redshift overshoot.

It is reported[11] that CHT at higher surface coverage exists predominantly in the equatorial chair conformer. Accordingly, the observed signals are most probably originating from two inequivalent CH sites, although, currently one cannot rule out the possibility that we are seeing a mixed axial and equatorial chair SAM.

For the biphenyl (BPhT) and the terphenyl (TPhT) SAMs, the SFG signal is believed, based on the BT substitution studies, to arise from the single CH moiety at the 8-position in BPhT and the 12-position in TPhT. Figure 6.4 compares SFG spectra from BT and TPhT. The vertical dashed lines are guides to the eye and help illustrate that, while both BT and TPhT exhibit a redshift, BT has a redshift overshoot in the 2-10 ps range, but no redshift overshoot is observed for TPhT.

SFG Overshoot after Flash-Heating

One dominate feature of the time-dependent data that has yet to be discussed is the observed intensity overshoot, characterized by the rapid loss of signal and its subsequent partial recovery. This phenomenon is easily seen in most of the time-dependence of the integrated spectral intensity shown in Figure 6.5, Figure 6.6 and Figure 6.7.

In the analysis of earlier experiments,[1,2,10] the data was plotted as a vibrational response function for each SAM, normalized to range from 0 to 1. This approach is not as helpful in comparing series of quite different molecular structures, because it conceals information about the magnitude of the SFG intensity drop. In chapter 6, the data are plotted as the fractional signal loss without further normalization.

To quantify the overshoot, the intensity-minimum value is subtracted from the long-time value. Thus, for BT in Figure 6.5, the overshoot is reported as 0.22. The BT overshoot decays with a time constant of 25 ps. In CHT, the

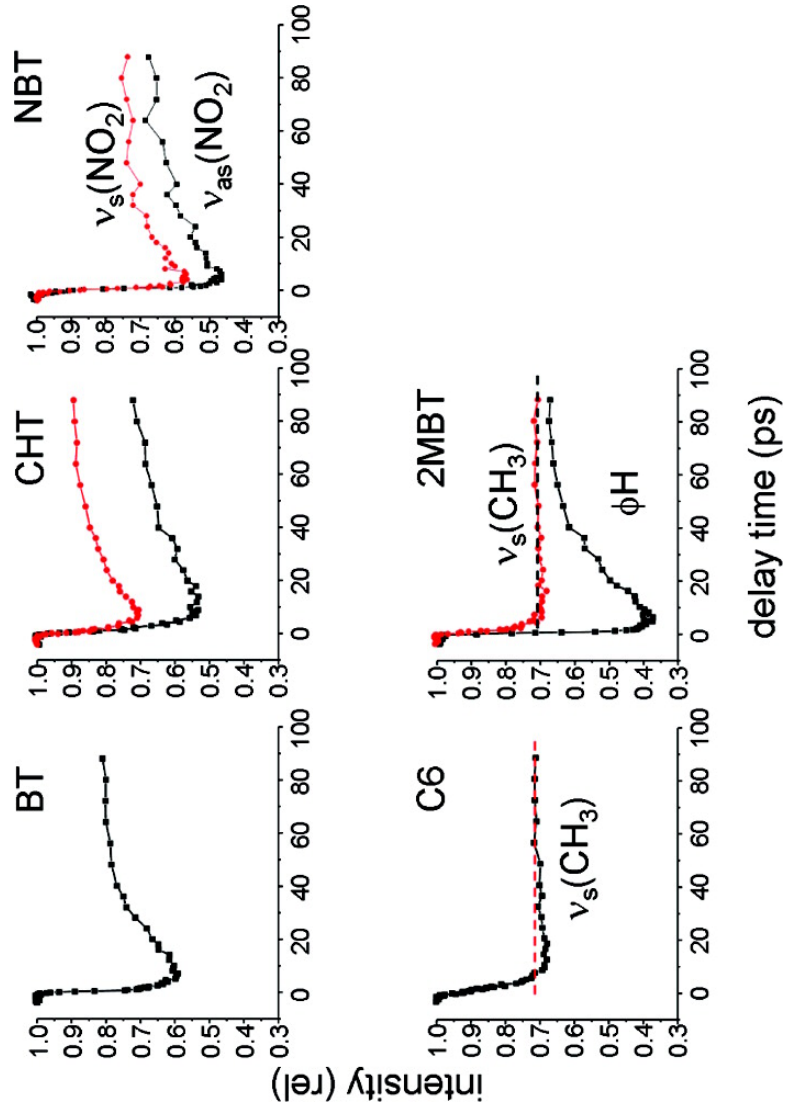

Figure 6.5: Dynamics of various monolayer structures - Time-dependence of SFG intensity loss for CH-stretch transitions of five SAM structures on Au. The dashed lines through the C6 and 2MBT data are guides to the eye to illustrate the small overshoots.

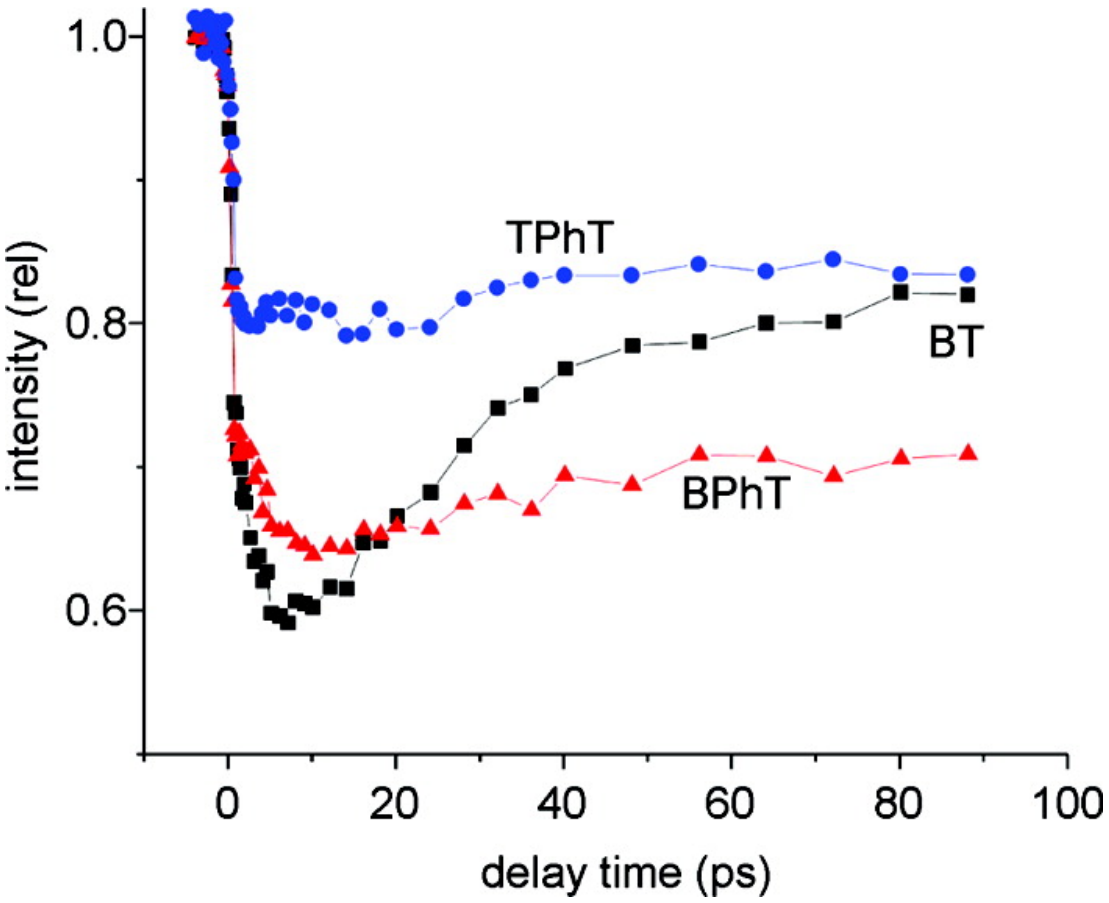

Figure 6.6: Dynamics for aromatic series - SFG intensity loss after flash-heating of benzenethiol (BT), 4-phenyl benzylthiol (BPhT), and terphenyl thiol (TPhT). The large overshoot observed with BT is much smaller in the biphenyl and terphenyl thiols.

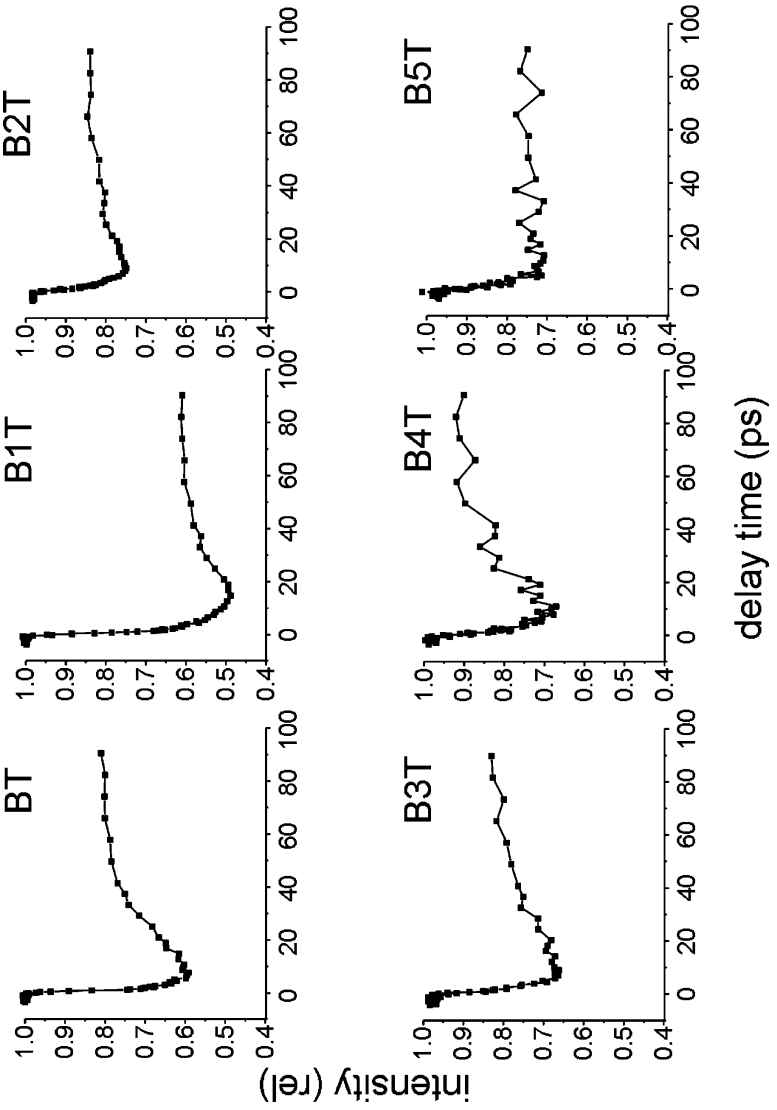

Figure 6.7: Dynamics for the -CH_2- linker series - Time-dependence of SFG intensity loss for phenyl-CH stretch of six SAM structures where a phenyl group is attached to the thiolate by the indicated number of -CH_2 linkers. As the linker becomes longer, the overshoot becomes less prominent.

two CH-stretch transitions, associated with the two inequivalent hydrogen sites, each have an overshoot of 0.20. For NBT, the nitro-group overshoot is 0.20 for $\nu_a(NO_2)$, and possibly a bit less for $\nu_s(NO_2)$. The overshoot for C6 is 0.04 and was not noticed in earlier work[2] due to a poor signal-to-noise ratio. The longer (even-numbered) alkanes C8-C24 show no detectable overshoot. With 2MBT, the phenyl CH stretch shows a large overshoot of 0.28, while methyl CH stretch might have a very small overshoot – no more than 1-2%.

Figure 6.6 compares the dynamics of BT to those of BPhT and TPhT. Note the biphenyl molecule has a methyl linker, which is absent in both BT and TPhT. The intensity overshoots are 0.22, 0.05 and $\leq$0.02 for the BT, BPhT, and TPhT, respectively. Figure 6.7 shows data for phenyl CH-stretch transitions of the benzene-linker molecules. The signal-to-noise ratio is best for BT and B1T, and decreases with increasing linker length. The SAMs with longer linkers seem to form less-dense and less-stable monolayers. Consequently, the sum-frequency signals are smaller and the monolayers degrade over time, limiting the amount of signal averaging. Despite the noise, one can see that the overshoot appears to decrease with increasing linker length (B4T is an exception), and there is no observable overshoot with B5T.

Figure 6.8 looks in more detail at the shorter-time behavior by comparing the normalized Au-surface reflectance change to the normalized SFG intensity drop of BT and B5T. This format allows direct comparisons between the different types of measurements. The fast rise of the reflectance, with a 400 fs risetime (10%-90%), is due to hot electrons generated by the pulse, and this rise should be viewed as the apparatus response time. The time resolution stems from the finite duration of the heating pulse plus a small amount of wobble (tens of micrometers) of the

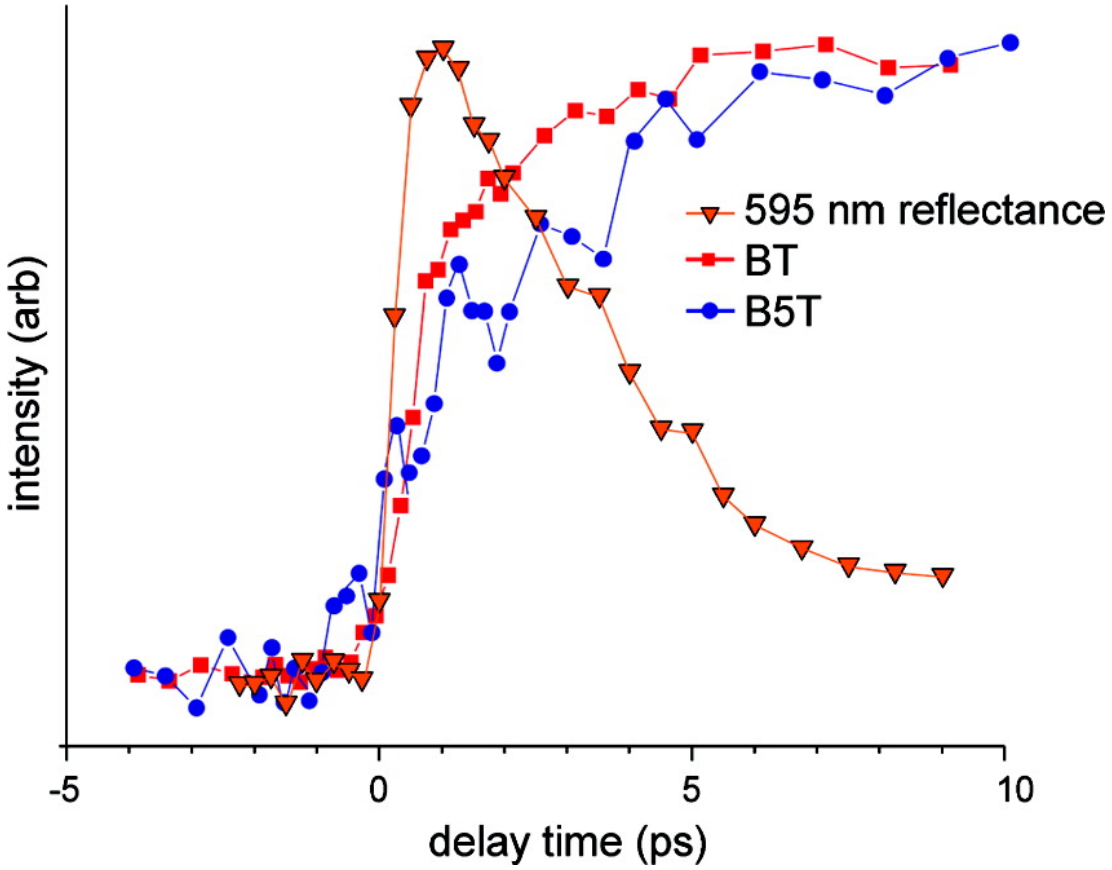

Figure 6.8: Rise-time comparison - Comparison of the early-time dynamics of the thermoreflectivity data and the sum-frequency response from benzenethiol (BT) and benzene-phentylthiol (B5T) monolayers. All data have been normalized.

sample translator. The BT SFG data has what can reasonably be termed a two-part rise, with the first part only marginally slower than the reflectance rise, and the second part characterized by a time constant in the 1.5-2.0 ps range. With the poor signal-to-noise ratio for the B5T data, it is not possible to definitively characterize the functional form of the rise in detail, but the B5T rise is clearly slower than that of BT, most notably in the 1.5-4 ps range.

SFG Thermometer

Prior to flash heating and at long delay times, $t \gtrsim 50$ ps, the SAMs are in thermal equilibrium with the Au surface. The SFG intensities I_{SFG} at these times are representative of the surface temperature. Therefore one can define an SFG thermometer coefficient Θ – the fractional change in I_{SFG} between an initial and final equilibrium temperature,

$$\Theta = \frac{\partial ln I_{SFG}}{\partial T} \tag{6.1}$$

Looking at the data in Figures 6.5-6.7, the SAM with the largest thermometer coefficient is B1T. Considering that B1T SAMs also provide relatively intense SFG signals, one should conclude that B1T is the best SFG thermometer. Another excellent thermometer is BPhT; this is because of both its large thermometer coefficient and its stability with respect to long-term irradiation by laser pulses. Of course, because of the overshoot, B1T is not as useful as an alkanethiol SAM for studying shorter-time heat-flow dynamics.

Figure 6.7 may also suggest the presence of a chain alternation effect for Θ. The SAMs with 1, 3, and 5 carbon atoms in the linker are better thermometers

than the SAMs with 0, 2, and 4 methyl-group linkers.

6.3 Discussion

According to standard thermodynamics, if one object, at an initial temperature of T_1, is placed in thermal contact with another object, having an initially higher temperature T_2, then the two objects will reach a thermodynamic equilibrium at a new final temperature T_f, such that $T_1 < T_f < T_2$. Assuming the two-object system is thermal isolated from the surroundings, trying to imagine a scenario where at any point in the thermalization process were the temperature of the first object temporally exceeds the final equilibrium temperature is difficult. If the SFG monolayer response is purely acting as a molecular thermometer, then this data suggests exactly that sort of temperature-overshoot process. Thus, the SFG signals must be reporting at least one other type of dynamics.

This section discusses a alternative model for the observed intensity overshoot, which involves the excitation of molecular vibrations by excited Au-surface electrons. The excited vibrational population results in a loss of the SFG intensity – an idea presented in §2.2. The accompanying redshift overshoot is attributed to electron excitation of at least some of the lower-energy vibrations, that are anharmonically coupled to the probed vibrations, to occupation numbers that temporarily exceed their ultimate populations in equilibrium at the higher temperature.

Femtosecond Laser Heating

Femtosecond near-IR laser-heating of Au is frequently described by a $two-temperature$ model.[12–15] For small temperature excursions ΔT of a few Kelvin, the laser pulses excite a small fraction of the conduction-band electrons, which thermalize in a few femtoseconds through electron-electron interactions.[12,14,16] The hot electrons have a large mobility,[14,17] efficiently transporting energy from the pumped (back) side of the Au layer to the front side. This initial electron temperature T_e is much greater than the resulting ΔT due to the relative size of the electronic heat capacity with respect to the total heat capacity. Thermalization of the electron and phonon temperatures occurs through electron-phonon coupling and a new thermal equilibrium is achieved in $\sim$1 ps.[17]

Larger-amplitude heating of Au has been studied in the context of femtosecond laser melting,[18] laser ablation[19] and plasma generation (warm dense matter).[20,21] The melting studies are most relevant here. To create a T-jump of hundreds of Kelvin, it is necessary to excite a larger fraction of the conduction electrons, including some of the d-band electrons. Interactions between electrons within the conduction band and between electrons and d-band holes retard the electron-lattice equilibration.[22,23] According to the improved model of Jiang and Tsai,[15] under our experimental conditions, the electron temperature should initially reach a peak temperature of $T_e \approx 2 \times 10^4$ K and the equilibration time should be $\sim$5 ps. The Au reflectivity data, Figure 6.8, clearly shows that the lattice heats up in $\sim$5 ps. This result is in good agreement with the predictions mentioned above and with the electron diffraction study of Au melting by Dwyer et al.[18]

Figure 6.8 compares the shorter-time Au-surface reflectivity trace and SFG

transients from BT and B5T SAMs. The signal losses associated with the overshoot effect occurs in the 0-0.6 ps time range. This 0.6 ps process correlates well with the 400-fs risetime that characterizes the apparatus response, opposed to the 2.5-ps electron-phonon thermalization time, the 20-ps decay of vibrational excitations, or the microsecond dissipation of the bulk sample. Thus, one could conclude that the overshoot results from a process that occurs primarily during the flash-heating pulse. Note that the back-side heating ensures that the SAM molecules never experience intense light from the flash-heating pulse directly; the overshoot is, then, associated with highly-energetic electrons present only during the flash-heating pulse.

Vibrational Excitations Generated by Au Electrons

On the basis of many studies of laser desorption of molecules from metal surfaces, it is well-known that hot electrons generated by laser pulses incident on a metal surface can create vibrational excitations in adsorbates.[12,24,25] The mechanism, in which electrons pump energy into adsorbates, is usually described as involving electron tunneling into the adsorbate, temporarily forming an anion. These anionic states decay rapidly because of strong electrostatic coupling with the metal substrate through image charges. For C_6F_6 on Cu(111), the anionic resonance lives for 7 fs,[26] and one might expect similar lifetimes for the current studies. Unfortunately, these anions are not directly detectable in these experiments. The creation and destruction of these anionic states can excite vibrations of the adsorbate molecules, which can be observed, through Franck-Condon overlap.

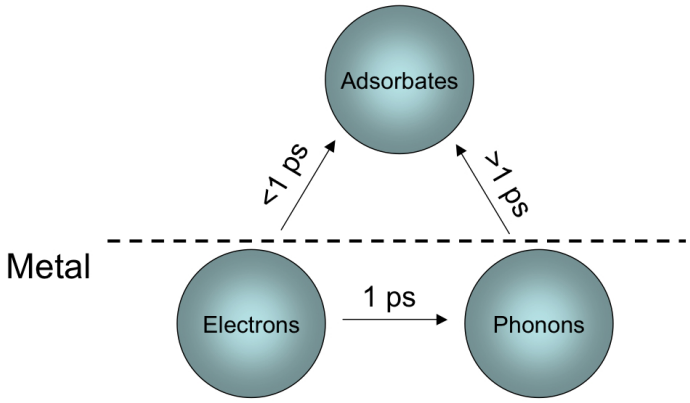

Figure 6.9: Interaction Scheme - This cartoon shows how each of the system components interacts and the corresponding time scales

Effects of Hot Electrons on SFG Spectral Intensities

The excitation of the particular vibrational mode being probed, whether it be a CH stretch or a NO_2 stretch, leads to the observed intensity overshoot. These probed vibrations have relatively-high resonant frequencies, such that, no significant thermal population will develop as a result from the flash-heating process. Thus, as the vibrational populations of these modes decay, the SFG intensity will recover. The remaining SFG intensity loss, the part associated with the molecular thermometer, is attributed to thermally-induced monolayer disordering, as in the earlier alkanethiol studies[1,2].

SFG is sensitive to both surface order[27] and vibrational populations.[28,29] As the surface order decreases, the SFG intensity decreases with an asymptotic limit of zero for a completely randomized or isotropic system. SFG intensity loss also ocurrs when the probed state becomes vibrationally excited. Both these effects

are apparent in the following frequency-domain formulation of SFG.[27]

$$I_{ppp} \propto |(N_0 - N_1) \sum_{ijk} L_p^i L_j^p L_k^p \sum_{abc} \langle (a \cdot i)(b \cdot j)(c \cdot k) \rangle \beta_{abc} E_j(\omega_{VIS}) E_k(\omega_{IR})|^2 \quad (6.2)$$

Equation 6.2 describes the p-polarized SFG intensity I_{ppp} created by the p-polarlized applied $E_p(\omega_{VIS})$ and $E_p(\omega_{IR})$ electric fields. N_0 and N_1 are the number density of molecules in the vibrational ground and first excited state; $(a \cdot i)$ is the projection of the a^{th} unit vector in the molecular reference frame onto the i^{th} unit vector in the surface frame; $\langle \cdots \rangle$ is the orientational ensemble average, and β_{abc} is the molecular hyperpolarizability in the molecular frame.

The SFG intensity can also be affected by time-varying Fresnel coefficients that change both the local electric fields $L_j^p E_p(\omega_{VIS})$ and $L_k^p E_p(\omega_{IR})$ and the reflected SFG signal field. The flash-heating pulse undoubtedly changes the optical properties of the gold substrate as seen in the reflectivity data. Mechanical processes such as thermal lensing or thermal deflection occur far too slowly to account for the faster transients observed. The reflectance near 640 nm, which is close to the SFG signal for these experiments, drops by a maximum of 5%. Further away from the interband transition region toward the probe pulses, where the optical properties are dictated by the conduction electrons or Drude electrons, the pump-induced reflectance changes are even smaller. The effects from time-varying Fresnel coefficients are easily seen in the alkanethiol data of Figure 5.3; the $artifact$ observed at $t = 0$ is due to changes in the optical properties of the Au and is a small fraction of the overall intensity loss. Undoubtably, the substrate reflectivity changes do contribute to the SFG transients for these aryl- and alkyl-thiol monolayers, but the effects are overwhelmed by thermally induced

SAM disordering and vibrational excitation of the probed modes.

Interestingly, the amount of vibrational excitation necessary to produce the observed overshoot is quite small. The benzene CH stretch $\nu = 1 \rightarrow 2$ transition is red shifted[30] by 122 cm^{-1} from the fundamental $\nu = 0 \rightarrow 1$ transition. In this limit of large anharmonic shift, the signal loss is proportional to $(1 - 2\delta)^2$,[29] where δ is the fraction of excited states. For example, BT displays a relatively large overshoot of 0.2, which corresponds to 5% CH-stretch excitation.

The underlying cause of the intensity overshoot is the existence of an excited-state population. Hence, the time constant for the overshoot recovery should be dependent on the vibrational lifetime T_1 of the particular vibration probed. According to this model, the recovery of the overshoot corresponds to $T_1/2$. For cases where the overshoot is small, extracting a precise T_1 is difficult. The data suggests a lifetime $T_1 \approx 25$ ps for BT and B1T. The vibrational lifetimes for CHT and NBT seem a bit longer, in the 40 ps range, but otherwise, all of the other SAMs seem to have T_1 in the 25-ps neighborhood.

The observed 25-ps time constant of BT is quite a bit longer than the 6-ps relaxation of CH-stretch excitations in liquid benzene.[31] Experimental conformation of this lifetimes using a more traditional techniques is difficult. If one tries to use an IR laser pulse to excite the vibration, then the surface is flash-heated and the heat flow from surface to adsorbate is likely a bigger effect than the heat flow from adsorbate to surface. This issue does not arise with non-absorbing dielectric surfaces, for instance, CO on salt.[32]

SFG Spectral Redshifts

As observed from the experimental spectra, a large portion of the vibrational modes evidence a frequency redshift after flash-heating. This redshift remains constant, in that it persists for 100s of picoseconds, for some the monolayers. While others display a more dynamic frequency response, exhibiting a strong redshift that relaxes to a more-modest value over a ∼50-ps time scale.

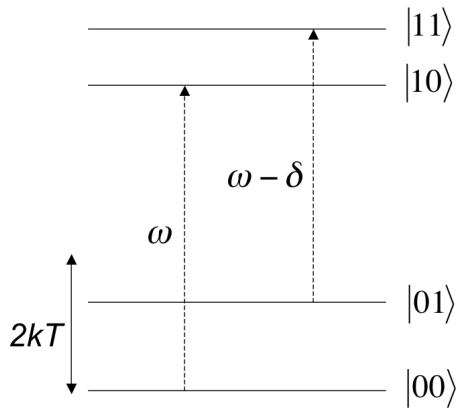

Figure 6.10: Thermally-induced redshift - The proposed mechanism for thermally-induced redshift of CH-stretch vibrations is shown in this schematic. The thermal population of lower energy vibrations move the intensity from the fundamental bands into anharmonically redshifted combination bands

The constant redshift can be described in terms of the energy-exchange model.[33] In this model the frequency redshift arises as a result of quartic anharmonic coupling between the modes being observed, designated by normal coordinate Q, and thermally-excited lower-energy modes designated by normal coordinates q. Originally developed to interpret temperature-dependent vibrational spectra of aromatic molecular crystals, this model is also applicable to SAMs, which are

essentially 2D molecular crystals. During the temperature-jump process, a large change in vibrational populations occurs for modes with energies $\leq 2kT$. For a 1500 cm^{-1} vibration, a temperature jump from 300 to 900 K, produces an increase in occupation number from $n = 7.5 \times 10^{-4}$ to $n = 0.09$ As expected, the occupation numbers increase even more for lower-energy vibrations. These vibrations remain in the excited state for several nanoseconds until entire monolayer-substrate system cools. Thus, the resulting redshift will also persist for at least 100s of picoseconds, as observed.

For C6, the observed redshifting transition is the fermi resonance the of the bending mode δCH_3 $\nu = 0 \rightarrow 2$ transitions with the other methyl stretches. The thermal excitation of the $\nu = 1$ bending-mode state draws intensity away from the $\nu = 0 \rightarrow 2$ transition into the anharmonically shifted $\nu = 1 \rightarrow 3$ transition. In this case, the thermally-excited mode and the mode being observed are the same mode. The relevant anharmonic coupling term has the form Q^4.[33–36]

In the aromatic molecules, *i.e.* BT, the lower-enegy CH-bending, ring-rocking, and ring-deformation modes will be thermally excited and are anharmonically coupled to the observed transitions through mixed-mode couplings of the form Q^2q^2.[33–35] These mixed-mode couplings lower the combination-band transition energy, leading to a shifted component in the spectrum.

The more dynamic frequency shifting behavior can be explained in a nearly-identical model. In this case, lower-energy vibrational modes are excited during the flash-heating process by inelastic electron scattering. The non-zero occupation numbers of these vibrational modes cause a redshift to occur by redirecting intensity from the fundamental band to the anharmonically-shifted combination band. This effect is caused by the same mixed-mode couplings that result in the

thermally-induced shift.

The difference between the two models is that the hot electrons excite certain vibrational modes to quasi-temperatures much larger than the long-time equilibrium temperature. Accordingly, strong redshifts will occur with the non-thermal excitation of the certain vibrational modes that are anharmonically coupled to the probed vibration. As the non-thermal vibrational population relaxes, dissipating energy into other lower-energy modes, the redshift lessens.

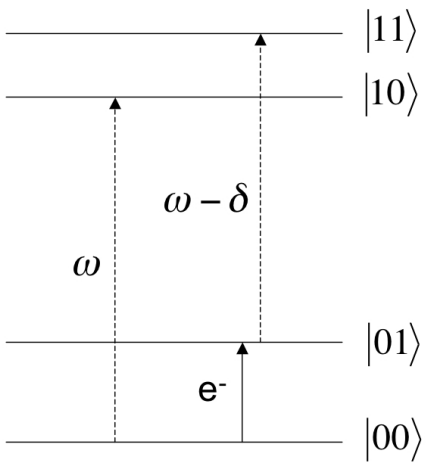

Figure 6.11: Redshifts from inelastic electron scattering - This schematic describes the population of lower-energy vibrational modes through inelastic electron scattering. The excited vibrational states lead to frequency shifts as the excited molecules make combination-band transitions instead of fundamental transitions

2-Methyl Benzenethiol

The experiments with 2MBT are especially interesting; two different parts of the molecule – the phenyl ring ϕCH and the methyl substituent CH_3 – can be simultaneously probe. Figure 6.5 shows clear differences in the dynamics of both the ϕCH and the CH_3 groups in response to flash heating. Operating from the premise that the CH_3 group, which shows no overshoot, acts as a molecular thermometer similar to that of the alkanethiols, and the dynamic response can be attributed to the monolayer disordering. The ϕCH group, on the other hand, is sensitive to both monolayer disordering and an excited-state population excited by hot electrons.

Equation 6.2 suggests that, if we divide the 2MBT ϕCH-group dynamics by the 2MBT CH_3-group dynamics, then a function proportional to the square of the vibrational dynamics $N_0 = N_1$ can be obtained. The results of this manipulation are shown in Figure 6.12. The vibrational dynamics, having an instantaneous rise, confirms the view that excitations of the higher-frequency transitions probed by SFG are created during the flash-heating pulses. The decay of this trace exhibits the 25-ps time constant associated with the vibrational T_1 of these excitations.

The decay of the 2MBT CH_3-group dynamics in Figure 6.2 results from thermal disordering, which is dependent on both the rate of heat flow across the Au-SAM interface and the intrinsic response time for a hot SAM to disordered. Based molecular simulations, the response time for alkanethiol monolayers was 0.5 ps.[1,2] In other words, the SFG thermometer had a response time of 0.5 ps. Thus, any significantly longer time constants should be associated with heat flow rather than an intrinsic response time of the thermometer. Figure 6.12 presents

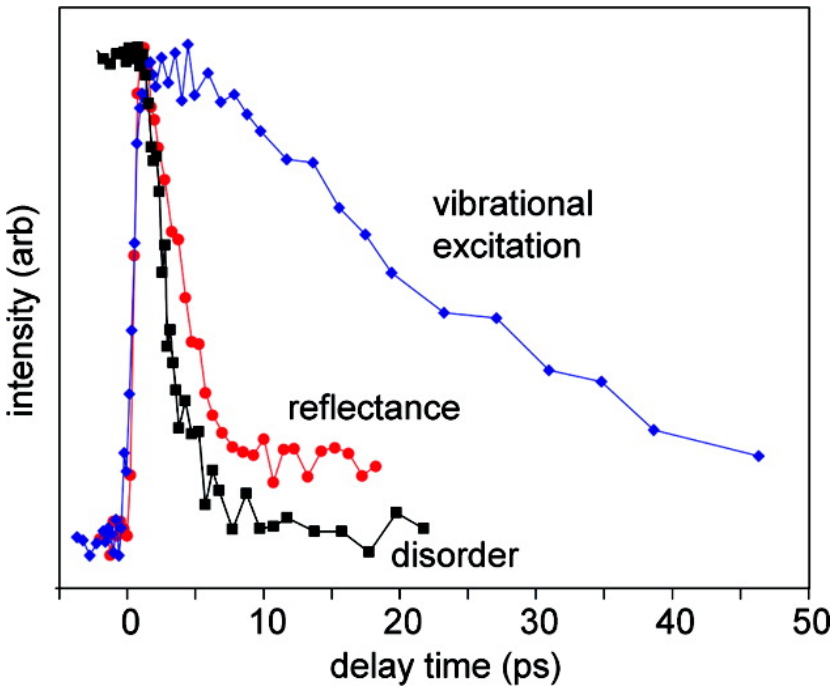

Figure 6.12: Separation of electron and phonon heating effects - From the 2-methyl benzenethiol (2MBT) data in Figure 6.5, we used Eq. 6.2 to compute the vibrational excitation of the phenyl CH stretch (blue diamonds). A comparison to the Au surfaces reflectance data (red circles) shows these vibrational excitations were created only during the reflectance rise, which represnents the laser time response, so they must be excited by hot non-thermal electrons generated during the flash-heating pulses. The 2MBT mehtyhl signal corresponds to the time for the SAM to undergo thermal disordering. The disordering is slightly faster than the reflectance decay. The reflectance decay approximately corresponds to the rate of heating the Au lattice to the final temperature.

the square root of the methyl SFG data, which is linear in the orientational-dynamics term. The time dependence can be fit by an exponential function with a time constant of 3 ps, which is interpreted as the time for SAM disordering. This disordering process appears to occur slightly faster than the decay of the reflectance data, which represents the time for Au phonons to thermalize with the higher-temperature electrons. In reality, the time constants are quite similar. The apparent illusion results because the normalized reflectance change returns to a non-zero value after 10s of picoseconds due to the effects of the phonon temperature on the reflectance.

Note that the monolayer response or the molecular thermometer will begin to saturate at a given temperature. Once a significant amount of disorder is present, further increases in monolayer temperature no longer lead to additional disorder. With a comparatively ridged molecular structure, most of the monolayer disorder is expect to occur by the excitation of libration modes, causing the individual molecules to rock back and forth in an uncoordinated dance. However, for these temperature jumps, the 2MBT acts as a reliable molecular thermometer, mirroring the thermoreflectance data identically.

Distance Dependence of Electron Excitation

Several observations suggest that the likelihood of vibrational excitation by electrons decreases for moieties connected to the surface by 4-6 or more carbon atoms. The intensity overshoot becomes minimal for alkanes C6 and longer. Additionally, the overshoot is minimal for benzenes spaced 5 carbon atoms (B5T) from the surface.

The results for substituted benzenes raise some interesting questions that

could form the basis for further investigations. In the phenyl, biphenyl, and terphenyl series, the overshoot decreases with increasing distance from the Au surface as with the benzene-linker molecules. The overshoot is large for the nitro transitions of NBT, which seems reasonable since the nitro π electrons are part of the coupled aromatic π-electron system. Electron tunneling onto the coupled phenyl-nitro orbitals would be expected to generate vibrational excitations of both moieties. An interesting case is the methyl substituent in 2MBT, which shows no overshoot. This methyl group is close to the Au surface, viewed either in physical space or by the spacing in units of carbon atoms. This puzzling observation is suggestive that electron heating of the methyl CH-stretch vibrations may be forbidden by a selection rule, which might provide evidence for the creation of short-lived anionic species as a source of the pumping mechanism mentioned earlier in this Section. On the other hand, the phenyl rings, may simply have an larger cross-section for inelastic electron scattering.

The Overall Effect of Electron Heating

Compared with the thermal energy supplied by the Au lattice, the vibrational excitations of the monolayer by the surface electrons represents a relatively small fraction of the total energy. In one of the more dramatic cases – the large overshoot of BT – hot electrons excited $\sim$5% of the probed CH stretch at 3070 cm^{-1}, corresponding to 150 cm^{-1} per molecule of the SAM or 1.8 kJ M^{-1}. By taking the heat capacity C_p of benzene to be 135 J $M^{-1}K^{-1}$, the electron-excited CH stretch accounts for just 13 K of the 600 K temperature rise. The effect of these hot electrons on other ϕCH stretches in BT are unknown, due to their absence in the sum-frequency spectra. For example, if all the A'-symmetry (C_S) ϕCH stretches

are excited with a similar 5% efficiency, the electron excitations lead to a temperature rise of 39 K. Therefore, the heat deposited into the monolayer by electron excitation is relatively small, even though the effects of electron excitation on the SFG intensity are not small.

Most of the vibrational transitions are not monitored by SFG; to understand how much energy is in these unobserved transitions, it is instructive to consider cases where the monolayers consist of a *base region* close to Au, where electron excitation occurs, and a spatially-distant *reporter region*. One of these systems is TPhT, and a helpful comparison between the redshift overshoots of BT and TPhT follows. Looking at the BT-monolayer spectra in Figure 6.4, there is an observable redshift overshoot; Figure 6.12 shows this feature more quantitatively. The redshift originates from the excitation of lower-energy vibrations that are anharmonically coupled to the probed CH-stretch transition, most likely ring and CH deformation modes in the 500-1500 cm^{-1} range. Now, there are two limiting cases: (1) electron heating is a significant effect, such that, the hot electrons excite all the vibrations in this frequency range to levels that temporarily correspond to temperatures even greater than 600 C. This would undoubtedly lead to an observed redshift overshoot, similar to that of the BT monolayers. Or (2), the electron heating is a negligible effect, and few anharmonically-coupled vibrational modes are excited that produce the observed redshift overshoot. If the first case were correct, then for the TPhT experiments, a substantial amount of vibrational energy initially deposited in the phenyl *base region* would rush into the other phenyl rings, leading to an observable redshift overshoot. In TPhT, no redshift overshoot is observed, indicating that the second case is likely correct and the relative amount of heating by electrons is small with respect to phonon heating.

One reasonable scenario is that the BT redshift overshoot results from electrons generating 5-10% excitation of 5-10 lower-energy (500-1500 cm^{-1}) vibrations of BT, having large electron-scattering cross sections and relatively-strong anharmonic coupling to the probed vibration. In this event, the total energy delivered to unobserved vibrations with an average energy of 1000 cm^{-1} would be a few hundred cm^{-1}, leading to an additional few tens of Kelvin temperature increase.

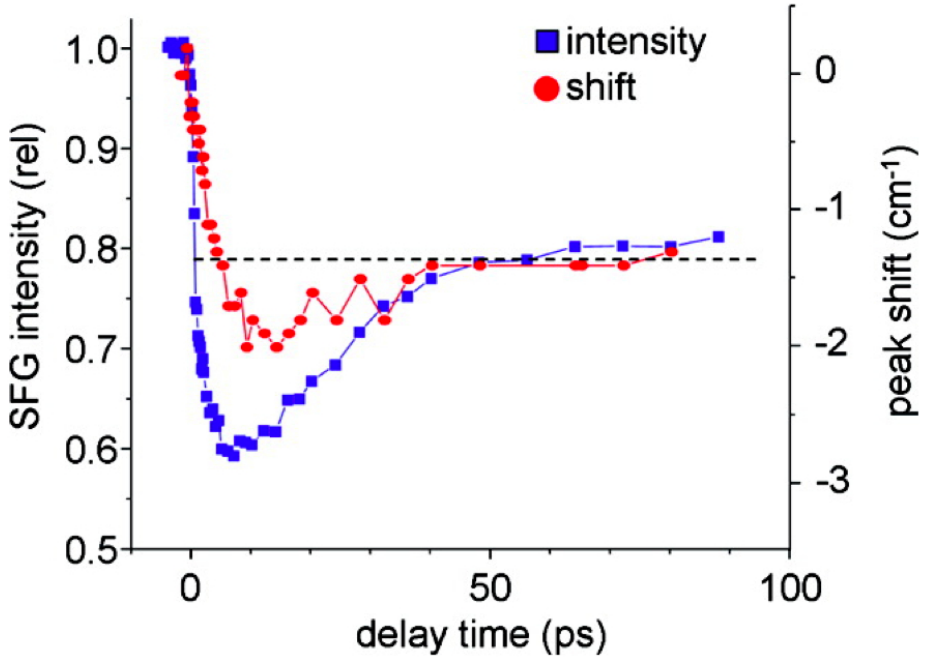

Figure 6.13: Benzenethiolate dynamics - SFG intensity loss from benzenethiol (BT) SAM on Au after flash-heating to ~600 °C shows a significant overshoot from the longer-time equilibrium value. The intensity overshoot is associated with the very fast intensity drop occurring in the first ~600 fs, which is not seen in longer-chain alkanethiols. The peak redshift shows a smaller overshoot.

6.4 Summary

These experiments were conducted to better understand energy transfer from flash-heated Au surfaces to thiolate SAMs, extending the prior flash-thermal calorimetry studies of C6-C24 alkanes to SAMs having probed groups closer to the Au surface. The main points are summarized below.

The aromatic BT monolayer(Fig. 6.13) evidences a significant overshoot in the SFG-intensity loss of the ϕCH and a much smaller overshoot in the CH-stretch frequency redshift. The intensity overshoot phenomenon is not limited to aromatic SAMs, since it also observed in cyclohexanethiol and in the shortest alkanethiol studied, C6. The time dependence of the overshoot shows that it results from excited Au electrons present only during the 300 fs flash-heating pulses. The SFG intensity loss is consistent with a proposed mechanism where these hot electrons directly excite the ϕCH-stretch transition being probed. The intensity overshoot represents relaxation of this excess vibrational energy. Due to the high sensitivity of SFG intensity loss to vibrational excitation, no more than a few percent of the SAM molecules need CH-stretch vibrational excitations to account for even the largest observed overshoots. The redshift overshoot is associated with hot-electron excitation of lower-energy vibrations that are anharmonically coupled to the probed vibration.

The studies with benzene-linker molecules indicate that surface electron excitation of SAM vibrations becomes inefficient when the probed groups are offset from the Au surface by a distance ranging between 4-6 methyl groups. This view is also supported by our alkanethiol studies, where only the shortest alkanethiol, C6, evidenced any overshoot at all. This work has now shown that phonon heat-

ing is the dominant heat transfer mechanism, since the total energy transfer from hot electrons is relatively small.

Energy transferred by hot surface electrons directly to probed vibrations of functional groups lying close to the Au surface has a disproportionately large effect on the SFG signal for the first few tens of picoseconds. Thus, in SAMs evidencing large overshoots on the greater-than-30-ps time scale, the SFG signal is not a faithful molecular thermometer. Although the electron heating process hinders the study of ultrafast heat flow in SAMs, it is useful for creating nonthermal vibrational populations in SAMs whose relaxation processes can be investigated. Since the original focus of this work is primarily interested in heat flow, monolayer systems such as the alkane chains, where short-time heat flow is directly reflected in the SFG signal. In this regard, the 2MBT and TPhT molecules are very interesting, since there is little or no overshoot when probing the CH3 substituent of 2MBT or the terminal phenyl group of the terphenyl moiety. It then appears that alkyl-substituted phenyl SAMs or polyphenyl SAMs would be reasonable systems to understand heat flow in molecule wires that incorporate aromatic moieties.

6.5 References

1. Wang, Z.; Cahill, D. G.; Carter, J. A.; Koh, Y. K.; Lagutchev, A.; Seong, N.-H.; Dlott, D. D. Chem. Phys. 2008, 350, 31.
2. Wang, Z.; Carter, J. A.; Lagutchev, A.; Koh, Y. K.; Seong, N.-H.; Cahill, D. G.; Dlott, D. D. Science 2007, 317, 787.
3. Carter, J. A.; Wang, Z.; Dlott, D. D. J. Phys. Chem. A 2008, 112, 3523.
4. Cahill, D. G.; Ford, W. K.; Goodson, K. E.; Mahan, G. D.; Majumdar, A.; Maris, H. J.; Merlin, R.; Phillpot, S. R. J. Appl. Phys. 2003, 93, 793.
5. Segal, D.; Nitzan, A. J. Chem. Phys. 2002, 117, 3915.
6. Segal, D.; Nitzan, A.; Hnggi, P. J. Chem. Phys. 2003, 119, 6840.
7. Galperin, M.; Ratner, M. A.; Nitzan, A. J. Phys.: Condens. Matter 2007, 19, 103201.
8. Lagutchev, A.; Hambir, S. A.; Dlott, D. D. J. Phys. Chem. C 2007, 111, 13645.
9. Harris, A. L.; Chidsey, C. E. D.; Levinos, N. J.; Loiacono, D. N. Chem. Phys. Lett. 1987, 141, 350.
10. Carter, J. A.; Wang, Z.; Dlott, D. D. Proceedings of the XXIst International Conference on Raman Spectroscopy; Withnall, R., Chowdhry, B. Z., Eds.; IM Publications LLP: Charlton, Chichester, 2008; p 112.
11. Joo, S.-W.; Chung, H.; Kim, K.; Noh, J. Surf. Sci. 2007, 601, 3196.
12. Frischkorn, C.; Wolf, M. Chem. Rev. 2006, 106, 4207.
13. Groeneveld, R. H. M.; Sprik, R.; Lagendijk, A. Phys. Rev. B 1992, 45.
14. Juhasz, T.; Elsayed-Ali, H. E.; Smith, G. O.; Surez, C.; Bron, W. E. Phys. Rev. B 1993, 48.
15. Jiang, L.; Tsai, H.-L. J. Heat Transfer 2005, 127, 1167.
16. Zhigilei, L. V.; Leveugle, E.; Garrison, B. J. Chem. Rev. 2003, 103, 321.
17. Brorson, S. D.; Fujimoto, J. G.; Ippen, E. P. Phys. Rev. Lett. 1987, 59, 1962.

18. Dwyer, J. R.; Jordan, R. E.; Hebeisen, C. T.; Harb, M.; Ernstorfer, R.; Dartigalongue, T.; Miller, R. J. D. J. Mod. Opt. 2007, 54, 905.

19. Zhigilei, L. V.; Garrison, B. J. Proc. SPIE Int. Soc. Opt. Eng. 1998, 3254, 135.

20. Ping, Y.; Hanson, D.; Koslow, I.; Ogitsu, T.; Prendergast, D.; Schwegler, E.; Collins, G.; Ng, A. Phys. Rev. Lett. 2006, 96, 255003.

21. Ernstorfer, R.; Harb, M.; Hebeisen, C. T.; Sciaini, G.; Dartigalongue, T.; Miller, R. J. D. Science 2009, 323, 1033.

22. Hu, M.; Petrova, H.; Hartland, G. V. Chem. Phys. Lett. 2004, 391, 220.

23. Chan, W.-L.; Averback, R. S.; Cahill, D. G.; Ashkenazy, Y. unpublished 2009, 102, 09570

24. Antoniewicz, P. R. Physical Review B 1980, 21.

25. Franchy, R. Reports on Progress in Physics 1998, 61, 691.

26. Vondrak, T.; Zhu, X.-Y. The Journal of Physical Chemistry B 1999, 103, 3449.

27. Shen, Y. R. The Principles of Nonlinear Optics; Wiley: New York, 1984.

28. Bredenbeck, J.; Ghosh, A.; Smits, M.; Bonn, M. J. Am. Chem. Soc. 2008, 130, 2152.

29. Ghosh, A.; Smits, M.; Sovago, M.; Bredenbeck, J.; Mller, M.; Bonn, M. Chem. Phys. 2008, 350, 23.

30. Reddy, K. V.; Heller, D. F.; Berry, M. J. J. Chem. Phys. 1982, 76, 2814.

31. Ewing, G. E. Acct. Chem. Res. 1992, 25, 292.

32. Seong, N.-H.; Fang, Y.; Dlott, D. D. J. Phys. Chem. A 2009, 113, 1445.

33. Shelby, R. M.; Harris, C. B.; Cornelius, P. A., J. Chem. Phys. 70 1979.

34. Harris, C. B.; Shelby, R. M.; Cornelius, P. A., Phys. Rev. Lett. 38, 1415, 1977.

35. Marks, S.; Cornelius, P. A.; Harris, C. B., J. Chem. Phys. 73, 3069, 1980.

36. Califano, S; Schettino, V.; Neto, N., Lattice Dynamics of Molecular Crystals, Springer-Verlag, Berlin, 1981.

7

Simulating Time-Dependent Sum-Frequency Signals[1]

7.1 Introduction

It is difficult to study molecules at surfaces or interfaces because the total number of molecules is small, and this is especially problematic in studies of interfacial molecular dynamics with ultrafast time resolution. Vibrational sum-frequency generation spectroscopy (SFG), where infrared (IR) and visible pulses are combined at an interface, has emerged as a powerful method to probe interfacial molecular dynamics. The nonlinear coherent nature of SFG helps overcome the sensitivity issues, especially when femtosecond IR pulses are used. With femtosecond pulses, a range of vibrational transition can be probed simultaneously and ultrafast time resolution can be achieved.

Ultrafast SFG experiments use three pulses, a pump pulse to generate non-

[1]Parts of the research presented here have been previously published as: Carter, J. A.; Wang, Z.; Dlott, D. D., Acc. Chem. Res. 42, 9, 2009.

equilibrium conditions with a probe pair, and two time-delay parameters. Mapping the sum-frequency intensity as a function of the tow time delays creates a two-dimensional surface, where one axis t_1 provides information about molecular dynamics driven by the pump pulse, and the other axis t_2 provides information about the dynamics of the vibrational resonances.

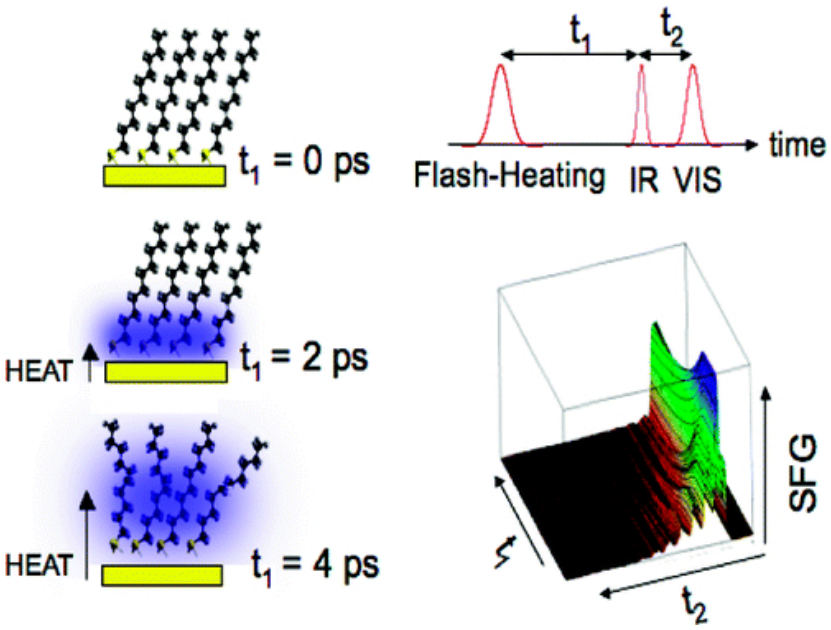

Figure 7.1: Pulsing diagram and corresponding signals - The molecular conductance experiments require three laser pulses with two corresponding relative timings. As these timings are adjusted, the two-dimensional sum-frequency signal changes accordingly. As the monolayer disorder increases the observed signal decreases along the t_1 slices. Along the other dimension, the signal decays and oscillates base on the resonant frequencies and the dephasing times.

This chapter analysis the 2D SFG method and reaches some unexpected, yet straightforward conclusions about how varying t_1 and t_2 affect the sum-frequency signals. Time-resolved SFG measurements are usually made using a visible probe pulse that is effectively infinite in duration. This reduces the signal down to a function dependent on pump-IR probe delay, t_1. Unfortunately, in this case, the

SFG signals have a large contribution from non-resonant sources, such as metal surfaces. This effect increases in the amount of noise. The non-resonant (NR) signal can be suppressed by inducing the time delay t_2 between the two probing pulses. Within this 2D SFG structure, one might expect that information about the molecular response to the pump pulses would be contained in slices along the t_1 axis. This is, however, not the case and by simulated the experiment one can see that the t_1 and t_2 parameters are not independent, but interact. Changing t_2 to suppress the NR signal cause the t_1 slices to shift in time.

7.2 2D SFG Simulations

This section describes simulations of 2D SFG with either time-asymmetric narrowband visible (NBVIS) pulses of femtosecond visible (fs-VIS) pulses. The flash-heating pulse was modeled with a 150-fs duration and arrived at the sample at t_1. The monolayer disorder was modeled phenomenologically with an effective exponential time decay $\tau = 2.5$ ps and with a delay time $t_0 = 0$ ps. See §5.3 for a discussion of these parameters. The broadband infrared pulse (BBIR), centered at $t = 0$, is given a 300-fs duration. Two different models for the visible pulse were used. The time-asymmetric NBVIS had a 300-fs rise and a 1-ps exponential decay, while the fs-VIS had 150-fs duration. Both visible pulses had an arrive time of t_2.

Within the simulations all vibrational resonance within the pulse bandwidth would be coherently excited, along with a non-resonant source term having a relative phase of π. This first-order polarization $P^{(1)}$ was then allowed to evolve with the corresponding frequency oscillations and characteristic dephasing terms.[1–3]

The time-evoled $P^{(1)}$ was up-converted into a second-order polarization $P^{(2)}$ in the presence of the visible pulse which radiated at the sum frequency.[1–3] The sum-frequency field was then time integrated on a model square-law detector.

Two monolayer models were used. The first model had one vibrational resonance with $T_2 = 1.5$ ps ($\Delta\nu = 16$ cm-1) intended to represent a benzenethiol monolayer. The other model, simulating an alkanethiol monolayer, had three vibrational resonances with intensities and linewidths needed to approximately reproduce the experimental spectrum.

Results

The t_1 slices in Figure 7.2 and 7.3 are expressed as VRFs – previously discussed in §5.2. Perhaps a disturbing feature of these t_1 slices is that the time where the initial change of the VRF is not at a constant t_1, but instead varies with t_2. This is understood from the timing diagrams in Figure 7.1, which show the flash-heating pulse arriving at t_1. The SFG signal, however, is not emitted until a time window near t_2. Thus the pump-induced thermal disorder will be observed when the pump pulse arrives first, $-t_1 < t_2$ With a nonzero value of t_2 to suppress theNR signal, the time delay where the VRF first rises is no longer t_0, but becomes $t_0 - t_2$. The was not a problem for the interpretations of the t_0 in the original alkanethiol experiments presented in Chapter 5, because the NR-suppression technique was not employed. In future experiments with NR suppression, an accurate determination of t_0 will require a careful measurement of t_2 as well.

Other interesting features of the t_1 slices also became apparent after these simulations. When femtosecond visible pulses were used, the initial change of the

VRF became more abrupt than with the narrowband pulses, indicating an improvement in time-resolution. With femtosecond visible pulses, the sum-frequecy signals are emitted over a shorter time window.[4–6] This enhanced time resolution results in a significant broadening of the vibrational resonances in the frequency domain. Additionally, with a femtosecond visible pulse, the sum-frequency spectra of samples with unresolved spectral features are strongly dependent on the t_2 delay. This spectral dependence on t_2 turns is quite useful when trying to precisely matching delay times for multiple samples of the same monolayer. Picosecond visible pulses provide better spectra resolution, but with worst time resolution. Realistically, the experiments discussed within this thesis do not benefit from the enhanced time resolution afforded by femtosecond pulses; slight motion of sample plane dictates the inherent time resolution of the instrument. Different experiments could, on the other hand, benefit from the application of femtosecond visible pulses.

The VRF shape is also dependent on the t_2 time delay in other, more subtle respects. The dependence of the signal on the monolayer disorder changes with t_2. With relatively short t_2, such that NR signals are also observed, the sum-frequency signal is observed as a coherent interference between the resonant polarization and non-resonant polarization terms, having a relative phase difference of ϕ,

$$I_{SF} \propto |P_R^{(2)} + P_{NR}^{(2)}|^2 = |P_R^{(2)}|^2 + 2|P_R^{(2)}||P_{NR}^{(2)}|cos\phi + |P_{NR}^{(2)}|^2. \tag{7.1}$$

Depending on the relative magnitudes of the resonant and non-resonant polarizations, the functional form various continuously from $|P_R^{(2)}|^2$ in the limit of small

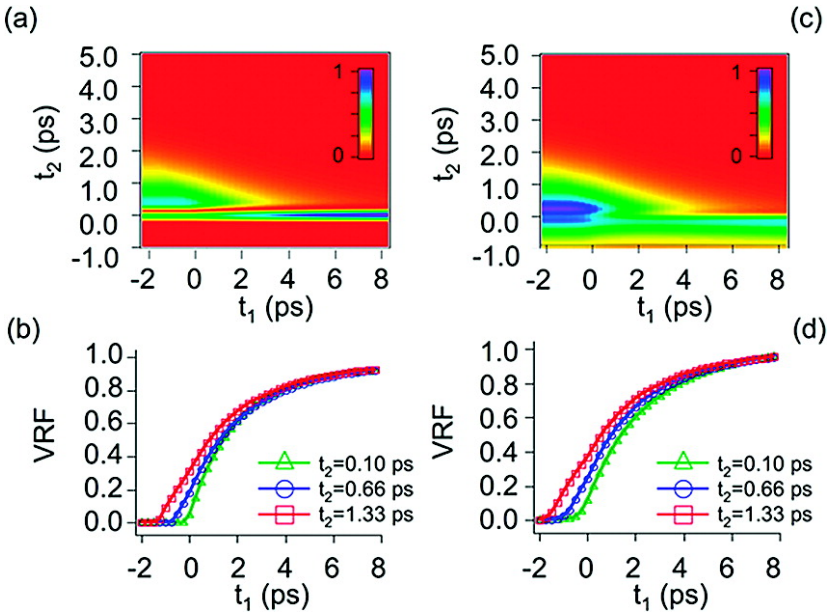

Figure 7.2: Simulated 2D SFG signals for one oscillator - The frequency-integrated signal for a single oscillator against a non-resonant background using either femtosecond or picosecond pulses. The t_1 axis is the delay between the flash-heating and BBIR pulses. The t_2 axis is the delay between the BBIR and visible pulses. (b), (d) VRFs obtained from slices along the t_1 axis for the indicated values of t_2

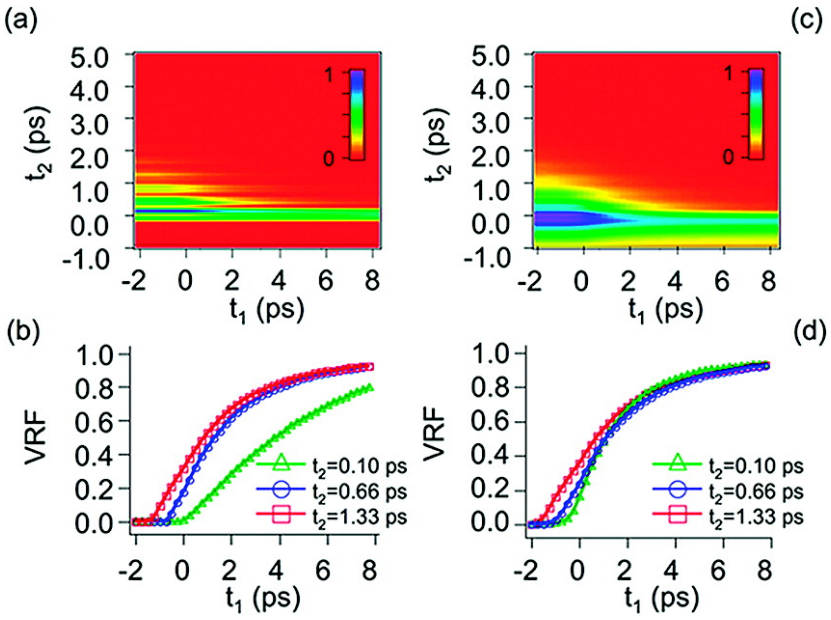

Figure 7.3: Simulated 2D SFG signals for three oscillators - The frequency-integrated signal for three oscillators against a non-resonant background using either femtosecond or picosecond pulses. The t_1 axis is the delay between the flash-heating and BBIR pulses. The t_2 axis is the delay between the BBIR and visible pulses. (b), (d) VRFs obtained from slices along the t_1 axis for the indicated values of t_2

non-resonant signal to $2|P_R^{(2)}||P_{NR}^{(2)}|cos\phi + |P_{NR}^{(2)}|^2$ in the large non-resonant limit. The time dependence of the monolayer disorder is contained in the resonant polarization term. Thus different values of t_2 lead to different resonant-to-non-resonant ratios, and thus different signal decay dynamics would be observed for the same monolayer, despite the fact that the monolayer is responding identically in both experiments.

Another interesting effect that is not readily observed in experiments due to artifacts and noise is a discontinuity in the first derivate or a slight kink of the signal near $t = 0$. If one thinks about the various time orderings of the three pulses through out a complete experiment this effect is reasonably understood. For $t_1 > t_2$, such that both the probe pulses arrive at the sample prior to the that of the pump pulse, then no energy is transferred into the monolayer and no thermal disorder is present. Accordingly, in this case, the signal is completely unchanged. As the optical delay t_1 is decreased, the time ordering of the pulses changes and the pump pulse arrives at the sample in between the infrared and visible probe pulses. Here, the infrared pulse creates an undisturbed vibrational coherence, which after the arrival of the pump pulse, the monolayer starts to disorder and the resulting second-order polarization is reduce. With further decrease of the optical delay for the pump pulse, the pulse order changes again. Now, the pump pulse generates orientational disorder that affects the magnitude of both the first-order and second-order material polarizations. The kink observed in the simulated data occurs at $t = 0$, where pump pulse exchanges positions with the IR-probe pulse.

Experimental Verification

In Figure 7.4, a time-asymmetric narrowband visible pulse was used to demonstrate the effect of t_2 on the determination of t_0. The peak feature at $t = 0$ ps is an artifact resulting from interactions of the IR pulse with the pump pulse, and it serves as a fiducial zero-time marker. As the t_2 delay is increased, one can easily see how the resultant sum-frequency signal changes. Interpreting this

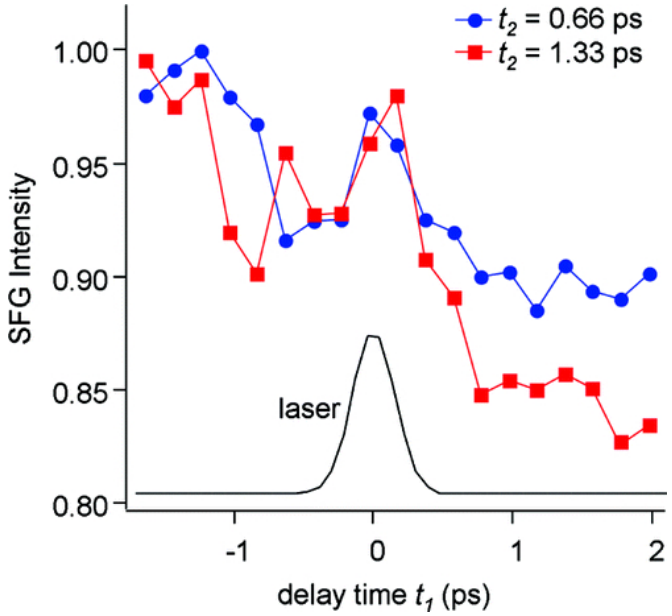

Figure 7.4: Effects of t_2 - Sum-frequency signal from an alkanethiol monolayer after flash-heating using a time-asymmetric narrowband visible pulse to suppress the non-resonant background. the curve denoted "laser" is the cross correlation between the pump and the broadband IR pulses. The feature near $t = 0$ is an artifact used as a fiducial time zero. As t_2 is increased, the loss of sum-frerquency signal occurs at earlier values of t_1.

signal is unfortunately not straight. The initial loss of sum-frequency signal is due to pump-induced changes in the Fresnel coefficients of the metal surface, which recovers in ∼2 ps. This effect is reasonably well understood as discussed in Chapter 3. Changes in the signal after ∼2 ps are caused solely by monolayer

disorder, and the data clearly shows that the $t_2 = 1.33$ ps signal has lost more intensity relative to the $t_2 = 0.66$ ps signal at any given time delay. To obtain accurate values of the t_0, then the data must be fit while taking these factors into consideration.

Non-Resonant Suppression

While the suppression of NR signals has been mentioned throughout this chapter, there has yet to be any detailed discussion of this technique until here. NR signals that interfere with the vibrationally-resonant signals are in general electronic in nature, either caused by the system of interest or other species present at the interface under study. The strength of the NR signals vary from interface to interface. For this work, NR signals generated by the Au-surface electrons are significant, generally an order of magnitude or so larger than the resonant signals and approximately 180° out of phase.

Due to the non-resonant nature of this signal type, the NR spectral features are very broadband. If fact, the NR features mirror the IR spectrum, which spans ~ 300 cm^{-1}. Owning to the broadband nature of this coherent response, the first-order NR signal dephases rapidly and for all practical purposes the second-order NR signal is only emitted when both probe fields overlap within the interface simultaneously. The vibrationally-resonant coherences, on the other hand, dephase with a characteristic $T_2 \gtrapprox 1$ ps and a second-order signal can be generated with a t_2 delay of several multiples of T_2.

For this discussion, the frequency-domain sum-frequency signal can be written such that it is proportional to the Fourier transform of the coherent second-order

polarizations,

$$I_{SF}(\omega, t_1, t_2) \propto |\int_{-\infty}^{\infty} (P_R^{(2)}(t, t_1, t_2) + P_{NR}^{(2)}(t, t_1, t_2)) e^{-i\omega t} dt|^2. \tag{7.2}$$

As t_2 is increase, $P_{NR}^{(2)}(t, t_1, t_2)$ decreases rapidly. Only an increase of several hundred femtoseconds is required to completely suppress NR signals, while the resonant signal remains. The sum-frequency signal then becomes only a function of the resonant sources,

$$I_{SF}(\omega, t_1, t_2) \propto |\int_{-\infty}^{\infty} P_R^{(2)}(t, t_1, t_2) e^{-i\omega t} dt|^2. \tag{7.3}$$

The experimental realization of NR signal suppression is shown for an alkanethiol monolayer in Figure 7.5.[7] This data in this figure was taken by Selezion Hambir. Without suppression, the vibrational resonances are observed as dips on a broadband NR background. While an increase of t_2 from 0 to 200 fs leads to a complete suppressed background and the vibrational resonances are detected as positive peaks. Between those two extreme the sum-frequency spectra are complicated by near-equal contributions of the resonant and non-resonant polarizations.

The experiments discussed in Chapter 5 were conducted without NR suppression techniques, which is clear from the spectra shown in §5.2. The remaining experiments made use of this technique.

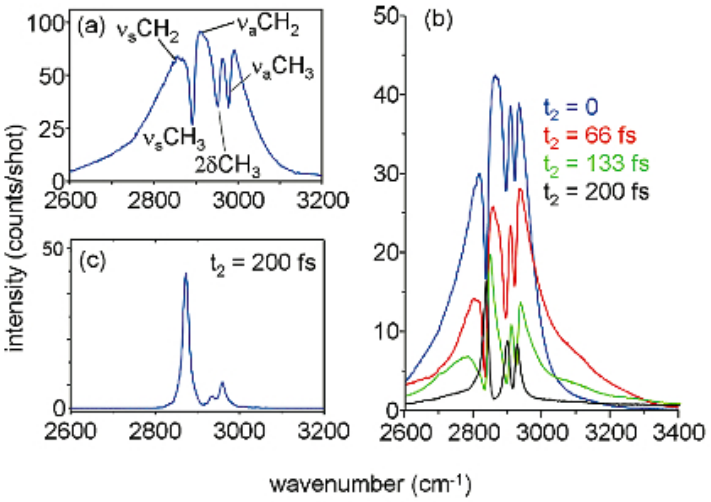

Figure 7.5: Non-Resonant Background Suppression - (a)Experimental SFG spectrum of 18-carbon alkanethiolate monolayer on Au without non-resonant suppression. (b) Similar spectrum using a time-delayed time-asymmetric narrowband visible pulse. As the time delay t_2 between the broadband infrared pulse and the narrowband visible pulse is increased, the non-resonant contribution disappears. (c) Similar spectrum with the non-resonant background is completely suppressed.

7.3 Summary

SFG is a powerful method for probing ultrafast processes at surfaces and interfaces, despite the sensitivity issues posed by the small number of interfacial molecules. In contrast to an ordinary pump-probe measurement with two pulses and a single delay time, an ultrafast SFG experiment has three pulses, one pump pulse and two probe pulses, and two delay times. Such SFG experiments are both two-dimensional and coherent. Using examples drawn from studies of flash-heating measurements of thermal transport through interfacial molecules, we first described results obtained with the simpler case where the visible probe pulse is effectively infinite in duration, with only a single delay-time parameter. The problems with this method stem from the NR background and the time resolu-

tion limited not by the laser parameters, but by intrinsic molecular dephasing rates.

We described, simulated and presented results from measurements using a visible pulse what was either a single-sided picosecond pulse or a femtosecond pulse. We showed that we could suppress the NR signal and achieve femtosecond time resolution of the probing process, but always with a trade-off. When the NR signals were suppressed by delaying the visible pulse by a time t_2, the molecular response also shifted in time, so an accurate measurement of the molecular response requires an additional knowledge of t_2. With a femtosecond visible pulse, better time resolution could be achieved, but the ability to resolve individual vibrational transitions may be lost. In all these situations, unique information about the ultrafast dynamic behavior of interfacial molecules can be obtained.

7.4 References

1. Shen, Y. R., The Principles of Nonlinear Optics, Wiley-Interscience, New York, 1984.

2. Boyd, R. W. Nonlinear Optics, 2^{nd} Ed. Academic Press, 2003.

3. Mukamel, S. Principles of Nonlinear Optical Spectroscopy. Oxford University Press, Oxford, New York, 1995.

4. Roke, R.; Kleyn, A. W.; Bonn, M., Chem. Phys. Lett. 370,227, 2003.

5. McGuire, J. A.; Beck, W.; Wei, X.; Shen, Y. R., Opt. Lett. 24, 1877, 1999.

6. Bordenyuk, A. N. Jayathilake, H. D.; Benderskii, A. V., J. Phys. Chem. B, 109, 15941, 2005.

7. Lagutchev, A.; Hambir, S. A.; Dlott, D. D., J. Phys. Chem. C, 111, 13645, 2007.

8

Appendix

This chapter contains various scripts used to either collect or analysis data presented in this thesis. Data collection scripts for both the thermoreflectance and the molecular conductance experiments are shown in Figures 8.1 and 8.2, respectively. An additional scripted used to control only the optical delay for the pumping pulse is shown in Figure 8.3. The scripts that drive the servo motors for the sample motion control are in Figure 8.4 and 8.5. The thermoreflectance experiments generate large data files and an analysis script, shown in Figure 8.6, was written to average and then reduce the raw data. And the script used to simulate the 2D-SFG experiments is shown in Figure 8.7.

```
rem This program collects pump-probe data for the fs-WL thermoreflectivity experiments.

rem sets delay in milliseconds
d=1000

input("Enter File Name", file$)

rem Background Acq
SetAcquisitionType(1)
run()
rem Set Data Acq
SetAcquisitionType(0)

baud(1,9600)

rem Set Delay Communication
comwrite(1,">>01\r")
comwrite(1,"LD*\r")
comwrite(1,"IHX*\r")
rem delay(10000)
comwrite(1,"IN*\r")

rem Closes Shutter
auxout(1,0)

rem variable to keep track of pump-probe delay
dline = 0.00

rem counter for number of delays
n=0
while(n<40)

rem Data from -2ps to 2ps; 17 steps at 250fs
if(n<17)then
  for k=1 to 10 step 2


        rem Close
        auxout(1,0)
        rem Take Data without Pump
        run()
        delay(d)

        rem Separate Data
        copy(#0(1<<1024,1),#1)
        copy(#0(1<<1024,2),#2)

                rem Save Data in *.txt
                for i=1 to 1024
                        a=write(file$, (i,#1_sig[i],#2_sig[i]),0,dline,k)
                        if a<0 then
                                print("Error on write")
                        endif
                next


                rem Open
                auxout(1,1)
                rem Take Data with Pump
                run()
                delay(d)
                rem Close
                auxout(1,0)

                rem Separate Data
                copy(#0(1<<1024,1),#1)
                copy(#0(1<<1024,2),#2)

                rem Save Data in *.txt
                for i=1 to 1024
                        a=write(file$, (i,#1_sig[i],#2_sig[i]),1,dline,k+1)
                        if a<0 then
                                print("Error on write")
                        endif
                next
    next

    comwrite(1,"IX F150 D-375*\r")
    delay(3000)
    dline = dline + .250

  endif

rem Data from 2.5ps to 6ps at 500fs steps
if(n<25) && (n>16) then
  for k=1 to 10 step 2


        rem Close
        auxout(1,0)
        rem Take Data without Pump
        run()
        delay(d)

        rem Separate Data
```

```
        copy(#0(1<<1024,1),#1)
        copy(#0(1<<1024,2),#2)

                rem Save Data in *.txt
                for i=1 to 1024
                        a=write(file$, (i,#1_sig[i],#2_sig[i]),0,dline,k)
                        if a<0 then
                                print("Error on write")
                        endif
                next


                rem Open
                auxout(1,1)
                rem Take Data with Pump
                run()
                delay(d)
                rem Close
                auxout(1,0)

                rem Separate Data
                copy(#0(1<<1024,1),#1)
                copy(#0(1<<1024,2),#2)

                rem Save Data in *.txt
                for i=1 to 1024
                        a=write(file$, (i,#1_sig[i],#2_sig[i]),1,dline,k+1)
                        if a<0 then
                                print("Error on write")
                        endif
                next
    next

    comwrite(1,"IX F250 D-750"\r")
    delay(3000)
    dline = dline + .50

  endif

rem Data from 6ps to 12ps at 750fs steps
if(n<30) && (n>24) then
  for k=1 to 10 step 2


        rem Close
        auxout(1,0)
        rem Take Data without Pump
        run()
        delay(d)

        rem Separate Data
        copy(#0(1<<1024,1),#1)
        copy(#0(1<<1024,2),#2)

                rem Save Data in *.txt
                for i=1 to 1024
                        a=write(file$, (i,#1_sig[i],#2_sig[i]),0,dline,k)
                        if a<0 then
                                print("Error on write")
                        endif
                next


                rem Open
                auxout(1,1)
                rem Take Data with Pump
                run()
                delay(d)
                rem Close
                auxout(1,0)

                rem Separate Data
                copy(#0(1<<1024,1),#1)
                copy(#0(1<<1024,2),#2)

                rem Save Data in *.txt
                for i=1 to 1024
                        a=write(file$, (i,#1_sig[i],#2_sig[i]),1,dline,k+1)
                        if a<0 then
                                print("Error on write")
                        endif
                next
    next

    comwrite(1,"IX F400 D-1125"\r")
    delay(3000)
    dline = dline + .750

  endif

rem Data from 12ps to max at 2000fs steps
if(n>29) then
  for k=1 to 10 step 2
```

```
        rem Close
        auxout(1,0)
        rem Take Data without Pump
        run()
        delay(d)

        rem Separate Data
        copy(#0(1<<1024,1),#1)
        copy(#0(1<<1024,2),#2)

                rem Save Data in *.txt
                for i=1 to 1024
                        a=write(file$, (i,#1_sig[i],#2_sig[i]),0,dline,k)
                        if a<0 then
                                print("Error on write")
                        endif
                next


                rem Open
                auxout(1,1)
                rem Take Data with Pump
                run()
                delay(d)
                rem Close
                auxout(1,0)

                rem Separate Data
                copy(#0(1<<1024,1),#1)
                copy(#0(1<<1024,2),#2)

                rem Save Data in *.txt
                for i=1 to 1024
                        a=write(file$, (i,#1_sig[i],#2_sig[i]),1,dline,k+1)
                        if a<0 then
                                print("Error on write")
                        endif
                next
    next

    comwrite(1,"IX F1000 D-3000"\r")
    delay(3000)
    dline = dline + 2

  endif

n=n+1
wend
```

Figure 8.1: Data acquisition script for thermoreflectivity experiments - This script was written in the Andor Basic environment and can be executed using the Andor software. It controls both an optical shutter and the optical delay stage by writing either to the auxiliary output or to the COM1 port. In short, this script will collect both the signal and the reference data using two different user-define tracks on the CCD at various pump-probe delays with and without the pump present, and then save each spectra in a single file.

```
rem sets delay in milliseconds
input("Enter Acq Time in milliseconds",d)

input("Enter File Name (*.txt)", file$)

rem Background Acq
SetAcquisitionType(1)
run()
rem Set Data Acq
SetAcquisitionType(0)

baud(1,9600)

rem Set Delay Communication
comwrite(1,">>01\r")
comwrite(1,"LD*\r")
comwrite(1,"IHX*\r")
rem delay(10000)
comwrite(1,"IN*\r")

rem Closes Shutter
auxout(1,0)

rem variable to keep track of pump-probe delay
dline = -4.000
rem counter for number of delays
n=0
while(n<65)

rem Data from -3.5ps to -1.5ps; 4 steps at 500fs
if(n<5)then
  for k=1 to 2 step 2


        rem Close
        auxout(1,0)
        rem Take Data without Pump
        run()
        delay(d)

        rem Separate Data
        copy(#0(1<<1024,1),#1)
        rem copy(#0(1<<1024,2),#2)

                rem Save Data in *.txt
                for i=1 to 1024
                rem     a=write(file$, (i,#1_sig[i],#2_sig[i]),0,dline,k))
                        a=write(file$, (i,#1_sig[i],k,dline))
                        if a<0 then
                                print("Error on write")
                        endif
                next


                rem Open
                auxout(1,1)
                rem Take Data with Pump
                run()
                delay(d)
                rem Close
                auxout(1,0)

                rem Separate Data
                copy(#0(1<<1024,1),#1)
                rem copy(#0(1<<1024,2),#2)

                rem Save Data in *.txt
                for i=1 to 1024
                        rem a=write(file$, (i,#1_sig[i],#2_sig[i]),1,dline,k+1))
                        a=write(file$, (i,#1_sig[i],k+1,dline))
                        if a<0 then
                                print("Error on write")
                        endif
                next
    next

    comwrite(1,"IX F250 D-750*\r")
    delay(3000)
```

```
    dline = dline + .500

  endif

rem Data from -1.3ps to 2.5ps at 200fs steps
if(n<25) && (n>4) then
  for k=1 to 2 step 2

        rem Close
        auxout(1,0)
        rem Take Data without Pump
        run()
        delay(d)

        rem Separate Data
        copy(#0(1<<1024,1),#1)
        rem copy(#0(1<<1024,2),#2)

                rem Save Data in *.txt
                for i=1 to 1024
                rem     a=write(file$, (i,#1_sig[i],#2_sig[i]),0,dline,k)
                        a=write(file$, (i,#1_sig[i],k,dline))
                        if a<0 then
                                print("Error on write")
                        endif
                next


                rem Open
                auxout(1,1)
                rem Take Data with Pump
                run()
                delay(d)
                rem Close
                auxout(1,0)

                rem Separate Data
                copy(#0(1<<1024,1),#1)
                rem copy(#0(1<<1024,2),#2)

                rem Save Data in *.txt
                for i=1 to 1024
                        rem a=write(file$, (i,#1_sig[i],#2_sig[i]),1,dline,k+1)
                        a=write(file$, (i,#1_sig[i],k+1,dline))
                        if a<0 then
                                print("Error on write")
                        endif
                next
    next

    comwrite(1,"IX F100 D-300*\r")
    delay(3000)
    dline = dline + .200

  endif

rem Data from 3ps to 5.5ps at 500fs steps
if(n<31) && (n>24) then
   for k=1 to 2 step 2


                rem Close
        auxout(1,0)
        rem Take Data without Pump
        run()
        delay(d)

        rem Separate Data
        copy(#0(1<<1024,1),#1)
        rem copy(#0(1<<1024,2),#2)

                rem Save Data in *.txt
                for i=1 to 1024
                rem     a=write(file$, (i,#1_sig[i],#2_sig[i]),0,dline,k)
                        a=write(file$, (i,#1_sig[i],k,dline))
                        if a<0 then
                                print("Error on write")
                        endif
                next
```

```
                rem Open
                auxout(1,1)
                rem Take Data with Pump
                run()
                delay(d)
                rem Close
                auxout(1,0)

                rem Separate Data
                copy(#0(1<<1024,1),#1)
                rem copy(#0(1<<1024,2),#2)

                rem Save Data in *.txt
                for i=1 to 1024
                        rem a=write(file$, (i,#1_sig[i],#2_sig[i]),1,dline,k+1)
                        a=write(file$, (i,#1_sig[i],k+1,dline))
                        if a<0 then
                                print("Error on write")
                        endif
                next
    next


    comwrite(1,"IX F250 D-750*\r")
    delay(3000)
    dline = dline + .500

  endif


  rem Data from 6.5ps to 10.5ps at 1000fs steps
if(n<36) && (n>30) then
   for k=1 to 2 step 2


                rem Close
        auxout(1,0)
        rem Take Data without Pump
        run()
        delay(d)

        rem Separate Data
        copy(#0(1<<1024,1),#1)
        rem copy(#0(1<<1024,2),#2)

                rem Save Data in *.txt
                for i=1 to 1024
                rem     a=write(file$, (i,#1_sig[i],#2_sig[i]),0,dline,k)
                        a=write(file$, (i,#1_sig[i],k,dline))
                        if a<0 then
                                print("Error on write")
                        endif
                next


                rem Open
                auxout(1,1)
                rem Take Data with Pump
                run()
                delay(d)
                rem Close
                auxout(1,0)

                rem Separate Data
                copy(#0(1<<1024,1),#1)
                rem copy(#0(1<<1024,2),#2)

                rem Save Data in *.txt
                for i=1 to 1024
                        rem a=write(file$, (i,#1_sig[i],#2_sig[i]),1,dline,k+1)
                        a=write(file$, (i,#1_sig[i],k+1,dline))
                        if a<0 then
                                print("Error on write")
                        endif
                next
    next
```

```
    comwrite(1,"IX F500 D-1500*\r")
    delay(3000)
    dline = dline + 1.00

  endif


rem Data from 12.5ps to 20.5ps at 2000fs steps
if(n<41) && (n>35) then
   for k=1 to 2 step 2


               rem Close
        auxout(1,0)
        rem Take Data without Pump
        run()
        delay(d)

        rem Separate Data
        copy(#0(1<<1024,1),#1)
        rem copy(#0(1<<1024,2),#2)

                rem Save Data in *.txt
                for i=1 to 1024
                rem     a=write(file$, (i,#1_sig[i],#2_sig[i]),0,dline,k)
                        a=write(file$, (i,#1_sig[i],k,dline))
                        if a<0 then
                                print("Error on write")
                        endif
                next


                rem Open
                auxout(1,1)
                rem Take Data with Pump
                run()
                delay(d)
                rem Close
                auxout(1,0)

                rem Separate Data
                copy(#0(1<<1024,1),#1)
                rem copy(#0(1<<1024,2),#2)

                rem Save Data in *.txt
                for i=1 to 1024
                        rem a=write(file$, (i,#1_sig[i],#2_sig[i]),1,dline,k+1)
                        a=write(file$, (i,#1_sig[i],k+1,dline))
                        if a<0 then
                                print("Error on write")
                        endif
                next
    next


    comwrite(1,"IX F1000 D-3000*\r")
    delay(3000)
    dline = dline + 2.000

  endif


rem Data from 24.5ps to 40.5ps at 4000fs steps
if(n<46) && (n>40) then
   for k=1 to 2 step 2


               rem Close
        auxout(1,0)
        rem Take Data without Pump
        run()
        delay(d)

        rem Separate Data
        copy(#0(1<<1024,1),#1)
        rem copy(#0(1<<1024,2),#2)

                rem Save Data in *.txt
```

```
                for i=1 to 1024
                rem     a=write(file$, (i,#1_sig[i],#2_sig[i]),0,dline,k)
                        a=write(file$, (i,#1_sig[i],k,dline))
                        if a<0 then
                                print("Error on write")
                        endif
                next


                rem Open
                auxout(1,1)
                rem Take Data with Pump
                run()
                delay(d)
                rem Close
                auxout(1,0)

                rem Separate Data
                copy(#0(1<<1024,1),#1)
                rem copy(#0(1<<1024,2),#2)

                rem Save Data in *.txt
                for i=1 to 1024
                        rem a=write(file$, (i,#1_sig[i],#2_sig[i]),1,dline,k+1)
                        a=write(file$, (i,#1_sig[i],k+1,dline))
                        if a<0 then
                                print("Error on write")
                        endif
                next
    next


    comwrite(1,"IX F1000 D-6000*\r")
    delay(6000)
    dline = dline + 4.000

  endif

rem Data from 48.5ps to 8.5ps at 8000fs steps
if(n>45) then
  for k=1 to 2 step 2


                rem Close
        auxout(1,0)
        rem Take Data without Pump
        run()
        delay(d)

        rem Separate Data
        copy(#0(1<<1024,1),#1)
        rem copy(#0(1<<1024,2),#2)

                rem Save Data in *.txt
                for i=1 to 1024
                rem     a=write(file$, (i,#1_sig[i],#2_sig[i]),0,dline,k)
                        a=write(file$, (i,#1_sig[i],k,dline))
                        if a<0 then
                                print("Error on write")
                        endif
                next


                rem Open
                auxout(1,1)
                rem Take Data with Pump
                run()
                delay(d)
                rem Close
                auxout(1,0)

                rem Separate Data
                copy(#0(1<<1024,1),#1)
                rem copy(#0(1<<1024,2),#2)

                rem Save Data in *.txt
                for i=1 to 1024
                        rem a=write(file$, (i,#1_sig[i],#2_sig[i]),1,dline,k+1)
                        a=write(file$, (i,#1_sig[i],k+1,dline))
```

```
                    if a<0 then
                            print("Error on write")
                    endif
                next
    next


    comwrite(1,"IX F2000 D-15000*\r")
    delay(7500)
    dline = dline + 10.0

  endif

n=n+1
wend
```

Figure 8.2: Data acquisition script for molecular conductance experiments – This script was written in the Andor Basic environment and can be executed using the Andor software. It controls both an optical shutter and the optical delay stage by writing either to the auxiliary output or to the COM1 port. In short, this script will collect both the signal and the reference data using two different user-define tracks on the CCD at various pump-probe delays with and without the pump present, and then save each spectra in a single file. Other versions of this code exist. Some have been modified to calculate peak area or peak height, along with peak position on the fly and save that data to an output file.

```
SetAcquisitionType(1)
rem run()

SetAcquisitionType(0)
baud(1,9600)

comwrite(1,">>01\r")

comwrite(1,"LD*\r")
comwrite(1,"IHX*\r")
rem delay(15000)
rem comwrite(1,"IX F15000 D-60000*\r")
rem comwrite(1,"IX F4000 D-303000*\r")
```

Figure 8.3: Script for delay line -This code will allowed independent control of the optical delay line for the pump pulse. As written, this code will move the delay line to the home position. Other delays are also possible by removing the remarks (rem) from the line of code that one may want. Within the "comwrite" command, the number after the "D" is the delay in 1500 steps/ps. The number after the "F" denotes the feed rate of the stepper motor. No other variables should be changed.

```
COMEXC0 ; continuous command processing off
COMEXS0 ; continue execution on stop off
SINGO00 ; kill sine wave generators
SINANG0.0,0.0 ; reset sine generators phase
FOLEN00 ; disable following
FOLMAS0,0 ; remove master sources
FOLRN1,1 ; follower ratio numerator
FOLRD1,1 ; follower ratio denominator
MA11 ; absolute mode enable
MC00 ; preset move mode
DRIVE11 ; enable drives
OUTLVL11 ;set output level logic
OUT00 ; reset outputs
INLVL00 ; set input level logic

; Scaling setup (millimeters on both axes)
SCLD800,2000 ; distance scaling
SCLA800,2000 ; acceleration scaling
SCLV800,2000 ; velocity scaling
SCALE1 ; enable scaling

; General motion
V100,100 ; velocity
A20,20 ; acceleration

; Homing
HOMBAC11 ; enable home backup
HOMEDG00 ; setting active home edge
HOMVF1.00,1.000 ; final home approach velocity
HOMV30,30
HOMA30,30

; Servo setup
SGP98.0,120.0
SGI0.0,0.0
SGV3.5,3.0
SGVF0.0,0.0
SGAF0.0,0.0
SOFFS+0.000,+0.000
SGILIM200,200
```

Figure 8.4: Lissajous figure parameters -This code will initialize the servo motor controls with the correct parameters and remove any unnecessary parameters stored in the controller member. If this script is not run before the Lissajous motion script, the controller may not behave correctly.

```
V10.00,10.000 ; taxi velocities
D-37.50,-5.00
MC00 ; preset mode
GO11 ; assume initial position
V100.00,100.000
; Current working frequencies: 5400,5001
FVMFRQ5400,5001; count frequency (3600=1 cycle/sec)
FOLMAS16,26
FOLRN35.00,35.000
FOLRD1.000,1.000
SINAMP2000,2000
SINANG180.0,180.0
FOLEN11
MC11 ; mode continuous
@FVMACC200.0
COMEXC1
COMEXS1
GO11
; start sine waves
SINGO11
; ramp up time
T35.000
TFS
END
```

Figure 8.5: Lissajous motion script -This script runs both servo motors that drive the sample stage in constant motion following a predetermined Lissajous figure.

```
#include <string.h>
#include <stdio.h>
#include <stdlib.h>
#include <math.h>
main()
{
    int nd=90; // number of delays
    int ns=10; // number of spectra at each delay
    int Data[nd][2*ns+1][1024]; // [delay][spectra][pixel]

    int i,j,k;


    float ***DataF;
    float ***dRR;
    float ***AdRR;



    DataF=(float***)malloc(nd*sizeof(float**));
        for(i=0;i<nd;i++){
            DataF[i]=(float**)malloc((2*ns+1)*sizeof(float*));
                for(j=0;j<2*ns+1;j++){
                    DataF[i][j]=(float*)malloc(1024*sizeof(float));
                        for(k=0;k<1024;k++){
                            DataF[i][j][k]=0;
                        }
                }
        }


    float r=1.0000;



    dRR=(float***)malloc(nd*sizeof(float**));
        for(i=0;i<nd;i++){
            dRR[i]=(float**)malloc((1+ns/2)*sizeof(float*));
                for(j=0;j<1+ns/2;j++){
                    dRR[i][j]=(float*)malloc(1024*sizeof(float));
                        for(k=0;k<1024;k++){
                            dRR[i][j][k]=0;
                        }
                }
        }



        AdRR=(float***)malloc(nd*sizeof(float**));
        for(i=0;i<nd;i++){
            AdRR[i]=(float**)malloc(2*sizeof(float*));
                for(j=0;j<2;j++){
                    AdRR[i][j]=(float*)malloc(1024*sizeof(float));
                        for(k=0;k<1024;k++){
                            AdRR[i][j][k]=0;
                        }
                }
        }



    int S;
    float D;
    int J1;
    int J2;



    FILE *fp;
    fp = fopen("./20100418_WL/8ACr_60mW_double.txt", "r");

// make matrix for each delay, 10 pairs of spectra per delay
// d1 r1 d2 r2 d3 r3 ... where d1 is data1 is un-pumped, d2 is pumped

for(i=0;i<nd;i++){                                          //loop for delays
    for(j=0;j<ns;j++){                                      //loop over each spectra

        if(j%ns==0){
            for(k=0;k<1024;k++){
                fscanf(fp, "%i %i %i %i %f %i", &Data[i][0][k], &Data[i][1][k], &Data[i][2][k], &S, &D, &J1);
            }
        }
        else if(j%ns==1){
            for(k=0;k<1024;k++){
                fscanf(fp, "%i %i %i %i %f %i", &J2, &Data[i][3][k], &Data[i][4][k], &S, &D, &J1);
            }
        }
        else if(j%ns==2){
            for(k=0;k<1024;k++){
                fscanf(fp, "%i %i %i %i %f %i", &J2, &Data[i][5][k], &Data[i][6][k], &S, &D, &J1);
            }
        }
        else if(j%ns==3){
            for(k=0;k<1024;k++){
                fscanf(fp, "%i %i %i %i %f %i", &J2, &Data[i][7][k], &Data[i][8][k], &S, &D, &J1);
            }
        }
```

```
        else if(j%ns==4){
            for(k=0;k<1024;k++){
                fscanf(fp, "%i %i %i %i %f %i", &J2, &Data[i][9][k], &Data[i][10][k], &S, &D, &J1);
            }
        }
        else if(j%ns==5){
            for(k=0;k<1024;k++){
                fscanf(fp, "%i %i %i %i %f %i", &J2, &Data[i][11][k], &Data[i][12][k], &S, &D, &J1);
            }
        }
        else if(j%ns==6){
            for(k=0;k<1024;k++){
                fscanf(fp, "%i %i %i %i %f %i", &J2, &Data[i][13][k], &Data[i][14][k], &S, &D, &J1);
            }
        }
        else if(j%ns==7){
            for(k=0;k<1024;k++){
                fscanf(fp, "%i %i %i %i %f %i", &J2, &Data[i][15][k], &Data[i][16][k], &S, &D, &J1);
            }
        }
        else if(j%ns==8){
            for(k=0;k<1024;k++){
                fscanf(fp, "%i %i %i %i %f %i", &J2, &Data[i][17][k], &Data[i][18][k], &S, &D, &J1);
            }
        }

        else if(j%ns==9){
            for(k=0;k<1024;k++){
                fscanf(fp, "%i %i %i %i %f %i", &J2, &Data[i][19][k], &Data[i][20][k], &S, &D, &J1);
            //  printf("%f\n",D);
            }
        }

    }
}

for(i=0;i<nd;i++){                                      //loop for delays
    for(k=0;k<2*ns+1;k++){
        for(j=0;j<1024;j++){
        DataF[i][k][j]=r*Data[i][k][j];
        }
    }
}



fclose(fp);
for(i=0;i<nd;i++){                                      //loop for delays
    for(j=0;j<1024;j++){
        dRR[i][0][j] = DataF[i][0][j];                  //pixel number in [i][0][j] and data in [i][1][j]
        dRR[i][1][j] = -(DataF[i][1][j]/DataF[i][2][j]-DataF[i][3][j]/DataF[i][4][j])/(DataF[i][1][j]/DataF[i][2][j]);
        dRR[i][2][j] = -(DataF[i][5][j]/DataF[i][6][j]-DataF[i][7][j]/DataF[i][8][j])/(DataF[i][5][j]/DataF[i][6][j]);
        dRR[i][3][j] = -(DataF[i][9][j]/DataF[i][10][j]-DataF[i][11][j]/DataF[i][12][j])/(DataF[i][9][j]/DataF[i][10][j]);
        dRR[i][4][j] = -(DataF[i][13][j]/DataF[i][14][j]-DataF[i][15][j]/DataF[i][16][j])/(DataF[i][13][j]/DataF[i][14][j]);
        dRR[i][5][j] = -(DataF[i][17][j]/DataF[i][18][j]-DataF[i][19][j]/DataF[i][20][j])/(DataF[i][17][j]/DataF[i][18][j]);
    }
}



for(i=0;i<nd;i++){                                      //loop for delays
    for(j=0;j<1024;j++){
        AdRR[i][0][j] = dRR[i][0][j];                   //pixel number in [i][0][j] and data in [i][1][j]
        AdRR[i][1][j] = 0.20000*(dRR[i][1][j] + dRR[i][2][j] + dRR[i][3][j] + dRR[i][4][j] + dRR[i][5][j]);
    }
}



fp = fopen("./20100418_Processed/Processed_8ACr_60mW_double.txt", "w");

//  PRINTS THE DATA
/*
    fprintf(fp, "Delay\tPixel\tCLOSED\tOPEN\tCLOSED\tOPEN\tCLOSED\tOPEN\tCLOSED\tOPEN\tCLOSED\tOPEN\tCLOSED\tOPEN\tCLOSED\tOPEN\tCLOSED\tOPEN\tCLOSED\tOPEN");

for(k=0;k<nd;k++){                                      //loop over delay
    for(i=0;i<1024;i++){
        fprintf(fp,"\n%i  %i  ",k+1,i+1);
        fprintf(fp, "%f   %f   %f   %f   %f   %f   %f   %f   %f",DataF[k][1][i],DataF[k][2][i],DataF[k][3][i],DataF[k][4][i],DataF[k][5][i],DataF[k][6][i],DataF[k][7][i],DataF[k]
[8][i],
        DataF[k][9][i]);

    //  fprintf(fp, "%f   %f   %f   %f   %f   %f   %f   %f   %f   %f   %f   %f   %f   %f   %f   %f %f   %f   %f   %f",
    //  DataF[k][1][i],DataF[k][2][i],DataF[k][3][i],DataF[k][4][i],DataF[k][5][i],DataF[k][6][i],DataF[k][7][i],DataF[k][8][i],
    //  DataF[k][9][i],DataF[k][10][i],DataF[k][11][i],DataF[k][12][i],DataF[k][13][i],DataF[k][14][i],DataF[k][15][i],
    //  DataF[k][16][i],DataF[k][17][i],DataF[k][18][i],DataF[k][19][i],DataF[k][20][i]);
    }
}
*/


 //PRINTS THE reduced DATA
/*
    fprintf(fp, "Delay\tPixel\tdr1\tdr2\tdr3\tdr4\tdr5");

for(k=0;k<10;k++){                                      //loop over delay
    for(i=0;i<1024;i++){
```

```
        fprintf(fp,"\n%i   %i   ",k+1,i+1);
        fprintf(fp, "%f   %f   %f   %f   %f",
        dRR[k][1][i],dRR[k][2][i],dRR[k][3][i],dRR[k][4][i],dRR[k][5][i]);
    }
}

*/

//PRINTS THE FINAL DATA
    k=0;
    for(i=0;i<1024;i++){
        fprintf(fp,"%i\t",i);
        for(k=0;k<nd;k++){
            fprintf(fp,"\t%7.4f",AdRR[k][1][i]);
    }
        fprintf(fp,"\n");
}


fclose(fp);



} //main
```

Figure 8.6: Thermoreflectance data analysis - This C code is used to analyze thermoreflectance data using the white-light continuum source. This code opens the raw data file and computes the average normalized changes in reflectance for all wavelengths and delays. The resulting output is then saved to a new file. Both the input and output files need to be changed manually and then the code needs to be recompiled.

```
#pragma rtGlobals=1        // Use modern global access method.

Function SIM(Td, FWHMir, FWHMvis, VISDecay, FWHMpump, T2,T0,phase)

variable Td
variable  FWHMir
variable  FWHMvis
variable VISDecay
variable  FWHMpump
variable T2
variable T0
variable phase
//  FOR T=2ps DECAY OF NB, Tnb     = 300 fs (0.30 ps)
//  value found by Maximizing NR w/r/t Tnb delay
// variable Tnb = -.300, this variable is now T0



variable res=0.001 // Sets the step RESolution in ps i.e. 0.001 = 1 fs res

Make /o/n = (25/res) ps =0 // 25 ps -5 to 15
Make /o/n = (25/res) IR =0
Make /o/n = (25/res) IRPolar =0
Make /o/n = (25/res) SFGPolar =0
Make /o/n = (25/res) IRPolarConv =0
Make /o/n = (25/res) FID =0
Make /o/n = (25/res) FID2 =0
Make /o/n = (25/res) VIS =0
Make /o/n = (25/res) IRp01 =0
Make /o/n = (25/res) PUMP =0
Make /o/n = (25/res) Orient =0
Make /o/n = (25/res) IRdecay =0
Make /o/n = (25/res) GreenFunc =0
Make /o/n = (25/res) ConvGF = 0
Make /o/n = (25/res) StepFunc = 0
Make /o/n = (25/res) StepFunc2 = 0
Make /o/n = (25/res) Spectrum
Make /o/n = (25/res) Var1 =0
Make /o/n = (25/res) Var2 =0
Make /o/n = (25/res) Var3 =0

// Defines picosecond times
ps = x*res-15  // counts backward to move VIS pulse and keep IR at ps = 0

//Defines the IR laser Pulse with FWHMir as input
variable  sigmaIR  =  FWHMir/sqrt(8*ln(2))
IR  =  1/(sigmaIR*sqrt(2*pi))*exp(-(ps)^2/(2*sigmaIR^2))
```

```
//Defines the VIS laser Pulse with FWHMvis as input
    variable sigmaVIS = FWHMvis/sqrt(8*ln(2))
//OPTION 1. NBVIS through etalon for FREQUENCY RESOLUTION.
    VIS = (1+erf((ps-Td+.3)/(sigmaVis*sqrt(2))))/2*exp(-(ps-Td+.3)/VISDecay)

//OPTION 2. Femtosecond probe pulse for TIME RESOLUTION.
    //VIS  =  1/(sigmaVIS*sqrt(2*pi))*exp(-(ps-Td)^2/(2*sigmaVIS^2))



Make/o/n = (25/.02) Delay
Make/o/n = (25/.02) Signal
Make /o/n = (25/.02) CC
Make /o/n = (25/.02) TD_Signal
Make /o/n=(25/.2,150)/D SpectraMatrix //Contains 50 spectra spaced by 0.2 ps
variable T
variable i=0
variable j=0
variable k=0

variable sigmaPUMP = FWHMpump/sqrt(8*ln(2))

// scalef changes the ratio of resonant to non-resonant
variable scalef = 0 // 0.69 is default with R and NR equal for T2 =1ps




// For loop that moves the PUMP pulse
for(T=10; T>-15; T -= 0.02)
    PUMP  =  1/(sigmaPUMP*sqrt(2*pi))*exp(-(ps-T)^2/(2*sigmaPUMP^2))

    //  OPTION 1: STEPFUNCTION RESPONSE
    //  Integrate/METH=1  PUMP/X=ps/D=StepConvPUMP

    //  OPTION 2: EXPONENTIAL DECAY RESPONSE
    for(i=0; i<25000; i+=1)
        if(i/1000-15 > T+T0)
        StepFunc[i] = 1
        endif
    endfor

     GreenFunc = StepFunc*(1-exp(-(ps-T-T0)/16))
     ConvGF = GreenFunc
```

```
// Calculates an effective IR polarization under the influence of the PUMP

    //  OPTION 1: STEPFUNCTION CALCULATION
    //   Orient  =  (1-.5*StepConvPUMP)

    //  OPTION 2: EXPONENTIAL DECAY CALCULATION
        Orient  =  (1-.5*ConvGF)


    //  SAME FOR BOTH OPTIONS
        Var3  =  IR*Orient
        Integrate/METH=1  Var3/X=ps/D=IRPolar  // p01  =  int(V(t)[p00-p11]
        IRPolar=IRPolar*exp(-ps/T2)              // ad hoc decay, needs a convolution


    SFGPolar  =  IRPolar*Orient*Orient*VIS*(sigmaVIS*sqrt(2*pi)) //extra factor is for VIS peak to
    // The FID contains two terms: Resonant and NR parts
    FID  =  VIS*Orient^2*(IRPolar*sin(90*ps+phase/180*3.14159)  +  IR*sin(90*ps)*scalef)
    FFT/OUT=4/DEST=Spectrum FID



    // Calculates Signal at the Resonance
    Signal[j]  =  Spectrum[358]

    Delay[j]  =  -T

    // Calculates the IR-Pump Cross Correlation
    Var1  =  IR*PUMP
    Integrate/METH=1  Var1/X=ps/D=Var2
    CC[j]  =  Var2[24999]
    j+=1

    // Saves the spectrum every 200 fs.
//  if(mod(T,.2)<1E-5)
//      for(j=0;j<150;j+=1)
//      SpectraMatrix[k][j]=  Spectrum[150+j]
//      endfor
//      k+=1
//  endif
endfor


// Calculates the VRF by Normalizing the Signal at the Resonance
variable  SigMin=Signal[899]
variable  SigMax=Signal[1]
Make/o/n = (25/.02) NormResponse
NormResponse  =  (SigMax-Signal)/(SigMax-SigMin)
```

```
//Display FID, IRpolar, IR vs ps
//Display CC, NormResponse vs Delay

//Display IR,IRpolar,VIS,NB,DeltaConvVIS, ChiR, vs ps
//ModifyGraph  rgb(IR)=(0,0,65535)
//ModifyGraph  rgb(ChiR)=(0,0,65535)
//ModifyGraph  rgb(NB)=(10,10,10)
//SetAxis bottom -1,1
//SetAxis left 0,5

//Display IRpolar, ChiR, NR, junk1 vs ps

end



//Calculates NRsingal vs Tnb

// Make/o/n = (30/.2) DelayNR
 //Make/o/n = (30/.2) NRsignal
//

// for(Tnb=10; Tnb>=-5; Tnb-=.1)
//  NB  =  (1+erf((ps-Tnb)/0.1))*exp(-(ps-Tnb)/DECAYnb)
//  NR = NB*IR
//  Integrate/METH=1 NR/X=ps/D=IntegratedNR
//  NRsignal[i] = IntegratedNR[5499]
//  DelayNR[i] = -Tnb
//  i+=1
 //endfor
// Display NRsignal vs DelayNR
// Display NB, IntegratedNR,IR vs ps
// End of NRsignal vs Tnb




//for(i=0; i<25000; i+=1)
//      if(i/1000-15 > 0)
//      StepFunc2[i] = 1
//      endif
//  endfor
//  IRdecay = StepFunc2*exp(-ps/T2)
//  Var3 = IRdecay
//  Convolve/A  IRPolar, Var3
//  for(i=0; i<25000; i+=1)
```

```
2/23/11                    SIMREAL.ipf                    5

//      if(i<22499)
//      Var3[i]=Var3[i+2500]*0.0045773 // multiplication re-normalizes this wave
//      else
//      Var3[i]=IRdecay[i] // finishes the convolved wave with the real wave at long times, where the cc
//      endif
//  endfor


    // Calculates the time-dependent Intensity
     //FID2 = FID*FID
     //Integrate/METH=1 FID2/X=ps/D=INT_FID
     //TD_Signal[i] = INT_FID[14999]
```

Figure 8.7: 2D-SFG script - This was written in Igor and was used to simulated the effects of varying the time delays between the pump and IR probe pulses and between the IR probe and the VIS probe pulses.